On the drying of polymer- plate-like particle-composites
Numerical study and experimental validation

Zur Erlangung des akademischen Grades eines

DOKTORS DER INGENIEURWISSENSCHAFTEN

von der KIT-Fakultät für Chemieingenieurwesen und Verfahrenstechnik

des

Karlsruher Instituts für Technologie (KIT)

genehmigte

DISSERTATION

von

M. Eng. Víctor Alfonso Gracia Medrano Bravo

Tag der mündlichen Prüfung: 24.03.2023

Erstgutachter: Prof. Dr.-Ing. Dr. h. c. Wilhelm Schabel

Zweitgutachter: Prof. Dr. Alexander Routh
(University of Cambridge)

Kurzfassung

Polymer-Partikel-Komposite sind zunehmend in den Fokus der angewandten Materialforschung gerückt. Durch die Einbettung von kolloidalen Nanopartikeln in eine Polymermatrix werden solchen Polymer-Partikel Kompositen neue Eigenschaften verliehen. Hierzu zählen u. a. Beeinflussung der mechanischen Eigenschaften, der elektrischen Leitfähigkeit, der thermischen Eigenschaften, der optischen Transparenz oder auch der Biokompatibilität. Die Funktionalität von Polymer-Partikel-Kompositen hängt in erster Linie von der Materialauswahl und deren Zusammensetzung, aber auch maßgeblich sowohl von der Verteilung als auch der räumlichen Ausrichtung dieser ab. Die meisten Kompositbeschichtungen werden durch Beschichten einer Dispersion mit anschließender Trocknung hergestellt. Die Komponentenverteilung in der Schicht selbst, die dabei entsteht; hängt vor allem von der Partikelgröße, -material, -geometrie und von der Trocknungsrate ab. Letztere wird von den Wärme- und Stofftransportprozessen bei den gegebenen Randbedingungen bestimmt. Die Partikelausrichtung wird auch durch unterschiedliche Scherung während des Beschichtungsprozesses z.B. einer Couette-Strömung in einem Beschichtungsspalt beeinflusst.

Der Einfluss der Trocknungsrandbedingungen auf die Komponentenverteilung von sphärischen Partikel-Polymer-Kompositen wurde in vorherigen Arbeiten (Baesch at al., Cardinal et al. and Routh at al.) untersucht. Für sphärische, monomodale Partikel in einer Polymerlösung wurden die Mechanismen der Stoffübertragung von kolloidalen und nicht-kolloidalen Komponenten identifiziert. Auch zeigen Ergebnisse, dass die Partikelgeometrie einen größeren Einfluss auf die Komponentenverteilung hat. Man findet erste Ergebnisse zum Einfluss der Partikelverteilung bei sehr flachen, plättchenförmigen Partikelsystemen. In den bisherigen Arbeiten war das Ziel, den Einfluss der Abflachung der Geometrie auf die Partikelverteilung während der Trocknung zu untersuchen. Es konnte evaluiert werden, wie die Simulationsroutine und die Modellierung für sphärische Partikel auch bei plättchenförmigen Partikeln weiterverwendet werden können. Diese neuen Geometrien wurden angepasst und durch die Untersuchung alternativer Stoffsysteme experimentell validiert. Zu diesem Zweck kann die Partikelverteilung im trockenen Film dreidimensional mittels Mess- und Auswerteroutinen mit Hilfe von in 3-D aufgenommen

Ramanspektren bestimmt werden. Die Abhängigkeit zwischen Partikelform und Partikeldynamik wird mittels Lichtinterferometrie in einer Zentrifuge bestimmt. Dabei kann die Trocknungsrate, die Partikelgröße und die Anfangskonzentration variiert werden. Bei den 3-D Raman-Aufnahmen in den trockenen Filmen wurden sehr unterschiedliche Partikelverteilungen beobachtet: eine Partikelansammlung an der Unterseite, eine homogene Partikelverteilung über der Filmhöhe oder eine Partikelansammlung an der Oberfläche des Filmes. Beim Vergleich von plättchen zur sphärischen Form zeigte sich, dass die Bewegung von plättchenförmigen Partikeln in einer Polymerlösung durch die Anwesenheit viskoser Widerstände deutlich langsamer erfolgt. Dies konnte bei der Weiterentwicklung der Simulationsmodelle auch berücksichtigt und die entsprechenden Simulationsparameter konnten für plättchenförmige Partikel angepasst werden. Die Ansätze der Simulation beschreiben die Partikeldiffusion, -sedimentation, Polymerdiffusion und Lösemittelverdunstung.

Für den Fall, dass die Plättchen durch ein typisches Beschichtungsverfahren wie z.B. Rakeln und Schlitzguß senkrecht ausgerichtet werden, wurde ein neues Modell entwickelt und verifiziert. Die Einflussparameter dieser Simulation lassen sich analog zu den sphärischen Partikeln zusammenfassen: zum einen als Verhältnis vom Produkt der Schichtdicke und der anfänglichen Trocknungsrate zum Diffusionskoeffizienten der einzelnen Partikel und zum anderen als das Verhältnis von Trocknungsrate zum Sedimentationskoeffizienten der einzelnen Partikel auftragen. Ein dimensionsloses Seitenverhältnis kommt hier zur Péclet-Zahl und Sedimentationszahl hinzu. Durch die systematische Variation dieser entdimensionierten Größen ist es möglich die Komponentenverteilung graphisch in einer dimensionslosen Trocknungskarte darzustellen. Die so erstellten Trocknungskarten ermöglichen es die Partikelverteilung im trockenen Film bei unterschiedlichen Randbedingungen vorherzusagen. Die Ergebnisse dieser Arbeit zeigen eine klare Abweichung von sphärischen Partikeln durch die Trocknungskarten in Abhängigkeit der Partikelform.

Abstract

Polymer-particle composites have been in the spotlight of the applied material research during the last decade. Due to the new properties that the embedding of colloidal nanoparticles in a polymer matrix can give. Some examples are the increase of mechanical properties, electrical conductivity, film transparency and biocompatibility. The functionality of the polymer-particle composites is mostly dependent of the component distribution and, in the case on non-spherical particles, the particles' orientation. This can be influenced by the material properties and boundary conditions during processing. Composites are produced by the coating of a polymer dispersion and subsequently drying of the solvent. The component distribution during drying is a function of the particles' geometry and the dynamics of the film's solidification. The last one can be determined by the mass transfer using conservation equations. The particles' orientation is dependent on the shear stress applied during the coating step, for example a knife coating process generates a Couette flow.

The Influence of the drying conditions on the component distribution of polymer - spherical particle and plate-like particle composites has been studied by Baesch et al. For these polymer-particle systems the mechanisms of the mass transfer were identified. The findings show that the particle geometry has an important influence on the component distribution, and the particle distribution depends heavily on the drying conditions. In the present work, the objective is to see if changes in the component distribution due to the presence of a polymer binder and the change in the geometry can still be described by the models found in the literature, or by adapting the current models for the different types of material systems.

To achieve these goals, the particle concentration in a dry film was investigated using 3-D Raman spectroscopy imaging and the dependence of particle shape and particle mobility was determined using light interferometry while centrifuging. During the study the drying rate, particles aspect ratio, particle size and initial concentration were systematically varied. The Raman imaging showed the three different particle distributions reported in the literature were present. Particle accumulation at the bottom of the film near the substrate, homogeneous particle distribution

along the film's height, and particle accumulation at the top of the film. When comparing particle shapes, the results showed that, the flat geometry of plate-like particles heavily hinders their mobility due to the presence of high viscous drag. This phenomenon was acknowledged with the development of a quasi-binary simulation approach, and the corresponding parameters were changed accordingly. The equations used in the simulation model can describe particle diffusion, particle sedimentation, polymer diffusion and the drying of the solvent.

The rotation of flat particles is not necessary to include in the simulation because after the coating process the plate-like particles tend to orient themselves in a horizontal position. Therefore, the same drying parameters of polymer-spherical particle composites can be used for polymer-plate-like systems. These parameters can be summarized as the ratio between the initial film height times the initial drying rate and the diffusion coefficient of a single particle (particle Péclet number), and as the sedimentation rate divided by drying rate the (sedimentation number). By systematically varying both it is possible to condense the three particle distributions in a graphical manner. The resulting distribution diagrams in dry film are known in the literature as drying regime maps and are a quick tool for predicting the final concentration at different conditions. In this work, it was concluded that the change in geometry causes a deviation from the original diagrams using spherical particles.

Table of Contents

List of abbreviations

OLED	Organic Light-Emitting Diode
COG	Center of Gravity
Cryo-SEM	Cryogenic Scan Electron Microscopy
DOF	Depth of Focus
DPSS	Diode Pumped Solid State
FCC	Face-Centered Cubic
HCP	Hexagonal Closed Packed
HTC	Heat transfer coefficient
IMRS	Inverse Micro Raman Spectroscopy
PDE	Partial Differential Equation
PEDOT	Poly (3,4-Ethylenedioxythiophene)
PSS	Polystyrene Sulfonate
PS	Polystyrene
PVA	Polyvinyl alcohol
SiO_2	Silicon Oxide
v/v	Volume to volume fraction
w/w	Weight to weight mass fraction
w/v	Weight to volume mass fraction

List of Latin symbols

a	Length of particle's vertical semi-axis	m
a_S	Solvent activity	−
A	Parameter for diffusion coefficient see equation (1.1)	−
	Parameter for viscosity see equation (2.9)	$Pa \cdot s$
	Parameter for K_2 expression see equation (3.19)	−
b	lenght of particle's horizonzal semi-axis	m
B	Parameter for diffusion coefficient see equation (1.1)	−
	Parameter for viscosity see equation (2.9)	−
	Bretherton constant	−
	Parameter for K_2 expression see equation (3.19)	−
C	Parameter for diffusion coefficient see equation (1.1)	−
	Parameter for K_2 expression see equation (3.19)	−
$\tilde{c}_i$	Molar to volume concentration of component I	mol/m^3

Symbol	Description	Units
$\tilde{c}_p$	Molar heat capacity at constant pressure	J/mol/K
$\bar{d}$	Orthogonal vector	−
d_C	Particle's (equivalent) diameter	m
d_P	Normalized polymer diffusion coefficient	−
$D_{i,j}$	Diffusion coefficient of component i in the liquid phase j.	m^2/s
$\bar{\bar{E}}$	Normalized evaporation rate	−
$\dot{E}$	Evaporation rate	µm/min
$\bar{\bar{E}}$	Strain tensor	1/s
F	Projection area	m^2
$\bar{f}_i^k$	Force k acting on particle i	N
g	Acceleration of gravity	m/s^2
h	Film thickness or height	m
I_i	Raman intensity of component i	a. u.
j_i	Fickian mass flux	$kg/m^2/s$
$K(\phi_C)$	Hidrance coefficient	−
K_2	Parameter of the sedimentation see equation (3.17)	−
$K_{i,j}$	Raman calibration constant	−
Le	Lewis number	−
M	Torque	$N \cdot m$
$\dot{m}_i$	Specific mass flux of component i	$kg/m^2/s$
$\tilde{M}_i$	Molar mass of component i	g/mol
$\dot{n}_i$	Specific molar flux	$mol/m^2/s$
N_A	Avogadro number	1/mol
N_S	Sedimentation number	−
Pe_i	Péclet number of component i	−
pH	Hydrogen potential	−
Q^n	Cumulative distribution	−
R	Radius of the particle	m
R	Efficiency of the detector system	−
$\bar{\bar{R}}$	Rotation tensor	1/s
$\bar{r}_i$	Position vector of component i	m
r_p	Particle's aspect ratio	−
Re	Reynolds number	−
rH	Relative humidity	−
S_i	Shape constant see equation (3.4) and (3.5)	1/m

List of Greek symbols

τ	Nondimensional time	−
ϕ_i	Volume fraction of component i	−
φ	Polar angle	°
χ_{ij}	Flory-Huggins Interaction parameter between i and j	−
$\overline{\omega}$	Rotation vector	$1/s$
Ω	Angle of the objective	−
$\overline{\Omega}$	Antisimetrical part of the roation tensor R	$1/s$

List of superscripts

*	In thermodynamic equilibrium
$^\infty$	In the atmosphere
^{b}	Binary based property
^{P}	Polymer coordinate

List of subscripts

$_p$	Aspect ratio
$_{crit}$	Critical transport property
$_{eff}$	Effective
$_{gas}$	Gas phase
$_{Gr}$	Graphene
$_0$	Initial or property of a single particle
$_x$	Local transport property
$_{max}$	Maximal packing concentration
$_{mix}$	Mixture
$_{obl}$	Oblate
$_\perp$	Orthogonal
$_\parallel$	Parallel
$_c$	Particle (colloid)
$_P$	Polymer
$_{pr}$	Prolate
$_{dry}$	Property after drying
$_{red}$	Reduced (viscosity)
$_r$	Relative (viscosity)
$_s$	Solvent
$_{sp}$	Specific (viscosity)

Preface

The following work summarizes the scientific research conducted during my PhD from 2017 to 2022 in the Thin Film Technology (TFT) research group at the Karlsruhe Institute of Technology (KIT). It is a collection from the results obtained with the help of the following students: Jakob Gröne, Louis Kontschack, Nikolas Oberle, Manuel Batora, Tanatta van Bonn, Nadine Zimmerer and Meike Dörner.

My doctoral thesis would not have been possible to complete without the instruction and support of my advisors Prof. Dr. Ing. D. h. c. Wilhelm Schabel and Dr.-Ing. Philip Scharfer. I would like to personally thank them for giving me the opportunity to complete my doctoral studies at their research group. Additionally, Margit Morvay who saved my life and helped me with the challenges of German bureaucracy.

In the same manner, I thank my friends Carsten, Andreana and Théo for the emotional support given during the pandemic and the "illegal" dinner parties, which were in more than one occasion interrupted by the police. It takes a foreigner to understand how hard isolation can be, especially when you are so far from home.

Finally, to my nephews, my mother, my sister, my brother and brother-in-law, as well as my grandparents and my father Víctor Javier who I'm sure were looking after me from the deepness of space among the stars, I would like to say them: thank you, this is for you.

Karlsruhe 2023

Víctor Alfonso Gracia Medrano Bravo

1   Introduction and state of the art

In the literature, there are several works centering on the modelling of mass transfer during drying of films composed by polymer solutions, dispersions, and polymeric dispersions. The drying phenomena and their causes have been analyzed and experimentally validated for spherical particles. This chapter intends to give an insight in to recent advances in the production of polymer spherical and nonspherical particle composites. The basics of coating and drying as well as the transport anisotropy caused by particle shape are presented. This will be used as a framework in the next chapters. Additionally, the objectives and working hypothesis are defined with the systematic investigation that will verify or falsify it.

1.1   Polymer-particle composites

The application of polymer films with embedded particles has caught the attention of the industry in the last decade, mostly because of the improvements embedded particles can achieve in an already functional polymer film[1]. Some examples of composites include lithium-ion batteries[2,3], printable electronics[4,5], fuel cells[6,7], biosensors[8,9], and antibacterial coatings [10,11], to name a few. There are models describing the formulation, coating and drying of composite films with the consideration that the particles are spherical and monomodally dispersed. This does not always correspond with many technically relevant material systems[12,13]. Especially when considering an equivalent diameter or simplifying the problem to a spherical geometry.

Graphene is an example of nonspherical particles for such composite materials. Its discovery became a turning point in material science[14,15], due to its flat and atom-thin geometry which allows electrons to jump easily from the valance to the conduction band[16,17]. This discovery sparked the production of gas sensors[18], electronics[19], membranes[20] and batteries[21]. Moreover, nonspherical particles like graphene tend to stack themselves differently in complicated patterns during processing, leading to a change in the physical properties, which affects the overall quality of the final product. For example, graphene-based membranes for the treatment of residual water tend to have a better performance when the graphene

flakes are arranged in an orderly manner, in comparison to a randomly stacked configuration.[22]

Moreover, the properties of graphene-doped composites [23] depend on the angle of the particles. During the formulation step, graphene particles are randomly oriented due to Brownian-like rotation, but during the casting stage it is possible to align the particles in the film by applying pressure. By having the particles more packed in the membrane, the selectivity can improved, due to the reduced mobility of certain ions as shown by Tsou et al.[22] Likewise, the conductive electron layer is also be affected by the direction the particles are pointing. Graphene composites with a conductive polymer, like PEDOT:PSS, produce an electrically conductive ink for the production of transparent electrodes, whose electric conductance depends on the orientation angle [24].

Another application of plate-like particles can be found in antibacterial coatings, normally used to reduce bacterial activity and to increase the biocompatibility of prosthetics. In an experimental study utilizing silver nanoparticles with three different geometries (spherical, rod-like and plate-like) as antibacterial agents, it was concluded that the effectiveness in inhibiting bacterial growth comes from the ability to maximize the contact area of the particles[11]. Meaning not only the particle shape is important, but the distribution of the particles plays a major role.

Furthermore, the quality and functionality of composites is also dependent on the interactions with the polymer binder, which influence the morphology of the product. The microstructure of the composites is classified in the literature depending on interactions between components. In Figure 1.1, the schematic representation of the different types of microstructures for plate-like particles[25,26] is shown. The plates are exfoliated, if they are completely delaminated and far apart from each other, so that any periodic arrangement cannot be identified. This occurs when the interactions with the polymer chains overcome the electrostatic forces between the particles[27]. If the polymer can mingle between the particles but some periodic structures can still be found, the microstructure is said to be intercalated. There is also the possibility while formulating that both polymer and particle do not intermix at all and interactions are between sets of particles and the polymer chains. This structure is also known as microcomposite. It is common to formulate the composite dispersion by firstly

2

combining the solvent and the particles and later adding the polymer. Usually the process is accompanied by heating and ultrasonic treatment to achieve a completely exfoliated structure[28,29].

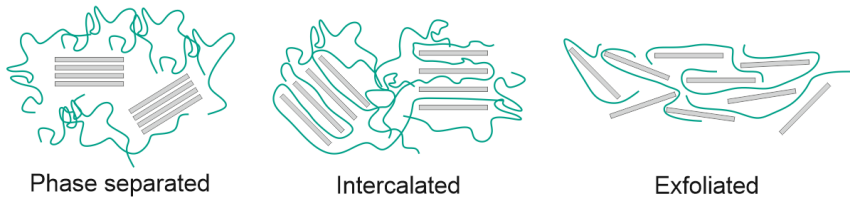Phase separated   Intercalated   Exfoliated

Figure 1.1 Graphical representation of different configurations of polymer-plate-like particle composites based on the component's interactions. Phase separated when the particle-particle interactions are strong, and the polymer interacts with cumulus of particles. Intercalated when the polymer can interact with individual particles, but the particles can still interact. Exfoliated when there are almost no interactions between particles.

At an industrial scale there are two common processes to create composites, namely the hot pressing and tape casting methods. The first process involves casting the components in batches as a powder and later increasing the temperature and applying stress to combine the species into a homogeneous film[30]. The other method, tape casting, is a continuous roll-to-roll process. It consists of a moving carrying substrate on which a liquid composite dispersion is coated and subsequently dried[31]. In the context of this work, a laboratory-scale process analogue to tape casting is studied, in which a dispersion is cast on a substrate using a coating blade and subsequently dried.

1.2   Drying of polymer films

Thin polymeric films have been part of our lives since the last century and can be found in several everyday products. Some examples include plastic foils[32], paintings[33], and adhesives[34]. Most of the production of polymer films consists of the formulation of the mixture by either dissolving or dispersing the polymer in a solvent, to be later coated onto a substrate and subsequently dried. The last two steps carry most of the production costs, and must, therefore, be modeled when designing and optimizing coating and drying processes. Polymer films undergo three main steps

during drying: the mass transport of the liquid solvent from the bulk to the phase boundary, the evaporation of the solvent at the surface of the coating, and the mass transfer of the solvent vapor from the phase boundary to the atmosphere.

The modeling of diffusion coefficients between pairs of polymers and solvents has been studied utilizing different approaches. Modelling the polymer molecules as bead-spring chains[35,36] predicts that the diffusion coefficient of solvents in polymers is proportional to the inverse square root of the polymer molar weight $D_{P,S} \sim 1/\sqrt{\widetilde{M}_P}$, this correlates well with experiments[37]. The equation from Vrentas and Duda can calculate diffusion in dilute polymer solutions using free volume theory as a foundation[38]. However, more empirical expressions have been utilized due to the lack of binary parameters in data bases necessary to use free volume theory models. One example can be found in equation (1.1), the parameters A, B and C in this expression can be fitted directly for drying experiments[39], making it dependent on the solvent loading X_S.[40–44]

$$D_{P,S} = \exp\left(-\frac{A + BX_S}{1 + CX_S}\right) \qquad (1.1)$$

In case of multicomponent systems, the Onsager approach[45] allows us to quantify the diffusive interactions between polymers by using the entanglement degree of the polymer chains. This approach can recreate experimental observations of ternary polymer-polymer-solvent systems with excellent agreement.[46] On the other hand, the presence of more solvents can be modelled using equation (1.1) in an ideal way by a model proposed by Siebel, Scharfer and Schabel, which requires adding the loading values of the solvents[47].

The evaporation of the solvent at the surface of the film can be estimated by integrating the Stefan-Maxwell equation and solving for the solvent flux.[48] Equation (1.2) is the resulting expression for the evaporation of a single solvent. The solvent transport is caused by the concentration gradient between the surface $\tilde{y}_S^*$ and the atmosphere $\tilde{y}_S^\infty$. At the phase boundary it is considered that liquid is in equilibrium with its vapor. The mass transport coefficient $\beta_{S,gas}$ is dependent on the conditions at which the dryer operates, and can be calculated from correlations found in the

literature[49]. Thus, the mass flux $\dot{m}_S$ is a function of the thermodynamic equilibrium between the liquid and its vapor and the transport properties.

$$\dot{m}_S = \beta_{S,gas}\widetilde{M}_S\tilde{\rho}_S \ln\left(\frac{1 - \tilde{y}_S^{\infty}}{1 - \tilde{y}_S^*}\right) \qquad (1.2)$$

Using a dynamic diffusion equation, the concentration of each species during drying is computed, as shown in expression (1.3), with solvent evaporation at the top of the film and impermeable substrate at the bottom as boundary conditions. The main challenge of this approach is the moving boundary due to the solvent leaving the film. It could be solved by adding an extra equation for the change in the limits of coordinate z. However, the expression would still be coupled with the solvent content off the film which would increase the computation times.

$$\frac{\partial \tilde{c}_i}{\partial t} = \frac{\partial}{\partial z}\left(D_{i,j}\frac{\partial \tilde{c}_i}{\partial z}\right) \qquad (1.3)$$

Saure and Schlünder proposed a physical approach based on polymer coordinates to solve the equation. The movement of the species is referenced with the polymer volume velocity instead of the average volume velocity[50]. A graphical summary of this approach can be found in Figure 1.2. After changing the molar fluxes as polymer-related, equation (1.3) is given in terms of the solvent loading, the polymer-based diffusion coefficient $D_{i,j}^P$ and the polymer volume fraction ϕ_P, as it follows:

$$\frac{\partial X_S}{\partial t} = \frac{\partial}{\partial \zeta}\left(D_{P,S}^P\phi_P^2\frac{\partial X_S}{\partial \zeta}\right)$$

where, $\qquad (1.4)$

$$\frac{\partial \zeta}{\partial z} = \phi_P$$

Equation (1.4) has fixed boundaries, thus uncoupling the evaporation problem from the coordinated system. This approach has been experimentally validated with drying experiments using methanol based polyvinyl acetate films, having a remarkable agreement[41,43,50,51].
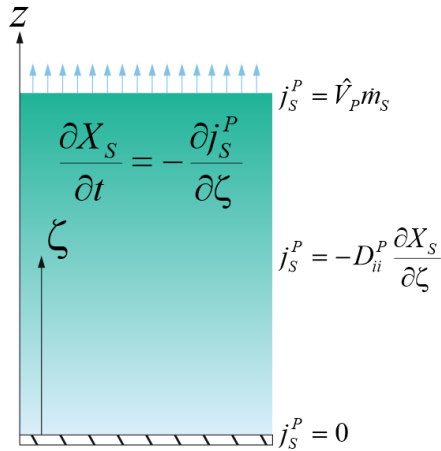
Figure 1.2. Graphical representation of the polymer coordinate approach showing the boundary conditions and the change to the fix coordinate ζ.

Schabel et al.[42] conducted in-situ drying experiments of thin polymer films utilizing Inverse Micro Raman Spectroscopy to measure the solvent concentration in transparent films at different points in the sample, thus, experimentally validating the concentration profiles obtained by the model[43]. Scharfer et al.[44,52,53] used the same model to describe the solvent intake (swelling) in a polymer membrane. It also has been used to determine diffusion coefficients in multicomponent systems[41,46,54] showing good agreement and the flexibility of the approach.

1.3 Drying of colloidal dispersions

Another approach for understanding the drying of polymer films is by considering the coiled polymer chains as dispersed spherical colloidal particles, also known as lattices. Routh and Zimmerman have conducted an extensive experimental and theoretical analysis on the drying behavior of lattices. Mainly on the evolution from a stable latex into a clearer, continuous and mechanically stable polymer film[55]. In their work it is shown how the particle distribution is mainly controlled by the Péclet number, defined for colloidal particles in equation (1.5).

$$Pe_C = \frac{\dot{E}h_0}{D_{C,0}} = \frac{6\pi\eta_S Rh_0\dot{E}}{\kappa T} \qquad (1.5)$$

In this case, the main drying conditions are given by the temperature T, the particle radius R, the liquid viscosity η_S, the solvent's drying rate $\dot{E}$ and the film's initial height h_0. If Pe_C is lower than unity, the diffusion driving forces are dominant, meaning that particles which may accumulate at the surface of the film, diffuse to the bulk creating uniform particle profiles, whereas for Pe_C greater than unity, drying will create particle concentration gradients.

The simulation model of Routh and Zimmerman[55] considers neutrally buoyant particles with the effects at the edges of the film being neglected. Therefore, particle transport takes place only in the direction of the film height, and it is only caused by the movement of the drying front and particle diffusion. Studies on horizontal drying fronts can be found elsewhere. [56,57] Moreover, colloids start to stack themselves in the final stages of drying in a random manner towards close packing. This causes transport properties like the diffusion coefficient to diverge, when reaching a certain volume fraction value.[58] The model uses a concentration-dependent particle diffusion coefficient $D_C(\phi_C)$, shown in equation (1.6), to match the physics of the divergence. It is composed of the Stokes-Einstein diffusion coefficient $D_{C,0}$, a term for describing the concentration dependency $K(\phi_C)$, which will be subject of study in the following chapters, and the compressibility of the dispersion $Z(\phi_C)$ which diverges when reaching a close packing $\phi_C \to \phi_{C,max}$.[59]

$$D_C(\phi_C) = K(\phi_C)\frac{d}{d\phi_C}[\phi_C Z(\phi_C)]\,D_{C,0}$$

where, $\qquad\qquad\qquad\qquad\qquad\qquad\qquad\qquad$ (1.7)

$$Z(\phi_C) = \frac{1}{\phi_{C,max} - \phi_C}$$

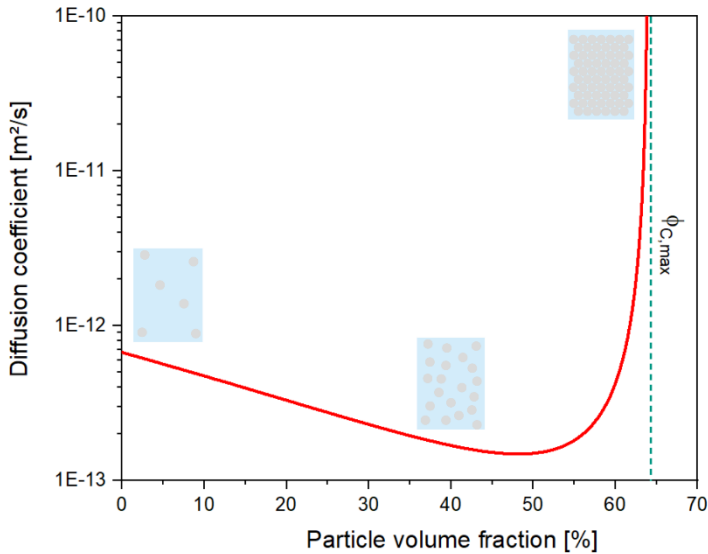*Figure 1.3. Diffusion coefficient of $1\,\mu m$ spherical particles in water at $T = 20\,°C$ as a function of the volume fraction using equation (1.7), showing the infinitely diluted value $D_{C,0}$ at $\phi_C \to 0$ from Stokes-Einstein, and the divergency of the diffusion coefficient at close packing $\phi_C \to \phi_{C,max}$.*

In Figure 1.3, the diffusion coefficient of $1\,\mu m$ spheres in water at $T = 20\,°C$ is plotted as a function of the particle volume fraction. In the diagram, the values at infinite dilution and close packing concentration are shown. The divergence of the diffusion coefficient when $\phi_C \to \phi_{C,max}$ allows the particle volume fraction to remain below this critical value.

The implementation of $Z(\phi_C)$ produces reasonable concentration profiles with a particle saturation at the film surface when the Péclet numbers are high ($Pe_C \gg 1$) and without exceeding the value of the packing concentration, whereas at intermediate values of Pe_C the scale of the concentration gradients corresponds to an order of magnitude of $\nabla\phi_C \sim O\left(\sqrt{Pe_C}\right)$. The concentration profiles were later experimentally validated, with a good agreement.[60]

Skin formation may be the most interesting phenomenon observed experimentally and described by this model[61–63]. Skin formation is defined

as an extreme segregation of the particles, where the film is divided in to a dried polymer at the surface and a liquid underneath it, causing the solvent evaporation rate to plummet due to the polymer film mass transport resistance. Moreover, the deformations caused by rapid particle accumulation could lead to film defects. One major example is crack formation, where the flow of the solvent through the region of the film at close packing causes a pressure drop, leading the film to release the built tension by splitting itself, thus creating cracks.[64,65]

Other works on the drying of dispersions used this diffusion model as a framework for further investigations, due to the good agreement with experimental observations[66,67]. The present doctoral thesis also benefits from it and applies it accordingly, as it is explained in the next chapters.

1.4   Drying regime maps

Cardinal et al.[66] further developed the model of Routh and Zimmermann by considering buoyant particles. This work examines the influence of sedimentation on the particle distribution. To quantify the contribution of sedimentation to the overall drying process, the sedimentation number N_S is introduced. It is defined as the ratio between the Stokes sedimentation velocity $U_{C,0}$ and the initial evaporation rate, as shown and compared with Pe_C in equation (1.8).

$$Pe_C = \frac{\dot{E}_0 h_0}{D_{C,0}} \quad N_S = \frac{U_{C,0}}{\dot{E}_0} \qquad (1.8)$$

In the approach of Cardinal et al., the drying process is controlled by two nondimensional quantities. If Pe_C is higher than unity and N_S lower than unity, the evaporation (**E**) is dominant. If Pe_C and N_S are lower than unity, the diffusion (**D**) is dominant. If N_S and the product of the two numbers is higher than unity $Pe_C N_S > 1$, then sedimentation (**S**) is dominant. In their study, the particle mass transfer during drying was simulated and different particle distributions were generated by systematically varying the values of the Péclet and sedimentation numbers. The complete derivation of the simulation is given in the appendix of this work in section 7.1.

Moreover, the particle concentration was graphically summarized as a function of the drying conditions given by Pe_C and N_S. In Figure 1.4, the simulation results are plotted in blue. The blue borders are obtained by testing if the combination of dimensionless quantities give $90\,\%$ of the close packing concentration ($\phi_C = 0.9 \cdot \phi_{C,max}$) either at the top or the bottom of the film, after a time proportional to half of the difference between the initial concentration and the packing concentration, as follows.

$$\tau_{max} = \frac{\phi_{C,max} - \phi_{C,0}}{2\phi_{C,max}} \qquad (\,1.9\,)$$

This diagram is known as a drying regime map and shows three possible vertical particle distributions. If the evaporation of the solvent is dominant, the particles will accumulate at the top of film, this is known as the (**E**)vaporation regime. If sedimentation of the particles is dominant, the particles will sink to the bottom and gather there, this known as the (**S**)edimentation regime. If neither sedimentation nor evaporation are dominant, the diffusion coefficient can counter any given concentration gradient within the film, maintaining the concentration uniform along the film, therefore this is called the (**D**)iffusion regime.
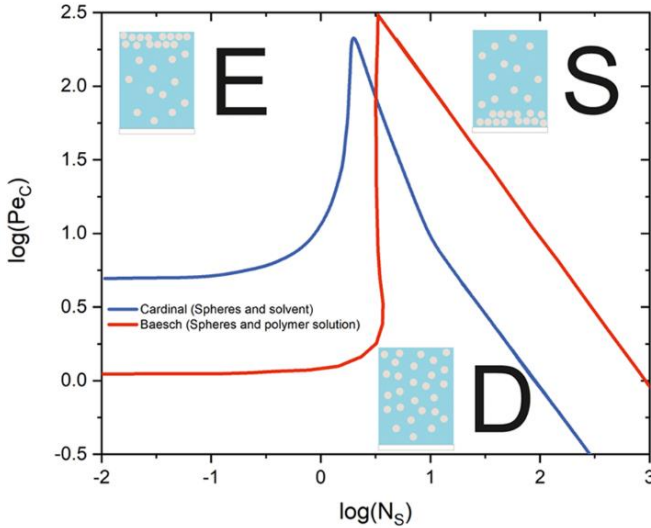
*Figure 1.4. Drying regime map for spherical particles with no binder (blue) and with a dissolved polymer (red), showing the three drying regimes: **E**vaporation: particles on top, **D**iffusion: particles evenly distributed and **S**edimentation: particles at the bottom. Extracted and adapted from Cardinal et al. Francis and Baesch et al. Scharfer, Schabel.[66,68,69]*

The drying regime map was validated experimentally, in which spherical silica particles with different sizes were dispersed in distilled water at different concentrations, cast on a substrate and dried at different conditions. After a given time, the drying was stopped, and the sample was frozen in liquid ethane for further investigation.[66] The film was cut in half and the cross section analysed using a scanning electron microscope (SEM). This technique is known as Cryo-SEM[70], and proved to be resourceful, because the obtained images can be quickly analysed. The experimental particle distribution was in good agreement with the predicted distribution from the drying regime map. This chart can be used for fast-track dryer sizing. Nevertheless, if the dispersion has a polymer binder, the predicted particle distribution could be inaccurate. This is due to the change in solvent concentration at the phase boundary, which will influence the drying rate, whereas in the simulation model the drying rate is considered constant.

In the work by Baesch et al.[50], it was determined how the presence of a polymer affects the final particle distribution in a dry film. The ternary systems polystyrene–polyvinyl alcohol–water (PS-PVA-H_2O) and silica–polyvinyl alcohol–water (SiO_2-PVA-H_2O) were investigated. One of the main conclusions was that at a certain polymer concentration, the mass transfer of a ternary polymeric dispersion can be modeled as a binary system: Instead of considering the solvent and polymer as two different components, the polymeric solution can be treated as one pseudo-component[71].

The core principle of this approach is based on the component size and diluted state of the coating dispersion. The low concentration reduces the interactions between the particles and the polymer chains. Moreover, the difference in size between the particles and polymer chains, and between the particles and solvent molecules, are on the same order of magnitude. Therefore, the particle-polymer and particle-solvent interactions are considered to be on the same order of magnitude. This principle is valid until the solvent concentration is too low, such that it to allows the polymeric chains to interact with each other, known as the overlap concentration. This concentration can be obtained experimentally by measuring different physical properties like the viscosity of polymer solutions as a function of the polymer content.[72] In Figure 1.5, an example of the overlap concentration measurement is displayed, showing the diluted and concentrated cases. On the left side of the diagram the viscosity increases as the polymer content increases, at a logarithmic scale this increase follows a constant slope. Once the overlap concentration is reached, the slope increases, changing the trend of the viscosity. In the appendix off this work in section 7.2.1, an example for the material system PVA-H_2O can be found.
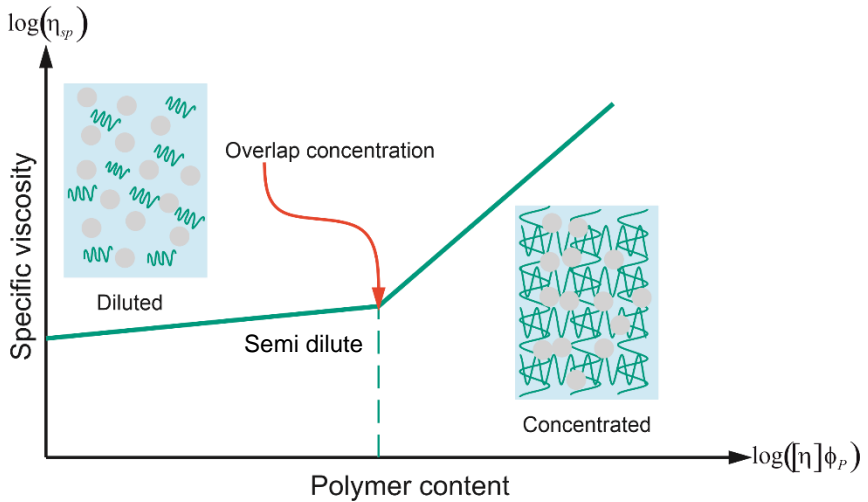
Figure 1.5. Specific viscosity of a polymeric dispersion as a function of the polymer content, showing the diluted regime where the polymer-particle and particle-solvent interaction are the same, and the concentrated regime where the polymer chains are entangled and there is no relative particle movement.

The kinetics between the polymer and the particles was investigated for the stability of the dispersion. Baesch[73] determined that the adsorption of the polymer on the particle surfaces, although it could help maintain the dispersion stability while coating, it also leads to the formation of agglomerates and thus a radical change in the particle transport properties.[50] Therefore, the polymer chains must remain with minimal adsorption to hinder the formation of agglomerates. This was realized by controlling the hydrogen potential using diluted ammonia buffer solutions at $pH = 9$. Additionally, the rheological properties of the polymeric solution were determined as a function of the polymer concentration.

Mathematical modelling of drying is done by combining the conservation equations of the dispersion and polymer drying using a quasi-binary approach, which is the framework for the modelling in the present work (see Chapter 3). This approach leads to a partial differential equation system consisting of three coupled equations with third type boundary conditions, which can be solved numerically (see Appendix 7.1). Using similar conditions, the drying regime maps were drawn by simulating at different Pe_C

13

and N_S until the particle concentration reached the desired regime, as depicted in Figure 1.4. The time needed to reach the corresponding concentration was changed to the time needed to obtain the overlap concentration, thus explaining the shift of the border between the Evaporation and Diffusion regimes.

Baesch et al. conducted the experimental validation in an in-situ and ex-situ manner by performing coating and drying experiments and later investigating the films with Cryo-SEM and 3-D Raman Spectroscopy. Both types of experimental approaches were shown to be suitable to determine the particle concentration at a given point during drying or in the dry film. Unlike Cryo-SEM analysis, the determination of the concentration in a dry film using Raman spectroscopy is non-invasive, there is no need to cut the film in half and it provides a 3-D image of the film. However, it only works if the sample is transparent or translucent enough to allow light transmission and to not overly scatter. Therefore, the particle distribution for the material systems like PS-PVA-H_2O cannot be determined during drying due to the turbid appearance of the coating dispersion.

By plotting the experimental drying conditions in the drying regime maps, the modelling was validated and in most of the cases the experimentally determined particle distribution corresponds to the regime predicted by the simulation. Nevertheless, the simulation approach has limitations, such as not calculating the particle concentration at high Pe_C values. Also due to the presence of a polymer, a second Péclet number is needed with the polymer diffusion coefficient at infinite dilution $D_{P,S,0}$ as shown in equation (1.10). This means a fourth regime while drying could be possible, where the polymer concentration increases at the phase boundary.[50]

$$Pe_P = \frac{\dot{E}_0 h_0}{D_{P,S,0}} \qquad (\,1.10\,)$$

Nevertheless, in order to reach this case, the drying rates must be higher than the rates needed for the Evaporation regime, mostly due to the higher polymer mobility. In comparison, the diffusion coefficient for a $1\ \mu m$ particle in a $3\ \%\ v/v$ PVA water solution at $T = 40\ °C$ is $D_{C,0} = 4.2 \cdot 10^{-14}\ m^2/s$, and the polymer diffusion coefficient of PVA in water at the same temperature at infinite dilution is $D_{P,S,0} = 3.3 \cdot 10^{-13} m^2/s$ (see Section 7.3), one order of magnitude higher. Thus, simulating this regime

would require an immense Pe_C, surpassing the capabilities of the simulation computer program. Moreover, even though the simulation can calculate the concentration of all components after the polymer overlap concentration is reached, these values are no longer valid due to the solidification of the polymer film.

1.5   Particle shape and anisotropy

Non-spherical particles can be categorized into two main sets, namely as deformed spheres that have been either flattened or stretched, as shown in Figure 1.6. Such shapes are named rotation ellipsoids, because they can be obtained by rotating a two-dimensional ellipse, meaning that two of the three ellipsoid's semi-axes have the same length. Oblate ellipsoids (plate-like) are therefore obtained by rotating around the shorter axis (semi-minor axis), whereas prolate ellipsoids (rod-like) are drawn by rotating around the longer axis (semi-major axis). Thus, their sphericity is quantitatively calculated using the aspect ratio r_p defined by equation (1.11), where a is the vertical axis and b the horizontal axis. If $r_p < 1$ the particle is plate-like, if $r_p = 1$ the geometry is spherical, and if $r_p > 1$ the particle is rod-like.

$$r_p = \frac{a}{b}$$

(1.11)

$$r_p < 1 \qquad\qquad r_p = 1 \qquad\qquad r_p > 1$$

Oblate Ellipsoid   Sphere   Prolate Ellipsoid
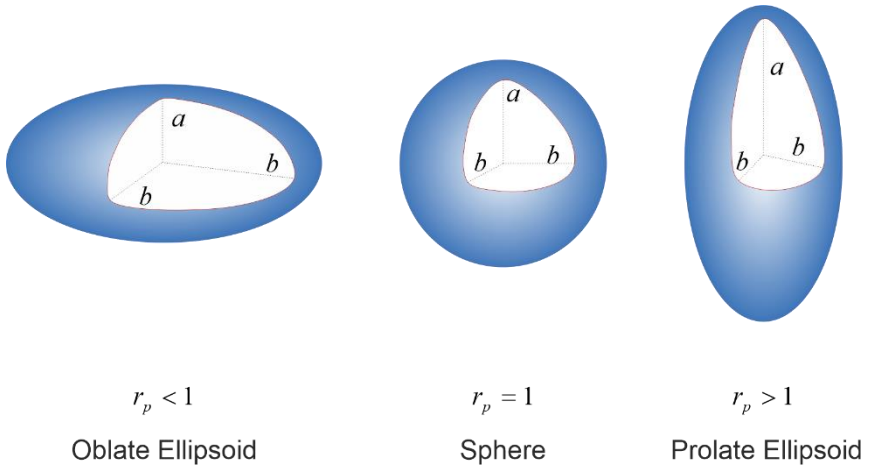
Figure 1.6. Classification of particle geometry according to the aspect ratio r_p. Oblate at $r_p < 1$, spherical at $r_p = 1$, and prolate if $r_p > 1$.

One notorious modification, caused by using nonspherical particles, is the change in the maximal packing concentration $\phi_{C,max}$, namely the maximal volume fraction the particles can achieve. As previously mentioned. This depends heavily on how the particles stack themselves during drying and settling. Spheres have two main orderly configurations while stacking, face-centered cubic (FCC) and hexagonal closed packed (HCP), which have a packing concentration of ~74 %, whereas a random or disordered stacking of spheres can have a maximal volume fraction of 64 %.

Unlike spheres, the maximal packing concentration of plates and rods are also dependent on the orientation they have. If the particles are aligned during drying, they could occupy more space than spheres in the polymer matrix. However, a random or time-dependent orientation of the particles could have a dramatic effect on $\phi_{C,max}$. This is crucial for the prediction of the particle distribution, because the definitions of the drying regimes borders are based on reaching 90 % of the maximal particle concentration. Therefore, $\phi_{C,max}$ is regarded as an input parameter for the simulation model (see Section 3.4).

The work of Chaikin et al.[74] gives an insight on how plates can randomly arrange themselves, and contains a chart to obtain $\phi_{C,max}$ as a function

of the aspect ratio r_p, as depicted in Figure 1.7. The packing simulations in this work used the "Paris parking" approach[75]. It is named after the way cars are parked over the curb in European cities, which, in the USA, is not usual or can even be prohibited. The particles are arranged with a random angle on a line putting its center over it, and without overlapping them. Depending on the space left unused, the packing concentration was determined. As previously mentioned, in an orderly fashion the particles that are flatter could use more space, filling the voids and increasing the packing concentration. Nevertheless, even by choosing low angles randomly, plates with low aspect ratio have a large drop in $\phi_{C,max}$.
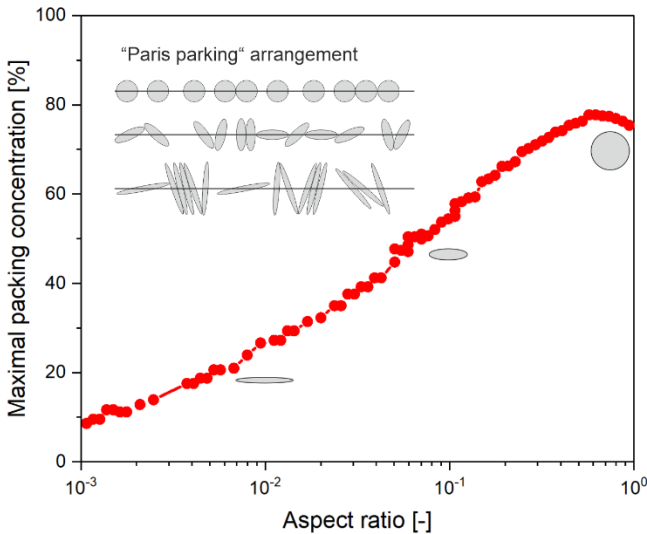
Figure 1.7. Maximal packing concentration $\phi_{C,max}$ as a function of the aspect ratio r_p for plate-like particles at low angles. Extracted and adapted from Chaikin et al.[74]

If the particles were to be aligned with the same angle, it will introduce another phenomenon to be considered, known as anisotropy. The anisotropy in material science can be defined as the difference of the physical properties depending on the direction it is being measured, meaning that a property cannot be quantified as a number or scalar, like in an isotropic material. Instead it must be measured and modeled in all the possible

directions. In a cartesian three-dimensional space, there are nine possible direction combinations, which will transform properties as viscosity, heat conductivity and mass diffusion into second order tensors[76].

In process engineering the most common examples of this phenomenon can be found in composite wall and thermal composite coatings problems for calculating the effective heat transfer[77]. Similarly, anisotropy in diffusional mass transfer is applicable in the modeling and operation of fuel cells with composite membranes[78]. But the most important application of a diffusion tensor is found in medical imaging.[79] By extracting the diffusional behavior of a substance across a tissue, it is possible to obtain information about its structure and thus a three-dimensional picture can be drawn. In Figure 1.8, the graphical explanation on how diffusion in isotropic and anisotropic porous systems works is shown. For isotropic materials there is no given order or pattern to follow, and the diffusion of a species through the material will be given by the porosity and the tortuosity as an effective diffusion coefficient D_{eff}.[80–82] For anisotropic materials, if the pores are arranged like in the left side of Figure 1.8, a species diffuses faster through the material from left to right than from top to bottom, meaning $D_\perp < D_\parallel$.[83]
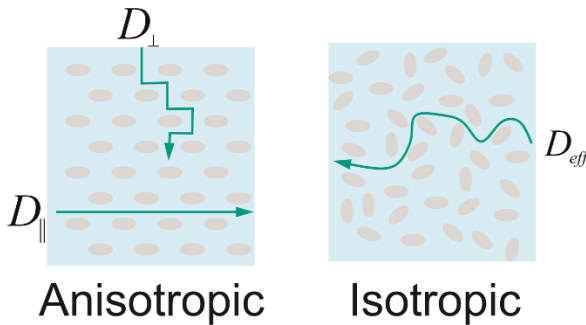
Figure 1.8. Graphical description of an anisotropic and isotropic material, showing the difference of the diffusion process at different directions (parallel and perpendicular).

1.6   Objectives and working hypothesis

The aim of the present work is to investigate the influence of particle shape on the particle distribution in a dry film, by simulating the component mass transfer during drying and experimentally validating the predicted concentration profiles using plate-like particles. The working hypothesis is that a change in the particles geometry will affect the component distribution during the coating and drying processes. Nevertheless, the particle distribution and drying regimes found in the literature can still be applied for plate-like particles by adapting and further developing the state-of-the-art quasi-binary simulation model. Thus, new drying regime charts can be drawn after adjusting the sedimentation and diffusion coefficient accordingly. To falsify or verify the hypothesis, a material system is selected and its physical properties are characterized. Later, using the obtained physical information of the material system, the state-of-the-art simulation is adapted and new drying regime maps can be plotted and experimentally validated.

Figure 1.9 shows the summarized sequence for producing a polymer-particle composite film. In each step, the most important property is labeled. First, a stable dispersion capable of producing a homogenous wet film is formulated. Experimental validation requires the selection of a suitable material system that allows measurement of the particle orientation. In this work, a transparent material system responsive to Raman radiation is chosen in order to use the available spectrometer and the analyzing software. During coating the particles rotate and their angle of orientation will influence their mobility. Afterwards, drying takes place where the boundary conditions: solvent evaporation rate, initial wet film height, and initial component concentration, dictate the mass transfer of the components. Finally, once the composite films have been dried, the final distribution can be determined to validate or reject the adapted simulation model.
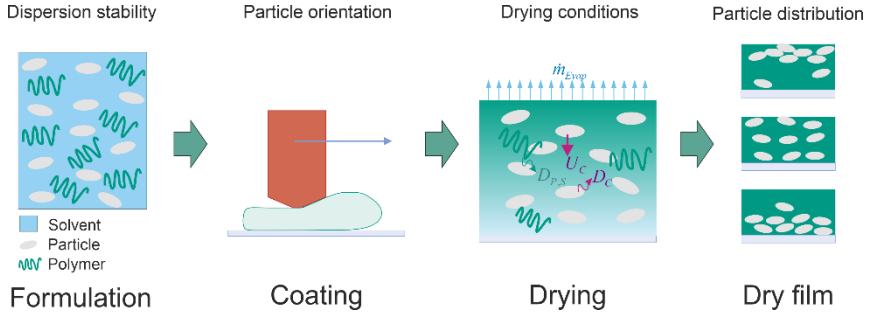
Figure 1.9. Graphical summary of the sequence of the production of polymer-particle composite films utilized to investigate the influence of the particle geometry on the particle distribution.

One of the main challenges of this work comes from the adaptation of the model, which requires the characterization of dispersions with non-spherical particles. This is mostly due to the orientation angle of the particles being an unknown variable. Determination of the particle orientation is achieved by conducting a theoretical study on the hydrodynamics of plate-like particles, during and after the coating step. This can be achieved by making a force balance on the particle surface depending on the fluid movement. While knife coating leading to a Couette flow can be considered and therefore a simple shear is used to determine the overall stress on the particle surface. The orientation of the particles is simulated, and needs to be experimentally validated by knife coating a dispersion and evaluating the particle angles via 3-D Raman spectroscopy or Cryo-SEM. Depending on the particle arrangement, the transport properties can be modeled accordingly.

Using the simulation for spherical particles, the concentration of the species at different drying conditions is calculated. By systematically varying the drying conditions, it is possible to draw new drying regime charts, in which the positions of the borders are dependent on the particle shape r_p. These new drying regime maps are validated by casting polymer films using knife coating, consequently drying them and investigating the component distribution via Raman spectroscopy. Thus, the working hypothesis can be validated of falsified.

2 Experimental Methodology

In this chapter, the methods and devices, which are used to obtain the physical properties of the composites and validate the simulation, are explained. First, a plate-like particle-polymer system is chosen accordingly to the measurement capabilities. Then, the system is characterized by measuring the required transport properties of each component, namely the viscosity of the polymer solution, the viscosity of the polymer-particle dispersion and the particle sedimentation rates. Afterwards, the particle orientation after coating is investigated using Scanning Electron Microscopy and 3-D Micro Raman spectroscopy to calculate the diffusion and sedimentation coefficients accordingly. The data obtained from the material system characterization is used in the next chapter to run the simulation.

The validation of the simulation requires drying experiments, which are conducted by casting the coating dispersion onto thin glass substrates. By systematically changing the drying rate and initial film height, a segregation of the particles at different parts of the film is caused. The resulting composite dried films are investigated using 3-D Raman spectroscopy. This measuring technique allow us to indirectly measure the concentration of each component in a noninvasive manner. This is done by fitting the sample spectrum with those of the pure components. Using a calibration curve, it is possible to convert the Raman intensity ratio into a mass loading. Thus, making it possible to verify or reject the simulated particle distribution.

2.1 Characterization of the material system

Polyvinyl alcohol is chosen as the polymer due to its mechanical strength and the abundance of experimental data obtained from previous works[84,85]. Glass flakes are selected as the plate-like particles due to their transparency, which allows being measured using Raman spectroscopy. Moreover, the flakes are commercially available, and can be purchased with a narrow particle size distribution. The monomodal distribution allow us to assume a constant particle aspect ratio r_p and to use

state-of-the-art simulation model as a framework, without making major changes.

The following properties of the material system were determined and are explained in detail in this chapter.

- Polymer solution viscosity. The particle diffusion and sedimentation are strongly dependent on the medium viscosity. During drying, the viscosity changes due to the loss of solvent. The concentration dependency on the solution viscosity is determined (see Section 7.2).

- Dispersion viscosity. One of the challenges in describing the diffusion and sedimentation of particles in a liquid mixture is the determination of the particle concentration influence on the transport properties. A first approach is to use the most common models available in the literature (Batchelor and Krieger-Dougherty) and to investigate if the models describe the viscosity correctly. If the models are proven to be accurate, then it could be inferred that the other transport properties could also be calculated using these or similar expressions.[86,87]

- Particle orientation. The viscous resistance acting on the moving particles is dependent on how the plate-like particles are oriented. If they were orthogonally positioned to the flow direction, the drag will be at its maximal value. Whereas, if the orientation is parallel to the flow direction, the drag would be at its lowest value. The orientation is experimentally determined to allow the use the of correlations.

- Particle sedimentation velocity. The sedimentation rates in differently concentrated dispersions are measured to determine the particle mobility and thus the diffusion coefficients properly.

2.1.1 Preparation of polymer solution

The solutions were prepared by slowly adding polyvinyl alcohol (PVA 99 % hydrolyzed, Sigma-Aldrich) with a molecular weight of $\widetilde{M}_{PVA} = 89 - 98 \; kg \; mol^{-1}$ in distillated water (Sigma-Aldrich) at room temperature. The polymer dispersion was stirred in small 5 ml flasks (WICOM) for 15 min

to ensure that the polymer is completely dispersed. This step is done to avoid the formation of agglomerates and facilitate the dissolution of the polymer. The temperature was then raised to 70°C and the mixture was continuously stirred until the PVA was completely dissolved, this can be determined when the liquid turns transparent. The samples were stored in a temperature-controlled cabinet until they were used. For the viscosity measurements, the PVA solution was degassed using an ultrasonic bath at room temperature until no bubbles were visible. The samples were used shortly after preparation to avoid gelation or crystallization of the polymer. The binary polymer concentration interval for the samples was from 0 to 17 % v/v. For the drying experiments and sedimentation measurements, the polymer concentration remained constant at $\phi_P = 3\%$

2.1.2   Preparation of dispersion

Glass Flakes (GF001 and GF001-10 Glassflake Ltd.) composed mostly of silicon dioxide SiO_2 were dispersed in aqueous PVA, prepared by using the methodology described in 2.1.1. The Flakes were slowly added and left for 24 hours with continuous stirring to avoid the formation of agglomerates. Shortly before usage, the samples were degassed in an ultrasonic bath at room temperature. The particle concentration interval for the sedimentation and viscosity measurements was from 0 to 6 % v/v, whereas for the drying experiments the concentration had a constant value of $\phi_{C,0} = 2\%$ in the wet film and of $\phi_{C,dry} = 40\%$ in the dry film. The plate-like particles utilized for the drying experiments (GF001-10) had an average length of 10 μm and average thickness of 1 μm, which results in an aspect ratio of $r_p = 0.10$. For the sedimentation measurements, two particle system were used, the one previously described, and bigger flatter particles (GF001) with an aspect ratio of $r_p = 0.03$.

2.1.3   Viscometry

The measurement of the viscosity was conducted using a cone and plate rheometer (Physica MCR 101 rheometer Anton Paar). The cone utilized had a 60 mm diameter and an angle of 3° resulting in a gap width of $h_{gap} = 154$ μm at the edge of the plate. To prevent solvent evaporation

during the measurements, a 3D-printed solvent trap was used. This allows saturation of the atmosphere around the cone, and thus hinders the evaporation of solvent. All the samples were measured three times and averaged to assure reproducibility. The plate can be temperature-controlled, and the samples were brought to the measuring temperature before the experimental investigation. This is done to maintain an isothermal process. The measured shear rate varied from $\dot{\gamma} = 10^{-3}\ s^{-1}$ to $\dot{\gamma} = 10^3\ s^{-1}$ and back to $10^{-3}\ s^{-1}$, to check for the presence of hysteresis. Every time a measurement was started, the viscosity of water was determined to ensure that the calculations for relative viscosity were accurate. The calculated value of the viscosity was determined by fitting the trend, or averaging the values, at low shear rates, depending on the rheological behaviour of the sample.
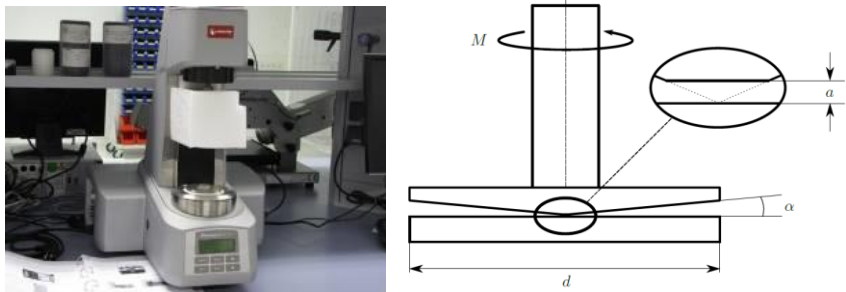
Figure 2.1. Left: photo of the rheometer used for the zero-shear $\dot{\gamma} = 10^{-3}s^{-1}$ viscosity measurements. Right: Set-up utilized showing the characteristic dimensions of the cone-plate system, including torque M, plate diameter, cone angle α and the height of the tip a complementing the frustum.

2.1.4   Zero-shear viscosity

Calculating the diffusion coefficient and sedimentation rate according to the Stokes-Einstein equation requires the medium viscosity. Depending on the material system, the viscosity could be dependent on the type of stress and the deformation rate that it is applied. These types of fluids are known as non-Newtonian and is the case for polymeric solutions, whose viscosity is a function of the shear rate $\dot{\gamma}$. When the shear rate increases, the viscosity decreases, which is known as shear thinning.

For sedimentation, the shear rate corresponds to an order of magnitude of $\dot{\gamma} = 10^{-6} \ s^{-1}$ which is considerably lower in comparison to the shear rates during knife coating or slot die coating, $\dot{\gamma} \geq 10^3 \ s^{-1}$.[88,89] Therefore, the viscosity needed to describe the diffusion coefficient and sedimentation rate during drying must be measured near zero shear rate $\eta(\dot{\gamma} \to 0)$, also known as the zero-shear viscosity. Throughout this work when the viscosity is mentioned, it is referring to this value.

2.1.5   Influence of concentration on the viscosity

The viscosity of the dispersion and its dependence on the particle content is investigated to evaluate if the diffusion and sedimentation of plate-like particles could be modeled in the same manner as dispersions containing spherical particles, thus justifying the use of adapted expressions for the diffusion and sedimentation coefficients. Some of the classic text book models use the relative viscosity to describe the concentration dependence, which is the viscosity of a dispersion divided by the viscosity of the pure solvent η_S as described in equation (2.1).

$$\eta_r(\phi_i) = \frac{\eta(\phi_i)}{\eta_S} \qquad (\,2.1\,)$$

By subtracting the solvent viscosity from the numerator, the so-called specific viscosity η_{sp} is obtained.

$$\eta_{sp}(\phi_i) = \frac{\eta(\phi) - \eta_S}{\eta_S} = \eta_r(\phi_i) - 1 \qquad (\,2.2\,)$$

Moreover, dividing it by the concentration of the solute ϕ_i results in the reduced viscosity η_{red}, which is the ratio between the increase of viscosity and the increase of solute quantity.

$$\eta_{red}(\phi_i) = \frac{\eta(\phi_i) - \eta_S}{\phi_i \eta_S} = \frac{\eta_{sp}(\phi_i)}{\phi_i} \qquad (\,2.3\,)$$

The so-called intrinsic viscosity $[\eta]$ describes the total solvent contribution of a mixture, it is calculated by approaching the solute concentration ϕ_i to zero.

$$[\eta] = \lim_{\phi_i \to 0} \frac{\eta_{sp}(\phi_i)}{\phi_i} \qquad (2.4)$$

Einstein developed a model for η_r of suspensions as a function of the volume fraction of the particles ϕ_C given by expression (2.5)[90]. The model considers a dispersion of rigid spheres at infinite dilution, which means that the particles are separated from each other in the fluid and do not interact. At these conditions, the intrinsic viscosity equals $5/2$.

Einstein: $\qquad\qquad\qquad \eta_r = 1 + 2.5\phi_C \qquad\qquad (2.5)$

This expression has a good agreement with experimental values for dispersions with volume fractions of solids up to 2 %. At higher particle content, the hydrodynamic interactions have to be considered. Batchelor extended the model[91] and the resulting expression can be found in equation (2.6).

Batchelor: $\qquad\quad \eta_r = 1 + 2.5\phi_C + 7.6\phi_C^2 + O(\phi_C^3) \qquad (2.6)$

According to this expression, interactions of the particles are in an order of magnitude of ϕ_C^2. The limitation of this approach is that the interaction of the particles is made in pairs, meaning that cases where more particles interact at the same time or when the spheres are not neutrally charged are not considered. This could cause deviations of the model. Equation (2.7) is a modified version of the Batchelor's model, which attempts to quantify interactions at higher particle content, hence the power-law nature of the expression[88].

Modf. Batchelor: $\qquad\qquad \eta_r = (1 - \phi_C)^{-n} \qquad\qquad (2.7)$

Krieger and Dougherty developed another model using expressions similar to those of Eilers[92] and Mooney[93] as a frame work, and adapted them according to experimental observations. It is displayed in equation (2.8). The model considers the interactions of two particles in a dumbbell arrangement, which can rotate in opposite directions due to the space between them[94]. One important aspect in the equation is the inclusion of the maximal packing concentration $\phi_{C,max}$. This parameter is important to add, due to the divergence of the dispersion's viscosity when approaching this value. Thus, this model is appropriate when describing concentrated systems.

Krieger-Dougherty:
$$\eta_r = \left(1 - \frac{\phi_C}{\phi_{C,max}}\right)^{-[\eta]\phi_{C,max}}$$
(2.8)

In Figure 2.2, the experimental relative viscosity of a dispersion of glass flakes at $40\ °C$ with an aspect ratio of $r_p = 0.1$ and PVA with a concentration of $\phi_P = 3\ \%$ is shown. Moreover, the experimental data is fitted utilizing the Krieger-Dougherty and Batchelor's approach, which both can predict the trend for the viscosity, fairly well.
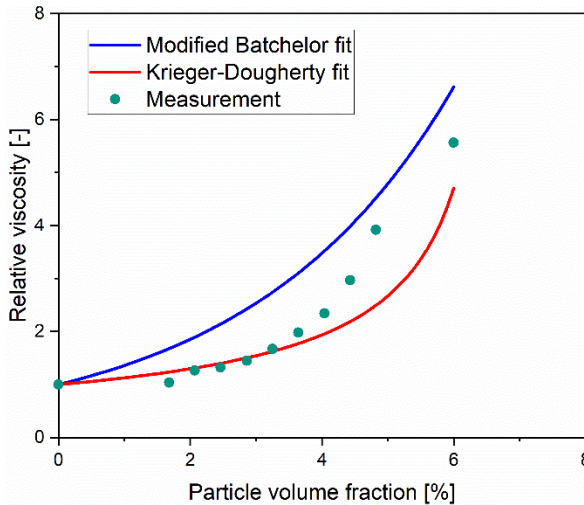
Figure 2.2. Relative viscosity of a $3\ \%$ v/v PVA aqueous dispersion as a function of the plate-like particles volume fraction. The experimental values are fitted using the modified Batchelor model from equation (2.7) and the Krieger-Dougherty model from equation (2.8).

To ensure the Krieger-Dougherty model is describing the physics of the dispersion correctly, $[\eta]$ and $\phi_{C,max}$ were chosen as fitting parameters and later compared. However, the experimentally determined maximal packing concentration $\phi_{C,max,exp} = 7\ \%$ turns out to be considerably lower than predicted by Chaikin et al.[74] ($\phi_{C,max} = 52\ \%$ see Figure 1.7). The significant deviation from the literature value can be attributed to the orientation of the particles, which during low shearing could be assumed as time-dependent. And if the particles have a significantly wide angle of

orientation, the packing concentration falls dramatically. Therefore, in this work the modified Batchelor approach is tested to describe the diffusion and sedimentation coefficients due to its independence from the maximal packing concentration.

For the binary aqueous polymer solution, the viscosity was fitted with an empirical approach due to the complex nature of the polymer chains. The viscosity of an aqueous PVA solution $\eta_{P,S}$ at $T = 40°C$ as a function of the binary (hence the superscript ϕ_i^b) polymer concentration ϕ_C^b is plotted in Figure 2.3. Due to the power-law trend of the viscosity, an empirical expression is chosen to fit the experimental values, as shown in equation (2.9).

$$\eta_{P,S} = A \exp(B\phi_P^b) \ \forall \ \phi_P^b \in [0,13\ \%]$$

where,

(2.9)

$$A = 2.38 \cdot 10^{-3}\ Pa\ s; B = 50.9$$

The range over which the expression is defined is not arbitrarily chosen, it is the diluted zone before the overlapping concentration. The determination of the overlapping concentration for this material system can be found in the appendix, in section 7.2.1.
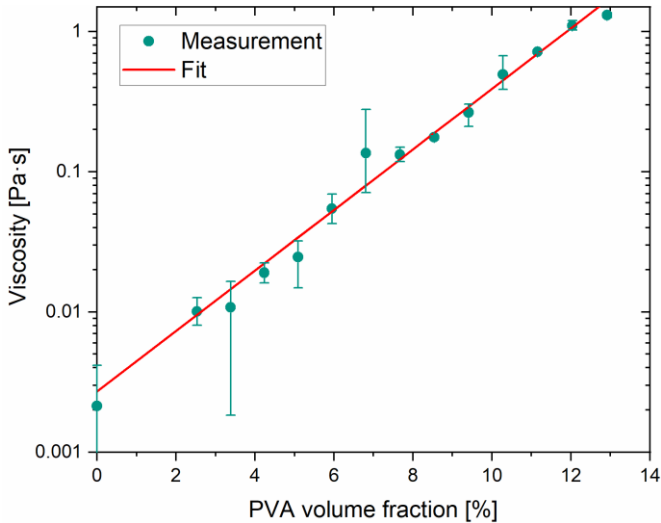
Figure 2.3. Viscosity of an aqueous polyvinyl alcohol solution at $40\ °C$ as a function of polymer content. The experimental data is fitted using the expression in equation (2.9).

2.2 Raman Spectroscopy

The measurement of particle distribution in the dry film is conducted using confocal micro Raman Spectroscopy. This is a noninvasive measuring tool, with the prerequisite that the samples must be transparent in the range of the light source ($\sim500\ nm$), so that if the sample can be investigated at different points inside of it. Transparency is vital to avoid complete scattering of the light whilst passing through the sample. If the component is translucent, there is a small influence of scattering on the measurement.

Radiated light in a transparent or translucent material is scattered by the molecules. A photon can excite a molecule into a virtual quantum state, from this "excited state" the molecules relax again and return to the original state; thus, light is emitted at the same wavelength as the outgoing radiation. The interaction is said to be an elastic collision, also known as "Rayleigh" scattering. Raman also Krishnan discovered in 1928 that some inelastic interaction could also take place, in which the molecule could go

29

after the excitation to an upper or lower energy state (Raman effect), meaning the wavelength of the emitted light changes. If the wavelength is greater, the scattering is called "Stokes-Raman", otherwise is known as the "Anti-Stokes-Raman".

The size of the frequency shift is dependent on the type of the chemical bond. Furthermore, the intensity of the spectral lines is given by the occupation of the energy levels. The intensity is dependent on the wavelength to the power of four. If a mixture from several Raman-active components is irradiated with monochromatic light, it is possible to determine the composition of the mixture by measuring the inelastic collisions.

2.2.1   Experimental Setup

The Raman spectrometer setup used in this work for the concentration measurements and the 3-D images is depicted in Figure 2.4. The setup consists of a microscope cross table (Marzhauser, Tango 3D) under an optical microscope with a 100x oil objective (Neo-Fluar, Zeiss). A diode pumped solid state (DPSS) laser with a 532 nm wavelength (Torus 532 Laser Quantum) is coupled to the microscope via a glass fiber. The laser is focussed to the sample through multiple mirrors and an edge filter. The Raman shifted light, emitted at the same incident angle as the laser light, passes the edge filter on the light path back, while almost all reflected, or Rayleigh scattered light is backscattered at the edge filter. The Raman light is directed via an adjustable pinhole leading into a multimode fiber, which brings the signal to the Raman unit (Jobin Yvon Labram 8). Inside the unit, the signal is sent through a $100\ \mu m$ slit and a grid with a constant of 600 and culminates in a CCD camera.
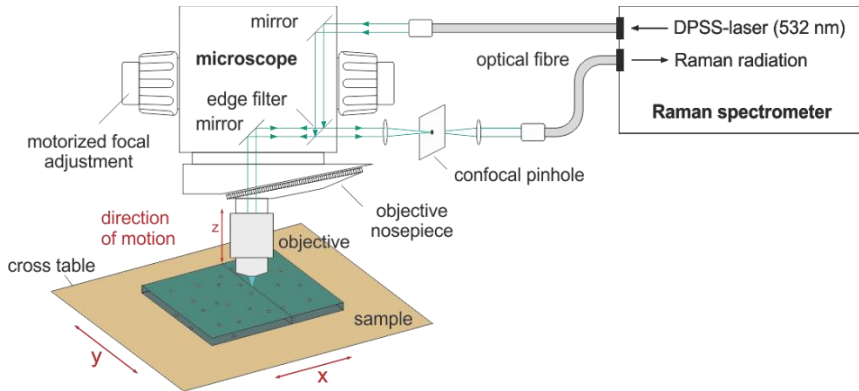
Figure 2.4. Schematics of the confocal microscope coupled with the Raman spectrometer, showing the path followed by the laser and the Raman signal from the sample[68]. The setup is capable of measuring 3-D Raman spectra as described by Baesch.[73]

The three-dimensional measurement is realized by moving the focal point using the motorized cross table and the microscope stage. The samples were prepared using the methodology described in the previous section. The polymer films were placed facing down on to the cross table and fixed into place using adhesive tape. The spectral images can be conducted with a spatial resolution in all directions of $0.5\ \mu m$.

The film imaging was performed by moving the focal point in micrometer sized steps in all three possible directions and measuring the Raman intensity at each given point. All films were investigated in the center of the sample. The samples were exposed to the laser for $5\ s$ at every point to guarantee a sample's spectrum with low background noise and to compensate for the loss of intensity due to scattering while going deeper into the film. The investigated film area in the XY plane was $100\ \times\ 100\ \mu m$, depending on the sample's thickness the overall studied volume varies. The resolution in the lateral direction was $\Delta x = \Delta y = 2.5\ \mu m$ and in the horizontal direction $\Delta z = 0.5\ \mu m$. Due to the processing time, the scan of a film can take between 24 to 72 hours, depending on the film thickness. The software (LabSpec5.91) integrated with the spectrometer is automatized and only requires the exposure time and the measurement size as inputs.

2.2.2 Spectral data analysis

The Raman intensity of the scattered light I_i of a given component in the focal point is dependent on variables related to the spectrometer setup and the material physical properties. The intensity is calculated using equation (2.10), where the variables dependent on the material are depicted in red as it follows, the molar mass $\widetilde{M}_i$, the differential scattering plane $\frac{\partial \sigma_i}{\partial \Omega}$, which contains the information related to the spectral properties of the observed chemical species and the mass concentration c_i. The setup-dependent variables are marked in blue as it follows; the irradiation volume V_{irr}, the observation angle of the objective Ω_{obs}, the projection area of the detector opening on the irradiation volume F, the intensity of the exciting radiation I_0, and the efficiency of the detector system represented by R. The advantage while determining the concentration via Raman spectroscopy is the linear concentration dependency of the intensity.

$$I_i = \frac{\partial \sigma_i}{\partial \Omega} \frac{c_i}{\widetilde{M}_i} N_A V_{irr} \Omega_{obs} F^{-1} R I_o \qquad (\,2.10\,)$$

Schabel proposed dividing the intensity of a component i by another intensity of a different component j using the same spectrometer to cancel the setup variables, leaving only the species dependent as shown in equation (2.11).[42][42] By rearranging the terms, the mass of each component can be separated, and the other variables condensed into one major constant K_{ij} known as the system calibration constant. This expression leads to a simple relation between Raman intensity and mass loading X_i. Schabel utilized this expression to determine one dimensional measurements of polymer films while drying.[95]

$$\frac{I_i}{I_j} = \frac{\dfrac{\partial \sigma_i}{\partial \Omega} \dfrac{c_i}{\widetilde{M}_i}}{\dfrac{\partial \sigma_j}{\partial \Omega} \dfrac{c_j}{\widetilde{M}_j}} = K_{ij} \frac{m_i}{m_j} = K_{ij} X_i \qquad (\,2.11\,)$$

The determination of the concentration of a mixture via Raman intensity is done by weighting the intensity of each pure component in a sum as written in equation (2.12). The experimentally obtained intensity is compared with the calculated one in a squared error. Therefore, to determine

the weighting factors α_i, the squared error must be minimized. This methodology has been successfully applied in multiple works with the same spectrometer[47,51,54].

$$I_{mix} = \sum I_i \alpha_i$$

(2.12)

where $\sum \alpha_i = 1$

The pure component spectra were obtained as follows: The glass flakes were directly measured as a powder, whereas the PVA spectrum was obtained by casting an aqueous PVA solution on to a 140 µm thick glass substrate. The coated polymer solution was later dried in a drying channel coupled with a Raman spectrometer, until no changes in the Raman spectra along the film were seen. Afterwards, it was put in a heating chamber for 24 hours to allow any remaining water to leave the film. The resulting spectra are shown in Figure 2.5.
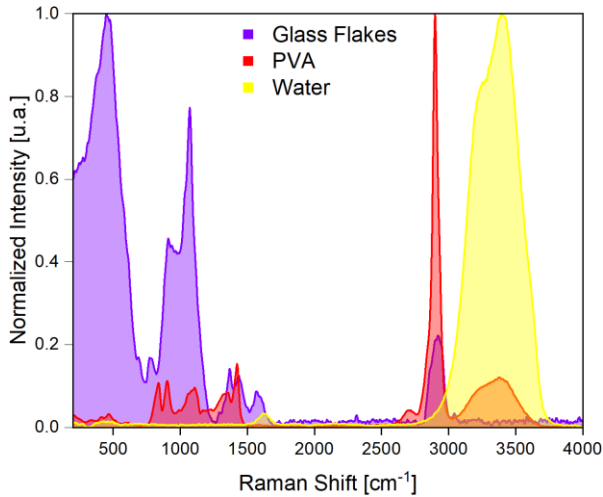
Figure 2.5. Comparison of the pure component Raman spectra of water, PVA and glass flakes, showing the characteristic peaks between 300 and $500\ cm^{-1}$ for the glass flakes, and between 2500 and $3800\ cm^{-1}$ for water and PVA.[69]

The characteristic peaks for glass (SiO_2) are located at wavenumbers between 300 and 500 cm^{-1}, at ~2750 cm^{-1} another peak from the residual glass impurities can be seen. For water, a wide band around 3450 cm^{-1} is

displayed. In the case of polyvinyl alcohol, the spectral information be-tween 300 to 1800 cm^{-1} is called the fingerprint area. Most of the peaks located in this interval come from the saturated bond (C-C) and the alkene bond (C=C) between two carbon atoms. The characteristic peak located at 2750 cm^{-1} corresponds to the hydrogen carbon bond. On the right side of this peak a band like the water band can be seen. It is expected that not all the water leaves the polymer film during the film casting and drying. This is because the air around the film has water, and the film unavoidably takes in water from the atmosphere. That is why the spectrum for the PVA is considered as dry, because the obtained spectrum contains the mini-mal amount of water that could be present under the chosen laboratory conditions.

The spectral evaluation was done at the interval where the characteristic peaks of glass and PVA are found. For the data analysis, a baseline cor-rection was carried out for the intensity array, and the intensity was nor-malized, as depicted in Figure 2.5.

For the calibration constant, different glass flakes-PVA films were pre-pared by drying at different conditions to induce different particle distribu-tions at different concentrations. Every film measurement had 400 data points at different coordinates inside the film and the weighting factors were determined accordingly. If the volume of the focal point remains con-stant, the average weighting factors $\bar{\alpha}_i$ could be correlated with the aver-age mass fraction $\bar{x}_i$ using equation (2.13)

$$\frac{\bar{\alpha}_i}{\bar{\alpha}_j} = K_{ij}\frac{\bar{x}_i}{\bar{x}_j} \qquad\qquad (\,2.13\,)$$

The volume of the focal point is not equal to the real volume due to optical deformation given by the change of the refractive index, which is a func-tion of the system's composition. The displacement of the focal point can be corrected using the center of gravity (c.o.g.) and the depth focus (d.o.f.) correction factors. The calibration procedure as well as the Raman spectra analysis and the deformation correction are done using existing software written in Microsoft's Excel Visual Basic. The resulting calibra-tion curve with the averaged weighting factors is displayed in Figure 2.6.
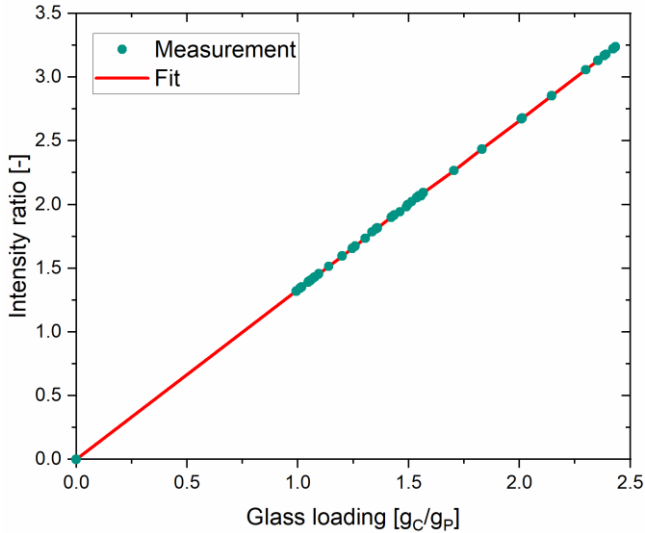
Figure 2.6. Calibration curve of the material system PVA and glass flakes. Calibration samples were prepared at different drying conditions to induce different particle distributions. The obtained calibration constant is ($K_{C,P} = 1.32$).[69]

2.3 Particle orientation investigation

The experimental determination of the orientation angle was conducted by coating a silicon wafer with dispersion. The particle concentration $\phi_C = 1\%$ is maintained low to facilitate the identification of single particles. The dispersion was cast using a coating knife (ZUA 2000.100, Zehntner) with a gap of $h_0 = 100$ µm at $\dot{\gamma} = 10 \ s^{-1}$. The resulting film was later frozen with liquid nitrogen and cut in half. Afterwards, the cross section was investigated with an electron microscope to determine how the particles are arranged.

In Figure 2.7, the cross section of a PVA film is displayed and the glass particles are marked in red to ease identification. As expected, during the freezing and cutting of the film some particles were caught in the middle and could not be separated from the film but remained hanging at the side, those defects are circled in blue to avoid confusion with particles that are not aligned. As can be observed, most of the particles remain at

a horizontal position after coating or slightly tipped on the side. The freezing and cross section analysis were realized with the help of a technician at the Laboratory of Electron Microscopy (LEM).
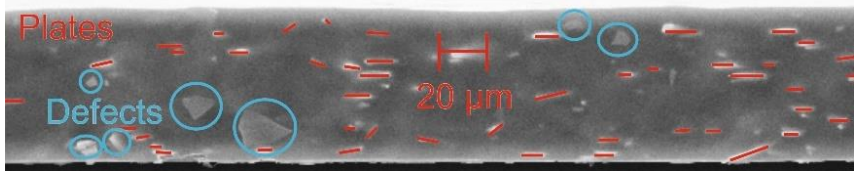
Figure 2.7. SEM image of a PVA film with 10 µm glass flakes ($r_p = 0.10$) embedded. The particles are marked in red showing how the particles are horizontally oriented.

The orientation of the particles after drying was investigated in the same manner to determine if the plates rotate after the coating process. A diluted dispersion of plate-like particles in a PVA solution ($\phi_C < 1\,\%$) was cast and dried. An area of $100\,\mu m\ \times\ 100\,\mu m$ was investigated to test if the resolution corresponds to the actual size and if the particles' orientation remains after drying. In Figure 2.8, the side area of a polymer film can be seen at two longitudes $x = 15\,\mu m$ and $x = 30\,\mu m$. After converting the Raman intensity to concentration, using the method described in the previous section, the calculated concentration array was arranged in a matrix, in which their index corresponds to the coordinates of the focal point. Afterwards, it was plotted using the MATLAB 2018 surface function. The colour gradient was adjusted by setting yellow when a pure glass flake ($\phi_C = 100\,\%$) was encountered and purple for pure PVA ($\phi_P = 100\,\%$). At $x = 15\,\mu m$ a horizontally oriented single glass flake can be seen with size that corresponds to the average particle size ($10\,\mu m$). Moreover, at $x = 30\,\mu m$ more flakes are shown with the same orientation distribution, experimentally validating that the plate-like particles are oriented horizontally after knife coating and drying.
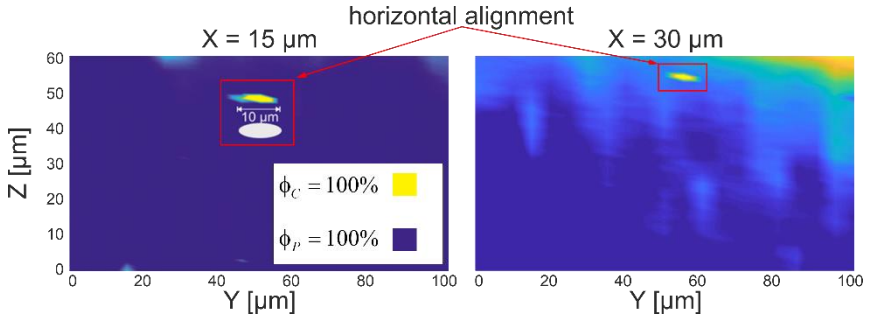
Figure 2.8. Cross sections of a dry film. PVA is marked with purple ($\phi_P = 100$ %) and the glass flakes with yellow ($\phi_C = 100$ %).[69]

The results are crucial to model the transport properties of the particles and predicting the particle distribution in dried films. In the following chapter it is shown that the simulations can reproduce the behavior, with most of the plate-like particles positioned in a horizontal position or are slightly tipped to one side after the knife coating process.

2.4 Sedimentation measurements

Sedimentation rates for colloidal particles in a dispersion can be determined by measuring the velocity of a settling front, as depicted in Figure 2.9. If all the particles in the liquid fall at the same rate, there is a change in the optical properties of the dispersion at the phase boundary. This means that the separation will cause the dispersion to become clearer at the top. However, experimental observation showed that during settling three different regions can be identified: a sediment region with a concentration close to close packing, a free-settling region where the particles maintain the initial volume fraction as it travels downwards, a transition region where the particle volume fraction changes smoothly between the first two. The size of the transition region has an order of magnitude that corresponds to the inverse of the Péclet number $O(Pe_C^{-1})$, meaning that at high Pe_C the transition turns into a discontinuity. Therefore, it is possible to measure the settling velocity by following the discontinuity along the sample's height.
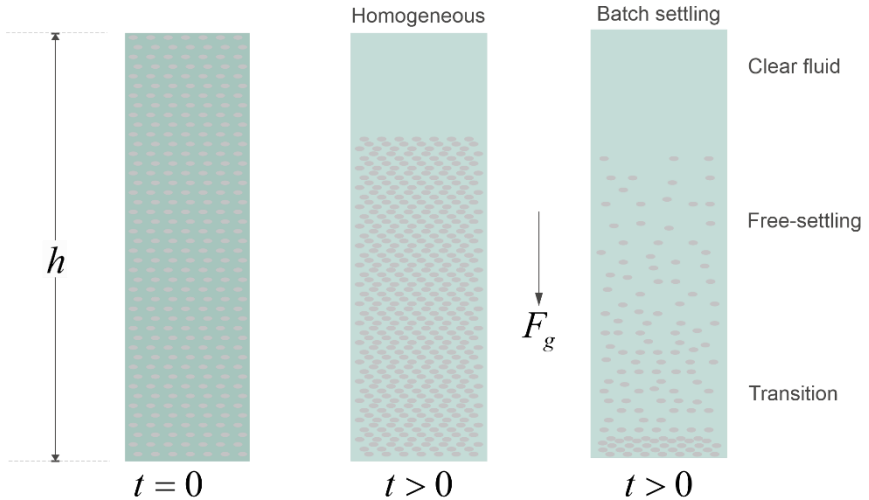
Figure 2.9. Graphical representation of homogeneous sedimentation and batch-settling of particles in a dispersion caused by gravity. Showing the separation of the components in an orderly manner with the presence of a sedimentation front and the sediment, transition, and free settling regions respectively.

To maintain the process as described, it is important that the interactions between particles remain minimal. Because collisions could cause the formation of agglomerates and increase deviation from Stokes' formula (see equation (3.1)). This can be avoided by maintaining a low particle concentration.

Waiting for a stable dispersion to separate by means of gravity can take a long time. For example, a 1 µm silicon colloidal particle in water at $20\ °C$ has a settling velocity of ~ 1 µm/s and would take about three hours to move $1\ cm$ downwards. Moreover, the experimental set-up must be isolated and damped to avoid the influence of external forces. Therefore, the approach chosen for investigating the sedimentation behavior of particles is by imposing a homogeneous external force that causes the separation of the particles from the liquid.

To this end, an analytic centrifuge (LUMi Sizer centrifuge, LUM GmbH) which allows the measurement of light transmission in a liquid is used to monitor the settling of the plate-like particles. This experimental investigation was conducted at the Institute of Mechanical Process Engineering

and Mechanics (MVM) supervised by Prof. Nirschl. In Figure 2.10, a graphical representation of the measurement principle is depicted. During sedimentation, a clear part in the dispersion appears, changing abruptly the value of the light transmission. This change moves from left to right as time passes, until all the particles reach the bottom. By measuring the displacement of this step, it is possible to calculate the sedimentation front velocity.
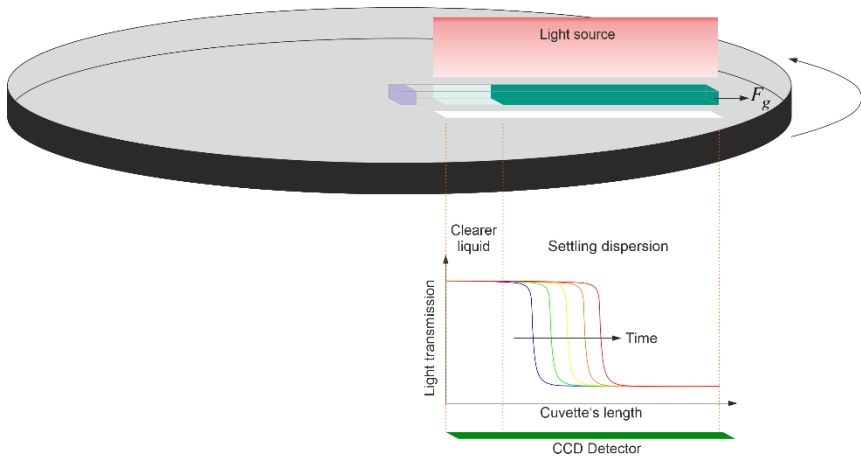
Figure 2.10. Graphical representation of the centrifuge measurement principle of the LUMi Sizer at MVM. On the top, a sample is being centrifuged while a light source irradiates it. Underneath the sample is a detector which measures the change of the light transmission as the particles settle to the bottom of the flask.

Aqueous PVA dispersions were prepared at a constant concentration of $\phi_P = 3$ % and different particle concentrations ranging from $\phi_C = 1$ % to 6 % at $40\ °C$. The centrifuge was operated at $200\ rpm$, which corresponds to a sedimentation force equivalent to ~12 times the acceleration of gravity. All the used samples were completely transparent with a sediment at the bottom after 2 hours. The sedimentation rates were measured in triplicate to assure reproducibility. In Figure 2.11, an example of the light transmission measurement is plotted. There is no formation of a noticeable discontinuity or step. Instead, a slope gets flatter as time passes. Nevertheless, it is still possible to determine the sedimentation rate of the plates by following the change of the slope.
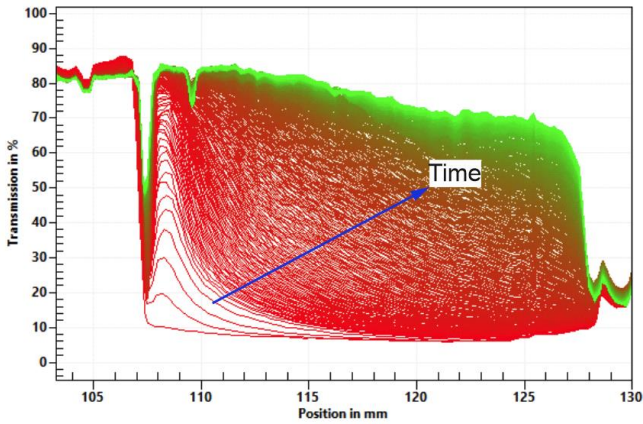
Figure 2.11. Light transmission measurement of a $3\,\%\,v/v$ PVA and $5.21\,\%\,v/v$ glass flakes aqueous dispersion at $40\,°C$. Showing for this case that instead of a step a slope is getting flatter as the time passes. This image is copied directly from the LUMi Sizer centrifuge analysing software at MVM.

In Figure 2.12, the left vertical axis shows the logarithmic sedimentation velocity distribution calculated from the light transmission rates in Figure 2.11, showing a gaussian distribution with a small standard deviation. On the right vertical axis, the cumulative distribution is plotted, where the mean value corresponds to the cumulative distribution at $50\,\%$ or $Q^{50}(U_C) = 28\,\mu m/s$. The mean value of the sedimentation velocity is used to study the concentration dependence of U_C. The complete values of sedimentation at different plate concentrations and at different cumulative distributions can be found in the appendix of this work in section 7.4.
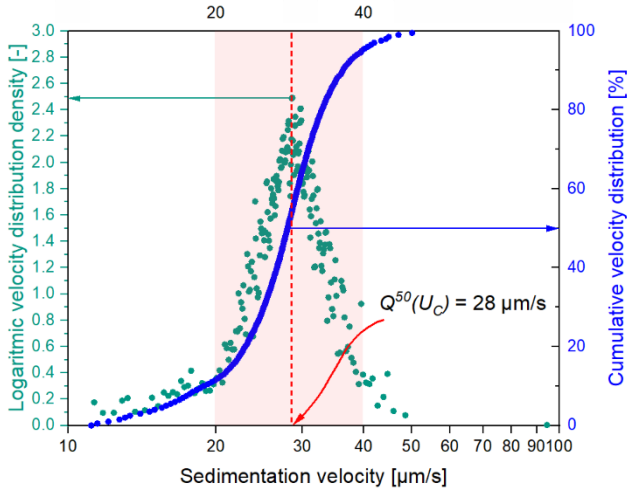
Figure 2.12. Cumulative velocity distribution (right y-axis) and logarithmic velocity distribution density (left y-axis) as a function of the sedimentation velocity of a 3 % v/v PVA and 5.21 % v/v glass flakes aqueous dispersion at 12 times the acceleration of gravity (12g), a temperature of 40 °C and $r_p = 0.10$. Showing a maximum corresponding to the cumulative distribution at 50% $Q^{50}(U_C) = 28$ µm/s, at 1g the velocity corresponds to $Q^{50}(U_C) = 2.3$ µm/s. 80% of the measured velocity falls between 20 µm/s and 40 µm/s. The sedimentation rates are calculated from the light transmission rates in Figure 2.11.

In Figure 2.13, the experimentally obtained sedimentation rates of two dispersions at different aspect ratios, $r_p = 0.10$ and $r_p = 0.03$, are displayed. Both experiments were fitted utilizing the expression shown in equation (2.14).

$$U_C = U_{C,0}(1 - \phi_c)^{-n} \qquad (2.14)$$

The particles at $r_p = 0.03$ appear to move faster even though their bigger surface generates a greater drag than the particles at $r_p = 0.10$. The difference resides in the particle weight which is dominant in the overall sedimentation velocity. At $r_p = 0.03$ the particles have an equivalent particle diameter of $d_c = 10$ µm whereas at $r_p = 0.10$ it is just $d_c = 2.20$ µm. The parameters to fit are the sedimentation velocity at infinite dilution $U_{C,0}$ and the exponent n. It can be noted that both aspect ratios show a good agreement with the model. The identity of the exponent as well as its

41

dependency with the aspect ratio will be discussed in the following chapter in section 3.1. In this kind of experiments the influence of the polymer was not investigated.
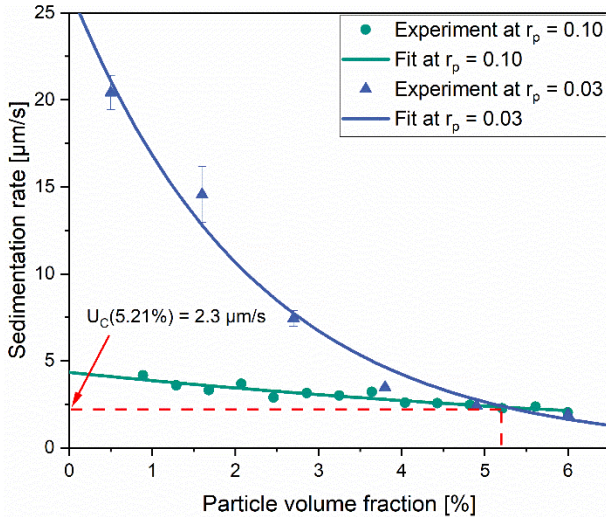
Figure 2.13. Sedimentation rate of plate-like particles at the acceleration of gravity ($1g$) in a $3\,\% \, v/v$ PVA aqueous solution system at 40°C as a function of the plates' concentration. The value from Figure 2.12 is marked in the diagram at $1g$. The used particles had an aspect ratio of $r_p = 0.10$ (circles) and $r_p = 0.03$ (triangles). Both experiments are fitted using the modified Batchelor model in equation (2.14), showing a good agreement.

2.5   Drying experiments

Aqueous PVA solutions with an initial particle concentration of $\phi_{C,0} = 2\,\%$ were prepared. Thin films were produced by casting the coating dispersion onto thin glass substrates using a coating blade (ZUA 200.100, Zehntner) at different gaps, resulting in wet film heights h_0 between 100 and $800\,\mu m$. Afterwards, the samples were dried using the devices described in the following subchapters. It is important to mention that the calculation of the evaporation rate $\dot{E}_0$ at the beginning of the drying process is necessary to determine the location of the experiment in the drying regime map.

2.5.1 Drying channel

The drying channel used in this work was built and developed by Schabel et al.[42,95] The set-up is temperature-controlled, allowing isothermal drying experiments. The air supply can also be temperature-controlled and has a dew point of $-60\,°C$. It is coupled with the Raman spectrometer previously described to measure the amount of solvent remaining in a film during drying at different film heights with a spatial resolution of $2 - 3\,\mu m$.

Due to the layout of the tunnel, drying occurs differently depending on the location of the wet film being studied. In other words, drying is dependent on the lateral coordinate parallel to the air flow. The side of the film that first comes in to contact with the air flow will dry faster than other parts of the film. Once the edge has dried, the mass transfer concentration boundary layer will move in the direction of the air flow increasing the drying rate on the rest of the film, as described by Schmidt-Hansberg et al. Scharfer, Schabel.[96] To accurately calculate the initial drying rate at a given point in the wet film, the determination of a local mass transfer coefficient is needed. Ameel[97] developed a correlation for the local Sherwood number Sh_x for the overflow of a flat plate as a function of the Schmidt Sc and Reynolds Re_x numbers, the position being investigated x and an offset x_0, as depicted in equation (2.15). As the drying front advances, this offset migrates into the film.

$$Sh_x = \frac{0.332 \cdot Sc^{1/3} Re_x^{1/2}}{\left[1 - \left(\frac{x_0}{x}\right)^{\frac{3}{4}}\right]^{1/3}}$$

(2.15)

where,

$$Sc = \frac{\nu}{\delta_{S,air}} ; Re_x = \frac{ux}{\nu}$$

$$\beta_{S,gas}^x = \frac{\delta_{S,air} Sh_x}{x}$$

(2.16)

The value of x is given by the location to be analyzed by means of in situ Raman spectroscopy. For the drying of an $3\,\%\,v/v$ aqueous PVA wet film using an air velocity of $u = 1\,m/s$ at $40\,°C$ and at $x = 56\,mm$ with no offset

will result in an initial mass transfer coefficient of $\beta_{S,gas,0}^{x=56\,mm} = 0.008\,m/s$ with a corresponding local heat transfer coefficient of $\alpha_{x=56\,mm} = 8.2\,W\,m^{-2}K^{-1}$. If the analysis is done at any other point, the migration of the moving boundary layer needs to be considered [96].

2.5.2   Comb Nozzle Dryer

The Comb Nozzle ® dryer is a lab scale device developed to generate homogeneous drying at high evaporation rates, thus being able to recreate industrial conditions[98]. It consists of impinging jets with a hexagonal geometry, hence the name. The air supply is preheated and then transported to the nozzles using an industrial blower, while neighboring jets remove the humid air. This configuration results in a more uniform heat transfer coefficient (HTC) distribution. For example, a mean HTC of $\alpha = 40\,W\,m^{-2}K^{-1}$ has a deviation of 5 %.

Moreover, the range of the HTC depends on the distance between the sample and the nozzles as well as the volumetric air flow. The operating range of the dryer utilized in this work was $20 - 80\,W\,m^{-2}K^{-1}$, and the HTC is varied by only adjusting the volumetric flow of the air. The mass transfer coefficient is calculated by using the Lewis number and Lewis analogy, shown in equations (2.17) and (2.18) respectively. The Lewis number compares the thermal diffusion of the gas phase, given by the heat conductivity λ_{gas} divided by the molar density $\tilde{\rho}_{gas}$ and molar heat capacity $\tilde{c}_p$, with the mass diffusion of the solvent in the air $\delta_{S,air}$.

$$Le = \frac{\lambda_{gas}}{\tilde{\rho}_{gas}\tilde{c}_{p,gas}\delta_{S,air}} \qquad (\,2.17\,)$$

$$\beta_{S,gas} = \frac{\alpha}{\tilde{\rho}_{gas}\tilde{c}_p Le^{1-n}}$$

where,   (2.18)

$n = 0.33$ if the air flow is laminar

$n = 0.42$ if the air flow is turbulent

Most of the physical properties in equation (2.18) are considered to be those from air, due to the low amount of water present in the gas mixture. For the drying of a $3\ \%\ v/v$ aqueous PVA wet film using an HTC of $\alpha = 30\ W\ m^{-2}K^{-1}$ at $40\ °C$ and relative humidity of $rH = 30\ \%$ will result in an initial mass transfer coefficient of $\beta_{S,gas,0} = 0.03\ m/s$.

3 Simulation model

In the following chapter, the considerations made to describe the mass transfer during drying of the water–polyvinyl alcohol–silicon oxide particle system are found. As mentioned in the previous chapter, non-spherical particles are subject to changes in the orientation when an external force is applied. This leads to changes in transport properties, such as dispersion viscosity, sedimentation rate and diffusion when comparing to spheres. Furthermore, these properties describe anisotropic systems, which are direction dependent.

Using the state-of-the-art quasi-binary approach as a framework for the simulation, some assumptions are made during the different stages of composite production to simplify the anisotropic behavior of plate-like particles. Most of the simplifications are made to circumvent the use of a diffusion tensor and keep the problem one-dimensional. As shown in the next chapter, these approximations correspond to the experimental observations.

The particle orientation is described by identifying the forces that apply and allowing its rotation while coating and drying is simulated. Once the orientation is determined, changes to the conservation equation are made. A parameter sweep determines how particle shape, in combination with the drying conditions affect the particle distribution in the dry film. Finally, using the particle distribution and maximal packing concentration as criteria, new drying regime maps for plate-like particles as a function of sphericity and the drying conditions are drawn.

3.1 Diffusion and sedimentation of plate-like particles

The movement of a single colloidal particle caused by a gradient in either the chemical potential or gravity can be described by the approach of Stokes and Einstein in equation (3.1). It is a function of the temperature T , Boltzmann constant κ and the friction caused by the liquid represented by the drag coefficient ξ, which is obtained by balancing the forces acting onto the particle, namely gravity, buoyancy, and viscous forces[37].

$$D_{C,0} = \frac{\kappa T}{\xi}$$

$$U_{C,0} = \frac{(\rho_C - \rho_S)gV_C}{\xi}$$

$(\,3.1\,)$

In Figure 3.1, a spherical and a horizontally oriented plate-like particle are displayed descending in a fluid, at settling rate of $U_{C,0}^i$ showing the change in the liquid velocity $\bar{u}$ around them using normalized streamlines. In the case of spherical particles, the drag is dependent on the fluid's viscosity and the particle size, leading to a drag coefficient $\xi = 6\pi\eta_S R_C$. For the plate-like particle, the interaction with the fluid, changes the friction, and therefore, the drag coefficient.
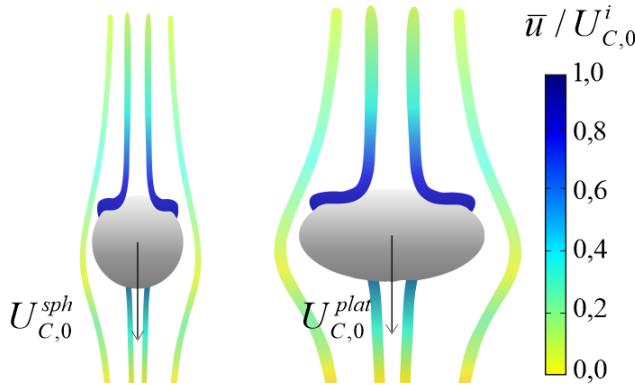
Figure 3.1. Schematic of the fluid velocity $\bar{u}$ around a sphere and a plate-like particle at settling velocity $U_{C,0}$ showing the effects of the geometry via the normalized streamlines.

For ellipsoids, Perrin developed a set of equations for the drag coefficient which are additionally dependent on the aspect ratio and particle orientation[99]. He only considered the trivial cases, in which either the particle has its major axis on a horizontal or vertical position. Analogous to the Stokes-Einstein equation, the drag coefficient is dependent on the medium viscosity and the particle size, given by the relative size of the semiaxes S_i using the lengths of the major b and the minor a axes (see Figure 1.6).

47

Perpendicular $\qquad \xi_\perp = 16 \cdot \pi \cdot \eta_j \dfrac{a^2 - b^2}{(2 \cdot a^2 - b^2) \cdot S_i - 2 \cdot a}$ $\qquad$ (3.2)

Parallel $\qquad \xi_\parallel = 32 \cdot \pi \cdot \eta_j \dfrac{a^2 - b^2}{(2 \cdot a^2 - 3 \cdot b^2) \cdot S_i + 2 \cdot a}$ $\qquad$ (3.3)

where,

$i = oblate \qquad S_{obl} = \dfrac{2}{\sqrt{b^2 - a^2}} \arctan\left(\dfrac{\sqrt{b^2 - a^2}}{a}\right)$ $\qquad$ (3.4)

$i = prolate \qquad S_{pr} = \dfrac{2}{\sqrt{a^2 - b^2}} \ln\left(\dfrac{a + \sqrt{a^2 + b^2}}{b}\right)$ $\qquad$ (3.5)

In Figure 3.2, the values for the drag and the diffusion coefficient of a single particle are plotted as a function of the aspect ratio. Even though the values for spherical particles cannot be calculated using the Perrin's set of equations, it can be observed that the values of both horizontal and vertical coefficients converge at the same point when the aspect ratio approaches one ($a = b$). Moreover, the drag coefficient tends to diverge when the geometry is either infinitely flat $r_p \to 0$ or infinitely long $r_p \to \infty$. Reciprocally, the diffusion coefficient drops at these aspect ratio values no matter the orientation of the particle. However, there is a maximum for rod-like particles when they are vertically oriented and for plate-like particles when they are horizontally oriented, both near complete sphericity, when the particle geometry is hydrodynamically optimal.
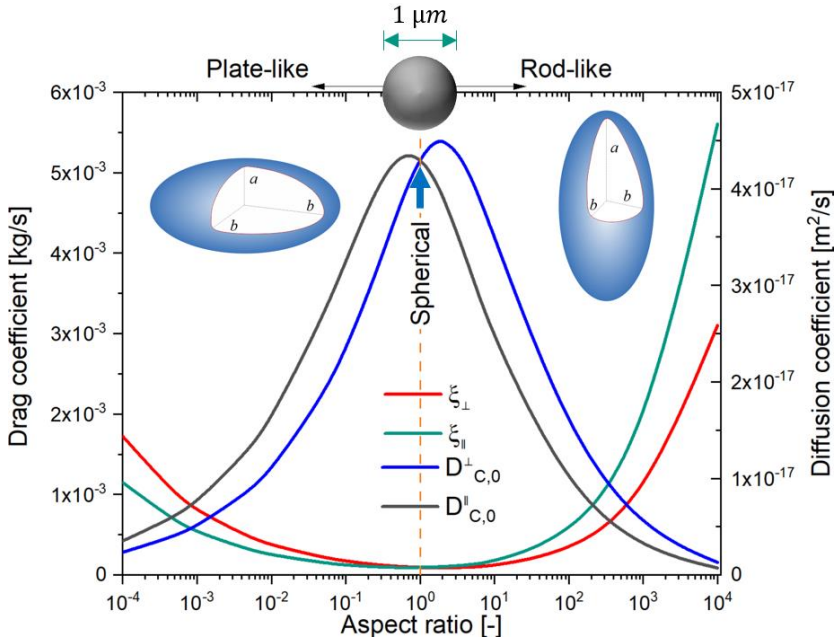
Figure 3.2. Drag and particle diffusion coefficient plotted as a function of the aspect ratio in a 3 % v/v aqueous PVA solution, considering the volume of a sphere with a 1 μm diameter. Both the horizontal and vertical cases are plotted for the diffusion and drag coefficient.[69]

If a single oblate ellipsoid is oriented in the horizontal position, as depicted in Figure 3.1, the diffusion coefficient and sedimentation rate can be calculated using expressions (3.1), (3.2) and (3.4). If there are different orientations, a more detailed modelling needs to take place to calculate the properties of the whole dispersion; meaning a diffusion tensor must be considered, as follows:

$$\overline{\overline{D}}_{C,0} = \kappa T \begin{pmatrix} 1/\xi_{11} & 1/\xi_{12} & 1/\xi_{13} \\ 1/\xi_{21} & 1/\xi_{22} & 1/\xi_{23} \\ 1/\xi_{31} & 1/\xi_{32} & 1/\xi_{33} \end{pmatrix} \qquad (3.6)$$

This tensor can be simplified if said particle can either remain horizontal or vertical, thus leaving only the matrix[100]:

49

$$\overline{\overline{D}}_{C,0} = \kappa T \begin{pmatrix} 1/\xi_\parallel & 0 & 0 \\ 0 & 1/\xi_\parallel & 0 \\ 0 & 0 & 1/\xi_\perp \end{pmatrix} \qquad (3.7)$$

In the literature, some considerations are made to maintain a scalar diffusion coefficient by only considering the two trivial orientations and weighing them in an effective drag coefficient ξ_{eff} shown in equation (3.9). This expression describes the mobility of a horizontally oriented particulate system. The symmetry of the particle makes the movement in the horizontal plane equal, hence the two in the expression 3.8 [101].

$$\xi_{eff} = \frac{3}{\dfrac{1}{\xi_\perp} + \dfrac{2}{\xi_\parallel}} \qquad (3.9)$$

3.2   Rotation of axisymmetric particles

The simulation model used in this work accurately describes particle orientation during coating and drying. This subchapter studies step by step the possible influences that trigger the rotation of particles to understand the experimental observations obtained in section 2.3. After the formulation step, particles find themselves in a diluted regime ($\phi_C = 2\ \%$), meaning that the angle of orientation is given by Brownian motion[102–105]. Therefore, particle orientation is random. The angle of orientation during coating is dependent on the fluid dynamics, which requires a more detailed analysis.

A knife coating process resembles the case of simple sheer at a constant rate $\dot{\gamma}$, assuming a fully developed flow ($t \gg 0$) as depicted in Figure 3.3. A particle is in a fluid with a polar angle φ and azimuthal angle θ relative to a unitary vector $\bar{d}$ perpendicular to the particle's surface. The fluid velocity vector $\bar{u}$ has zeros in any direction except in the x direction and is given by equation (3.10).

$$u_x = \dot{\gamma} \cdot z \qquad (3.10)$$
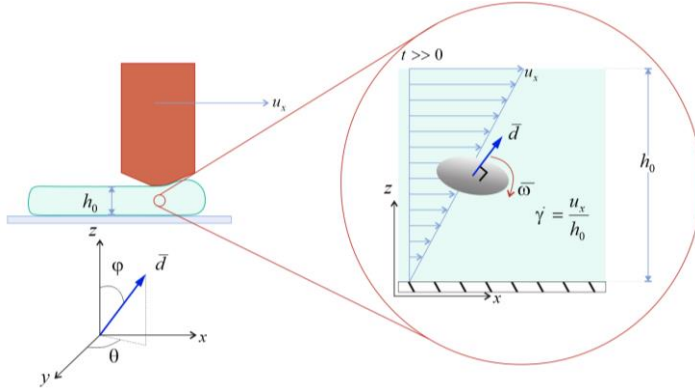
Figure 3.3. Graphical representation of a coating process using a coating knife, showing a fully developed linear velocity profile and the rotation of a particle.

The rotational speed of the particle, represented by the orientation of vector $\bar{d}$ is obtained by the cross product of the rate of rotation vector $\bar{\omega}$ and the fluid velocity vector $\bar{u}$.

$$\frac{d}{dt}\bar{d} = \bar{\omega} \times \bar{u} \qquad (3.11)$$

Expanding this expression using the strain tensor $\bar{\bar{E}}$ and the vector $\bar{\Omega}$ results in equation (3.12), where B is the Bretherton constant which acknowledges the particle shape as an expression of the aspect ratio r_p[106,107].

$$\frac{d}{dt}\bar{d} = \bar{\Omega} \times \bar{d} + B \cdot \left[\bar{\bar{E}} \cdot \bar{d}(\bar{d} \cdot \bar{d}) - (\bar{\bar{E}} : \bar{d}\bar{d}) \cdot \bar{d}\right]$$

$$B = \left(\frac{r_p^2 - 1}{r_p^2 + 1}\right) \qquad (3.12)$$

The vector $\bar{\Omega}$ corresponds to the bottom half of the rotation tensor $\bar{\bar{R}}$, whereas $\bar{\bar{E}}$ is the strain rate tensor. For simple shear the tensors are written as follows:

51

$$\bar{\bar{R}} = \frac{\dot{\gamma}}{2}\begin{pmatrix} 0 & 1 & 0 \\ -1 & 0 & 0 \\ 0 & 0 & 0 \end{pmatrix} = -\varepsilon_{ijk}\Omega_k$$

$$\bar{\bar{E}} = \frac{\dot{\gamma}}{2}\begin{pmatrix} 0 & 1 & 0 \\ 1 & 0 & 0 \\ 0 & 0 & 0 \end{pmatrix}$$

(3.13)

Parametrizing $\bar{d}$ using spherical coordinates results in:

$$d_x = \sin\theta \cdot \cos\varphi$$

$$d_y = \sin\theta \cdot \sin\varphi$$

$$d_z = \cos\theta$$

(3.14)

Substituting equations (3.13) and (3.14) in (3.12), two sets of equations are obtained for the angles θ and φ:

$$\frac{d\theta}{dt} = -\left(\frac{r_p^2 - 1}{r_p^2 + 1}\right) \cdot \frac{\dot{\gamma}}{4} \cdot \sin 2\theta \cdot \sin 2\varphi$$

(3.15)

$$\frac{d\varphi}{dt} = -\frac{\dot{\gamma}}{r_p^2 + 1} \cdot \left(r_p^2 \cdot \cos^2\theta + \sin^2\varphi\right)$$

(3.16)

Figure 3.4 depicts the solution for the polar angle φ at a shear rate $\dot{\gamma} = 80\ s^{-1}$, an aspect ratio of $r_p = 0.10$ and with an initial value of $\varphi_0 = 45°$. As expected, the solution is periodic, showing that the particle will turn over fast and stay most of the time in a horizontal position or at a low angle[108]. Hence the probability for a particle to be in a vertical position during coating is low. The works from Jefferey[109] come to the same conclusion. In the literature this phenomenon is widely known as flake alignment and has been extensively investigated.[110–112] Nevertheless, it is important to mention that this phenomenon is only seen for oblate particles ($r_p < 1$), for rod-like particles, the orientation at simple shear oscillates without any trend.[113]
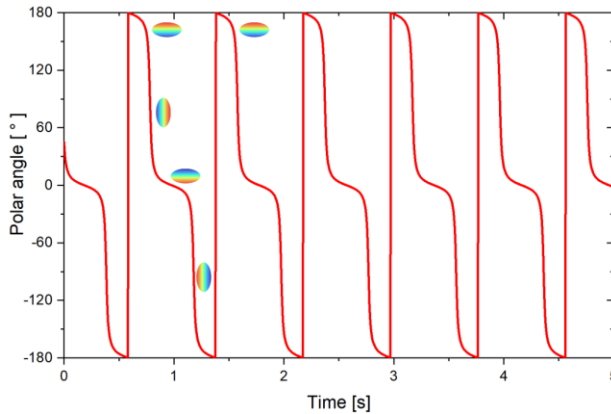
Figure 3.4. Polar angle course at a shear rate of 1 s^{-1} and an aspect ratio of $r_p = 0.10$. A particle is shown demonstrating the orientation, confirming that for most of the coating time the particle maintains a horizontal position.

After the coating process, there is no longer a velocity gradient in the film and therefore no mechanical causes for rotation. Due to Brownian motion it is possible for the particles to rotate. During drying, only the film shrinkage and the sedimentation of the particles due to gravity, the flow of the liquid around the particle could cause a change in the particles' orientation. Kirchner conducted a study using particulate spray coatings with initial random orientation to verify if the shrinkage of the film has an influence on the rotation of the particles[114]. It was widely acknowledged that particles in spray coatings orient themselves, due to the moving boundary pushing the particles downwards, and not due to a flow-induced orientation[115]. Kirchner showed that only a quarter of the particles present in the coating were aligned due to solvent evaporation, concluding that the drying has an influence on the particles' alignment, but it is not dominant.

Sedimentation has a different effect on the particle rotation. Whalley and Mullins[116] theorized and later experimentally validated that plate-like particles could sediment in both an orderly and random manner, but at high force fields the plates tend to sediment horizontally. Ardekani et al.[117] developed simulations to understand what happens at low force fields. They determined that plates with an initial random orientation will wobble at the beginning of the process, but later stabilize their movement to remain in a horizontal position. This is not the case for rod-like particles,

53

which are subject to constant rotation, generating turbulence while descending[118–120]. The mathematical model in combination with the works found in the literature, justifies the modeling of the diffusion $D_C(\phi_C)$ and sedimentation $U_C(\phi_C)$ coefficient as scalars rather than a second-order tensor.

According to analytical work and the experimental observations on the orientation of plates shown in section 2.3, the particles will undergo three changes during processing as follows:

1. During formulation and before coating, the particles are suspended in the liquid and their angle of orientation is determined by Brownian motion, meaning that the angle distribution will be random.
2. After the dispersion has been cast onto the substrate via knife coating, the plates orient themselves in a horizontal position. The rate at which they align and sync is a function of the shear rate $\dot{\gamma}$.
3. During drying, the moving phase boundary aligns the particles that might still be randomly oriented. The other particles at other points in the film and those that did not align will orient themselves or remain horizontally. This is due to the downward movement which produces high viscous forces.

3.3   Aspect ratio influence on sedimentation

The concentration dependency of diffusion and sedimentation can be modelled, analogously to the relative viscosity, as a ratio of the dispersion transport property divided by the same property at infinite dilution $U_C/U_{C,0}$. In the case of the sedimentation rate and diffusion coefficient this ratio is known as the sedimentation coefficient $K(\phi_C)$. The most known model in the literature to describe concentration dependencies of transport properties for dispersions is due to Batchelor's model[121]. This work considers two non-electrically charged particles that interact in a diluted system. The Batchelor expression corresponds to series solution, which is given in equation (3.17) and is often approximated to the first term. A modified version is given by equation (3.18) and is in better concordance with experimental values at higher concentrations[122]. It must be noted that at low concentrations equation (3.18) reduces to expression 3.16.

$$\frac{U_C}{U_{C,0}} = 1 + K_2 \phi_C + O(\phi_C^2) \qquad\qquad (3.17)$$

$$\frac{U_C}{U_{C,0}} = K(\phi_C) = (1 - \phi_C)^{-K_2} \qquad\qquad (3.18)$$

The parameter K_2 is determined experimentally, for spherical particles that are randomly distributed the value ranges from $-K_2 = 4.2 - 6.4$ according to the literature.[123–125] For both spherical and plate-like particles there is a linear analytic expression developed by He et al.[126] $-K_2 \approx 3.8/r_p$. In Figure 3.5, several measurements of K_2 from the literature are plotted as a function of the particle aspect ratio r_p, showing that the He model does not represent the experimental data. Due to these discrepancies an empirical model based on the potential of two particles from Weeks et al.[127] is modified in this work as follows:

$$-K_2(r_p) = A + B \left[\frac{1}{(r_p + C)^4} - \frac{1}{(r_p + C)^2} \right] \qquad (3.19)$$

$$A = 6.18 \; ; \; B = 1.78 \cdot 10^{-3}; \; C = 5.22 \cdot 10^{-2}$$

The constants A, B and C of expression (3.19) are fitted by minimizing the sum of the squared differences. In this formula A corresponds to the minimal value of $-K_2$ given by the average measurements for spheres, C gives a threshold value for the aspect ratio at which $-K_2$ increases dramatically, and B is the rate at which $-K_2$ increases after the threshold. This approach shows a remarkable improvement for the prediction of experimental values. The results at $r_p = 0.10$ and $r_p = 0.08$ seem to break the trend, but those values are very close to each other and due to the different measuring techniques used to determine K_2, it should be interpreted as a small deviation from different literature sources rather than a break of the trend.
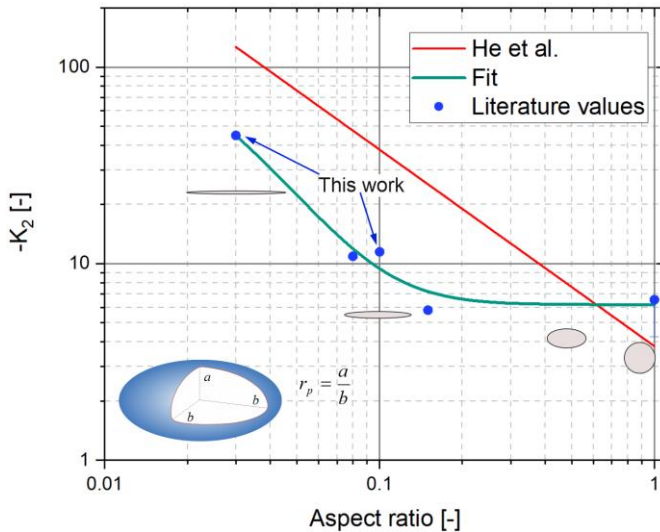
Figure 3.5. Particle shape influence on -K_2. The literature values from van der Kooij et al. [101] and Buscall et al. [123] are plotted in blue as well as the data produced in this work, showing the decrease in particle mobility at an increasing flat geometry. The theoretical model of He et al.[126] is plotted in red showing a considerable deviation from the experimental values, whereas the fit from equation (3.19) shows a good prediction in comparison.[128]

In Figure 3.6, the calculated normalized sedimentation velocity ($U_C/U_{C,0}$) as well as experimental values are plotted as a function of the concentration and the aspect ratio by utilizing equations (3.18) and (3.19). The model predicts the experimental data found in the literature and obtained in the present work, even though each experiment had a different liquid. This confirms that the influence of the viscosity of the medium is not relevant for K_2. Due to the good agreement, the simulation model utilizes the developed expressions for K_2 instead of the experimental values to calculate the sedimentation and diffusion coefficient of the particles during drying.
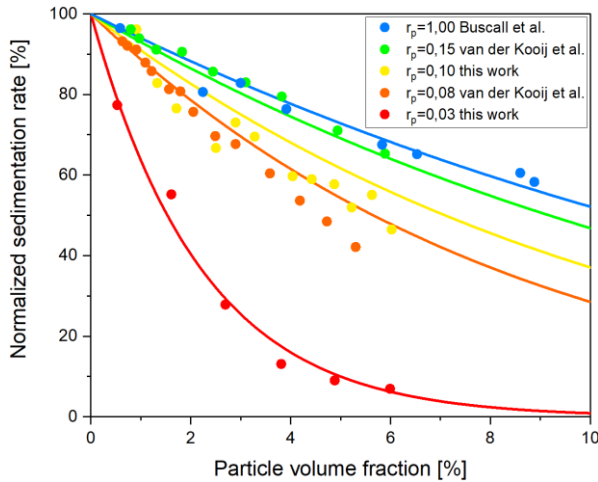
Figure 3.6. Normalized sedimentation velocity measurements plotted as a function of the concentration at different aspect ratios using equation (3.18) and (3.19), showing a good agreement with the experimental values from the literature and this work.

3.4   Adaptation of the existing simulation model

The simulation approach uses the model derived from the framework of Baesch et al. [67], changing the parameters that describe the sedimentation and diffusion of the particles. Using the knowledge obtained in the previous section, the model was adapted accordingly. Namely the diffusion coefficients of the particles and polymer, as well as the sedimentation were changed to match the material system. A complete derivation and non-dimensionalization of the model can be found in the appendix.

The model consists of three coupled partial differential equations (PDE), in the form of the dynamic diffusion equation with different volume fluxes $\Gamma_{i/S}$ and a moving boundary[129] as portrayed in Figure 3.7. The boundary conditions are defined at the top with evaporation of the solvent and at the bottom as impermeable[130]. The model only requires the temperature and the Péclet and sedimentation numbers to calculate the concentration profiles (see section 7.1). The PDE system is solved using the commercially available software COMSOL Multiphysics 5.5 and the application

Builder with the partial differential equation general form package and a moving mesh.
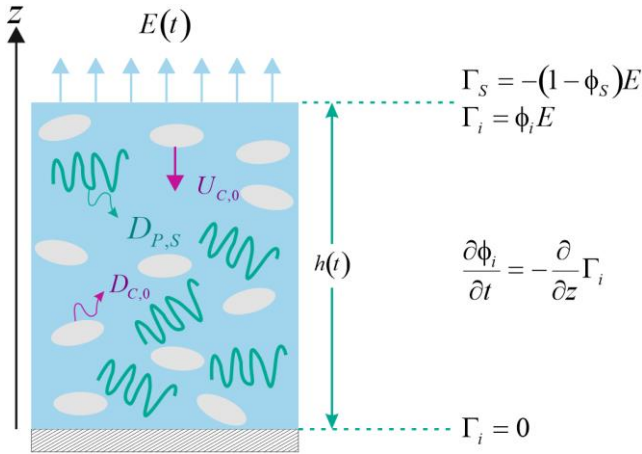
Figure 3.7. Graphical representation of the drying of polymer-particle-composites. At the top of the film the solvent evaporates; the particles in the bulk sediment and diffuse, the polymer also diffuses along the film and at the bottom of the film the substrate is impermeable[128]. The derivation of each flux can be found in the appendix 7.1.

In Figure 3.8, the volume fraction profiles are plotted at different dimensionless times $\tau = tE_0/h_0$ during drying and at different values of Pe_C and N_S, exhibiting the sensitivity of these parameters. Each column has the concentration of a given component; the particles are plotted on the left, the solvent in the middle and the polymer on the right, whereas the rows contain different drying conditions given by the non-dimensional entities. The initial volume fractions in all the plots are $\phi_{S,0} = 95\,\%$, $\phi_{P,0} = 3\,\%$ and $\phi_{C,0} = 2\,\%$, with the particles' aspect ratio at $r_p = 0.10$. This component distribution corresponds to a concentration in the dry film of $\phi_{P,dry} = 60\,\%$ and $\phi_{C,dry} = 40\,\%$, the first row of plots shows the concentration profiles at $N_S = 1$ and $Pe_C = 10$. It shows that the particles accumulate at the top of the film displaying a notable gradient, due to the fast evaporation of the solvent and slow particle diffusion. However, the polymer does not exhibit the same extreme gradient until $\tau = 0.7$, due to its high diffusion

coefficients which translates into a low Pe_P, counterbalancing the high evaporation of the solvent.

The middle row shows the concentration profiles when all the driving forces are balance, namely $N_S = Pe_C = 1$. During drying, most of the concentration profiles remain constant without visible gradients until $\tau = 0.70$. At this point, evaporation and sedimentation processese are not dominant; the particle diffusion velocity does not allow an accumulation at the top nor the bottom of the film. The increasing viscosity of the PVA-solution is the main reason why the particles accumulate at the top of the film, and a concentration gradient can be seen in the last time step.

The bottom row has the same values of dimensionless entities, expressly $N_S = Pe_C = 10$, but in this case the particles sink to the bottom of the film at $\tau = 0.10$. Although the drying driving force is high, the sedimentation velocity overcomes the evaporation rate and diffusion of the particles, thus not allowing the movement of the particles upwards. It must be noted that the simulation cannot run properly using some combinations of Pe_C and N_S[67]. If it were to obtain an accumulation of polymer (skin formation) and particles at the top of the film, high Pe_C and low N_S numbers should be given to acquire such a regime. Unfortunately, in those cases the simulation program does not converge, due to the high diffusion velocity of the polymer in contrast to the particles $D_{P,S} \gg D_C$.

As in previous work[73], three different particle concentration profiles were observed: accumulation of the particles at the top when the Péclet number is high and the sedimentation number is low, mostly constant component distribution along the film's height when Pe_C and N_S are low and at the same order of magnitude, and accumulation of the particles at the bottom when both nondimensional entities are at high values. From these results it is concluded that to trigger accumulation on the top or the bottom only a difference of one order of magnitude between the nondimensional numbers is required. In the next section, this threshold for the Péclet and sedimentation numbers is obtained to establish the boarders in the drying chart between the observed particle distribution regimes, thus allowing us to draw new drying regime maps for plate-like particles as a function of the aspect ratio.
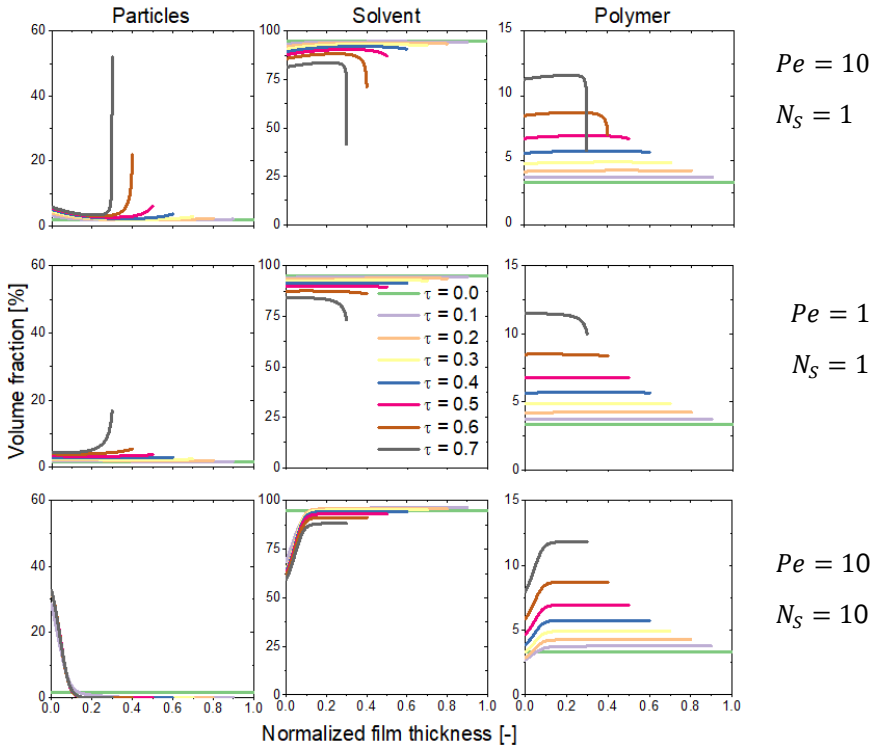
Figure 3.8. Volume fraction profiles as a function of the normalized film height at different dimensionless times, the left, middle and right columns correspond to the concentration profiles of particles, solvent, and polymer, respectively. Calculations were done with an aspect ratio of $r_p = 0.10$. The first row corresponds to a $Pe_C = 10$ and $N_S = 1$ and an accumulation of the particles at the film surface can be observed. The row in the middle was calculated with $Pe_C = 1$ and $N_S = 1$. Even at lower Pe numbers a particle accumulation at the surface is obtained due to an increase of the viscosity. The row at the bottom corresponds to $Pe_C = 10$ and $N_S = 10$. At this high sedimentation numbers an accumulation at the bottom of the coating happens almost immediately[128].

3.5   Drying regime maps for plate-like particles

Similar to the works of Cardinal et al.[66], the drying regime maps are calculated by systematically trying pair values of Pe_C and N_S and evaluating the concentration of the particles at the top or the bottom of the film after half of the maximal simulation time $\tau = \tau_{max}/2$ (see equation (1.9)), as previously mentioned in section 1.4. If the particle concentration resulting from the Pe_C and N_S pairs at the top equals 90 % of the maximal packing concentration $\phi_C(\tau_{max}, h(\tau_{max})) = 90\,\% \cdot \phi_{C,max}$, then the point corresponds to the border between the Evaporation and Diffusion regimes. The same principle applies to the Sedimentation-Diffusion regime border but evaluating the concentration at the bottom $\phi_C(\tau_{max}, 0) = 90\,\% \cdot \phi_{C,max}$.

The flow chart in Figure 3.9 explains the numerical method used in the present work to obtain the Evaporation-Diffusion regime border. The simulation requires the following input parameters to run: the number of points n for the N_S and the range $[N_S^0, N_S^{end}]$ to be evaluated, starting values for the Péclet-number Pe_C^0 and Pe_C^1, the system temperature T, initial component distribution $\phi_{i,0}$, and the particles' aspect ratio r_p to calculate the maximal packing concentration $\phi_{C,max}$ and K_2. Afterwards, the software solves the coupled PDE system and compares the concentration value at the top with $90\,\% \cdot \phi_{C,max}$, calculating an error ε. The routine uses the secant method to calculate the necessary value of Pe_C, which would minimize the value of ε by comparing the starting value of the Péclet number with the tolerance $tol = 10^{-3}$. This tolerance value produces computation times of three hours with smooth borders for the drying regime maps. Once the change of the Pe_C is lower than the tolerance, the routine starts with a new N_S value until the whole range has been evaluated. A stop condition is integrated in the routine when the binary polymer concentration exceeds the overlap concentration $\phi_P^b = 13\,\%$. The routine was programmed in C++ using the application builder of COMSOL Multiphysics 5.5. The complete program can be found in the appendix.
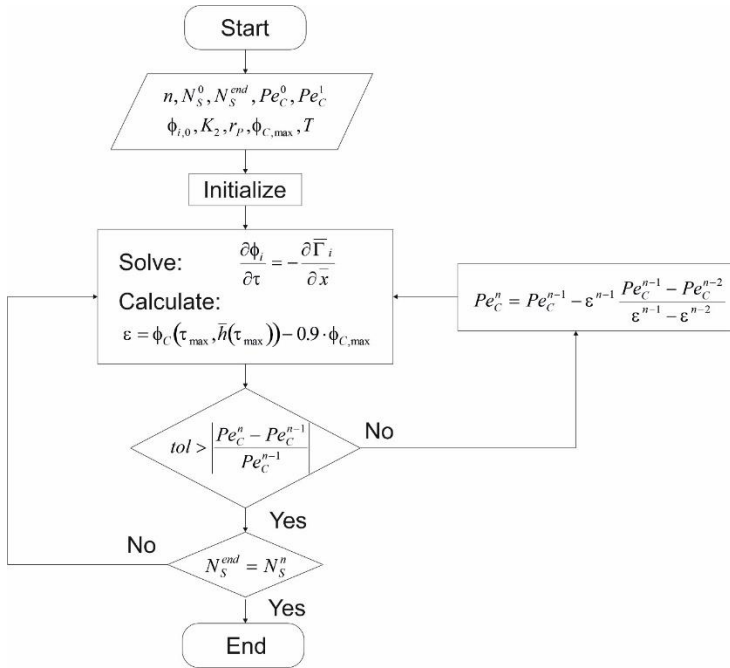
Figure 3.9. Numerical method flow chart for the Evaporation-Diffusion regime border. The input parameters for the program are: the number of points n, the interval of the drying map $\left[N_S^0, N_S^{end}\right]$, the initial estimation points $\left[Pe_C^0, Pe_C^1\right]$, initial concentration of each component $\phi_{i,0}$, the particle shape r_p, maximum packing concentration $\phi_{C,max}$, K_2 and temperature. Using the input parameters, the program solves the partial differential equation system and verifies if the particle concentration at the top corresponds to 90 % of $\phi_{C,max}$ by calculating the error ε. If the given Pe_C^n difference is less than the tolerance, then the program starts again with the next N_S^i value, if not, a new value for the Pe_C^n is calculated using the secant method until it reaches convergence. The numerical approach does not change for the Sedimentation regime border, only the error is calculated with the concentration at the bottom of the film $\phi_C(\tau_{max}, 0)$.[128]

In Figure 3.10, the drying regime map is displayed for plate-like particles with PVA at $r_p = 0.10$ and $40°C$. The chart resembles the spherical counterpart from the work of Cardinal et al.[66], it starts at low sedimentation numbers with a constant value of the Péclet-number, this diverges when N_S approaches unity, and finally the value of the Péclet number descends at first high and later lower rates. The three different possibilities for the particles to accumulate are illustrated and marked with their respective symbol. The regions in the map are defined as follows: when the particles accumulate at the top of the film is the **E**vaporation regime (E), when the particles sink to the substrate is the **S**edimentation regime (S), and finally the region where the particle concentration does not exceed 90% of $\phi_{C,max}$ at $\tau = \tau_{max}/2$ and any place in the film is the **D**iffusion regime (D).
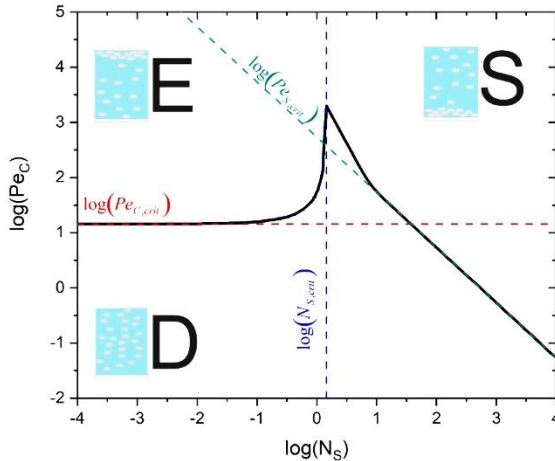
Figure 3.10. Drying regime map with initial solvent volume fraction $\phi_{S,0} = 95\%$, a particle volume fraction in the dry film $\phi_{C,dry} = 33.3\%$, and an aspect ratio $r_p = 0.10$. The three different regimes are illustrated and marked with the corresponding letter; Evaporation regime (E): the particles accumulate at the top, Sedimentation regime (S): the particles accumulate at the bottom, Diffusion regime (D): the particle concentration does not reach 90% of $\phi_{C,max}$ and therefore the particles remain evenly distributed. The borders between regimes are marked in color using the critical dimensionless numbers as follows; D-E: regime with $Pe_{C,crit}$ in red, E-S: regime with $N_{S,crit}$ in blue and S-D: regime with the line whose ordinate intercept corresponds to the $Pe_{S,crit}$, in green.[128]

The main separation of borders is defined with the critical values of Pe_C, N_S and the Péclet sedimentation number Pe_S, which can be calculated as

a product of the other two dimensionless numbers as shown in equation (3.20).

$$Pe_S = \frac{U_{C,0} \cdot h_0}{D_{C,0}} = Pe_C \cdot N_S \qquad (3.20)$$

These numbers set the change when evaporation dominates over diffusion $Pe_{C,crit}$; sedimentation dominates over evaporation $N_{S,crit}$; and sedimentation overcomes diffusion $Pe_{S,crit}$. Graphically, $Pe_{S,crit}$ can be described as the ordinate intercept of the line from the border between diffusion and Sedimentation regime at high N_S using equation (3.21).

$$\log(Pe_C) = -\log(N_S) + \log(Pe_{S,crit}) \qquad (3.21)$$

$Pe_{C,crit}$ is the limit value when the sedimentation number tends to zero $N_S \rightarrow 0$. On the other hand, there is no explicit border between the Evaporation and Sedimentation regimes, they are simply separated by the critical value of the sedimentation number $N_{S,crit}$, which is calculated by intersecting the two main border lines.

The influence of the aspect ratio was investigated and the resulting drying regime maps can be found in Figure 3.11. There is a trend for a decreasing aspect ratio, which lowers the Evaporation-Diffusion border, thus expanding the Evaporation regime for a decreasing aspect ratio. Unfortunately, the map at $r_p = 0.03$ could not be fully calculated for the Sedimentation-Diffusion border with the same conditions as given for the other two borders, because of numerical issues. Therefore, the tolerance is lowered to $tol = 10^{-2}$ to achieve convergence. The region in which the tolerance is lowered is marked with a dashed line.

The exponent K_2 is the cause of this dramatic change in the position of the borders, which move downwards with a lower aspect ratio. A lower aspect ratio at identical particle volume results in the particles getting flatter and flatter. This would mean for the fluid around the particles a greater viscous resistance to overcome, and thus a greater resistance to flow. Additionally, when the evaporation rate increases, flatter particles cannot diffuse fast enough to compensate the gradient, thus expanding the evaporation regime at a low r_p. As mentioned in the previous section, certain numerical values are not possible to simulate for the two main dimensionless numbers. The same principle applies for the sedimentation coefficient $K(\phi_C)$, which at $r_p = 0.03$ is a function raised to the power of ~45, see Figure 3.5.
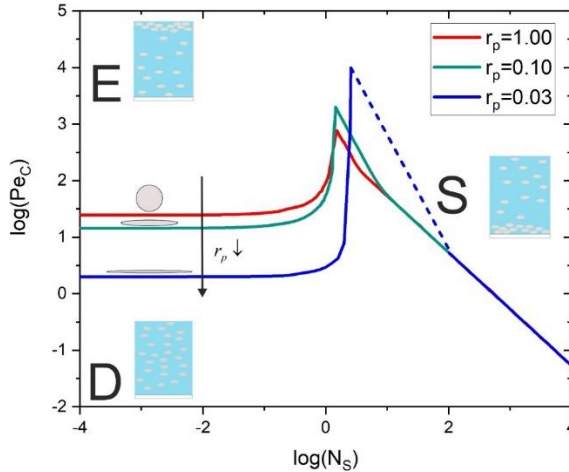
Figure 3.11. Dependence of the drying regime borders on particle aspect ratio. The lower the aspect ratio r_p, the lower the boundaries are located. The borders were simulated using the data available in the literature and experimentally obtained. The dashed area for an $r_p = 0.03$ is due to the lower tolerance in the simulation to obtain convergence.[128]

The increased shift of the borders as a function of the aspect ratio is shown in Figure 3.12. The border between Evaporation and Diffusion regime corresponds to $Pe_{C,crit}$, the implicit border between evaporation and Sedimentation regime is quantified with $N_{S,crit}$, and $Pe_{S,crit}$ defines the separation between the Diffusion and Sedimentation regime. In the studies from Cardinal et al.[66] it was concluded that $Pe_{S,crit}$ is only dependent on the initial concentration of the particles. This is also shown by the results, since all the borders at different r_p overlap at high N_S. The region $\log N_S \leq 1$ shows a different trend, because sedimentation driving forces have not yet fully overcome evaporation and the drag provoked by the flat geometry. That it is why N_S at $r_p > 0.03$ needs to be one order of magnitude greater than $N_{S,crit}$, in order to follow the same constant trend. However, for $r_p = 0.03$ we cannot be certain, due to the limitation of the simulation routine.
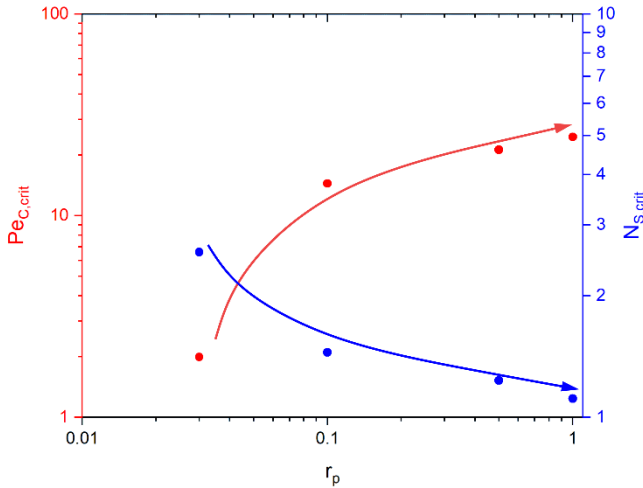
Figure 3.12. Influence of the r_p on the critical values of the Pe_C and N_S for plate-like particles. Showing an increase of $Pe_{C,crit}$ (left axis) and a decrease of $N_{S,crit}$ (right axis) at higher values of r_p (see Figure 3.10).[128]

As depicted in Figure 3.12, with an increasing aspect ratio, the critical Péclet number follows a non-monotonic increasing trend until reaching complete sphericity. On the other hand, the critical sedimentation number decreases as particles get rounder. The trend of $Pe_{C,crit}$ can be explained by the values of K_2, allowing a higher mobility as the aspect ratio of the plate-like particles increases. A higher mobility implies higher diffusion coefficients, not allowing the particles to accumulate at the top of the film. The evaporation rate is approximately the sedimentation of the particles at $z = h(t_0)$ when $N_{S,crit}$ is reached, meaning:

$$E_0 \approx U_C|_{z=h(t_0)} = U_{C,0} \cdot K(\phi_{C,0}) \qquad (3.22)$$

$$N_{S,crit} \approx \frac{1}{K(\phi_{C,0})} \qquad (3.23)$$

Equation 3.24 predicts that if the hindrance coefficient $K(\phi_C)$ decreases (aspect ratio decreases), $N_{S,crit}$ will increase at a constant initial particle concentration $\phi_{C,0}$, leading to an expansion of the Evaporation regime. Similarly for $Pe_{C,crit}$, this phenomenon is due to the decrease of mobility at a lower aspect ratio, making it harder for the particles to match the

66

speed of the evaporation front and therefore the region to obtain accumulation at the top of the film is extended to higher sedimentation numbers.

It is important to put the influence of sphericity on the drying regime maps into context. The influence of the aspect ratio is compared with the influence of the initial component concentration, which are not dependent on the physical properties of the material system. In Figure 3.13, drying regime maps are plotted at different values of the initial volume fraction of the solvent $\phi_{S,0}$ and the different particle concentration in the dry film $\phi_{C,dry}$. In the left diagram, $\phi_{C,max}$ was kept constant, while varying $\phi_{S,0}$. The reduction of the solvent leads to the obvious conclusion of the expansion of the Evaporation regime, due to the greater initial particle concentration, thus reducing the evaporation needed to reach $\phi_{C,max}$. The change of the initial concentration changes the borders almost in the same order of magnitude as changing the aspect ratio. On the contrary, the variation of $\phi_{C,dry}$ hardly changes the critical dimensionless numbers. The main reason for the Evaporation regime expansion and the low influence of the particle concentration lies in the low mobility of the plate-like particles. This intensifies the effect of the drying driving forces by raising the evaporation rate E_0, allowing the phase boundary to move faster than the particles can diffuse.
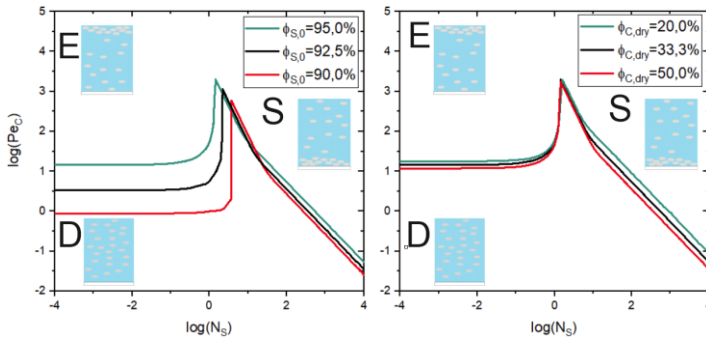
Figure 3.13. Influence of initial solvent and particle volume fraction in the dry film on the drying regime maps at $r_p = 0.10$. In the left diagram, the borders were drawn using a constant particle volume fraction in the dry film of $\phi_{C,dry} = 33.3\ \%$ and the initial solvent volume fraction is modified, showing a reduction of the Diffusion regime. This is due to the increase of the particle concentration, making it easier to fulfill the condition of the Evaporation regime at lower Pe_C. On the right, $\phi_{C,dry}$ is varied with a constant $\phi_{S,0} = 95\ \%$, which hardly produces any shift of the regime borders due to the low initial concentration $\phi_{C,0}$.[128]

It is concluded that the influence of particle geometry causes an important change of the particle distribution in the dry film. The changes of the borders are so great that one could use the particle shape as parameter to obtain a desired regime. In Figure 3.14, an example with different experimental points is plotted to show how a drying map can be used for decision making while designing a drying process or formulating a coating suspension. The used points are also tabulated in Table 1. In this figure, the maps for spherical particles and plate-like particles are plotted in red and green for a temperature of $40\,°C$. For both cases, the initial solvent concentration was set to $\phi_{S,0} = 95\,\%$ and the dry-film particle concentration to $\phi_{C,dry} = 40\,\%$. Likewise, the experimental points are plotted in color, depending on the aspect ratio of the particles, and are calculated using the particle diameter d_C, the initial evaporation rate E_0, and the initial film height h_0. Additionally, the experimental points consider a particle density of $\rho_C = 2600\,kg/m^3$, and a density of the polymer solution of $\rho_{S,P} = 1060\,kg/m^3$. The particle diameter for the plates is calculated to match the volume of the sphere counterpart, assuring that any changes in the regime map only comes from the geometry of the particles.

At the bottom of the map, three different cases with an increasing particle size are displayed. The initial film height is $100\,\mu m$ and the initial evaporation rate $0.01\,\mu m/s$. The particle diameters plotted are $0.10\,$, $0.50\,$ and $1\,\mu m$, which correspond to 0.215, 1.08 and $2.15\,\mu m$ equivalent diameter for the plates. In this example, increasing the particle size results in moving up diagonally to the right, due to the increase of the sedimentation velocity and decrease of the sedimentation coefficient. Similarly, in the center there are three cases with increasing evaporation rates of 0.01, 0.1 and $1\,\mu m/s$, a sphere particle size of $1\,\mu m$ and a film height of $100\,\mu m$. These cases show a diagonal increase to the left of the map. Finally, in the region of $\log(N_S) = -1.3$, the film height is varied to values of 100, 500 and $1000\,\mu m$, using a particle size of $0.1\,\mu m$ and an evaporation rate of $0.01\,\mu m/s$. The increase of the film height leads to an obvious increase upwards.

In all the cases the plate-like particle points are located on top of the spherical. As mentioned in the previous sections, the flattening of the particle while retaining the same volume leads to an increase of the drag: Decreasing the diffusion coefficient and the sedimentation rate leads to a locating of the points at higher Péclet numbers and lower sedimentation numbers in comparison to spheres.

It can be observed that for this example the plate-like particles are distributed in the Evaporation and Sedimentation regime, whereas most of the spheres are in the Diffusion regime. If the location of spherical particles in a coating were to be located at the top of the film by increasing the initial film height from $100\ \mu m$ to $1000\ \mu m$, it would barely be enough to reach the Evaporation regime. On the contrary, plate-like particles reach the Evaporation regime by increasing the initial film thickness h_0 by a factor of five. Therefore, changing the particle geometry gives another possibility for designing drying processes.
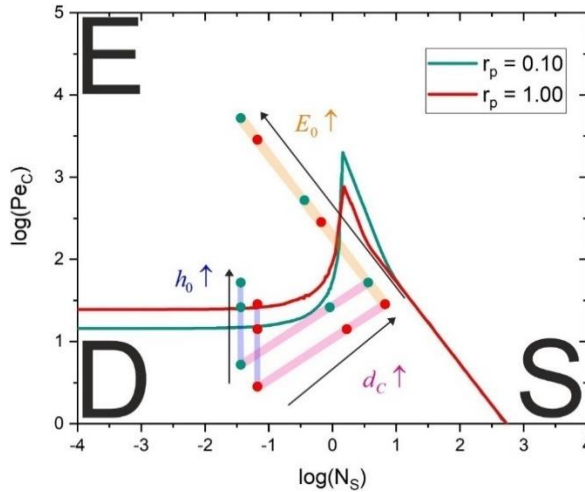
Figure 3.14. Drying regime map for spherical particles plotted in red ($r_p = 1.00$) and plate-like particles plotted in green ($r_p = 0.10$), showing how the particle size d_C, the evaporation rate E_0 and the initial coating film height h_0 affect how the particles are going to distribute over the dry film height. Near the bottom center of the map are three cases at increasing particle size with an evaporation rate of $0.01\ \mu m/s$, an initial film height of $100\ \mu m$, and particle diameters of 0.1, 0.5 and $1\ \mu m$: The plate-like particles are plotted at the same conditions with an equivalent diameter to achieve the same volume as their spherical counterparts. At the center, three cases at increasing evaporation rates of $0.01, 0.10, 1.00\ \mu m/s$ with a particle size of $1\ \mu m$ and a film height of $100\ \mu m$ are shown. The remaining three cases with increasing film height of $100, 500, 1000\ \mu m$ with an evaporation rate of $0.01\ \mu m/s$ and a particle size of $0.1\ \mu m$ are shown.

Table 1. Example points utilized in Figure 3.14, showing the necessary criteria to calculate Pe_C and N_S from. The same initial viscosity is used for all the given points with a value of $\eta_{S,P} = 1.3 \cdot 10^{-2} \ Pa \cdot s$.

d_C [μm]	r_p [−]	$D_{C,0}$ [$m^2 s^{-1}$]	$U_{C,0}$ [$m^2 s^{-1}$]	h_0 [μm]	E_0 [$m\ s^{-1}$]	N_S [−]	Pe_C [−]
1.0	1.0	$3.5 \cdot 10^{-14}$	$6.7 \cdot 10^{-8}$	100	$1.0 \cdot 10^{-8}$	$2.8 \cdot 10^{1}$	$6.7 \cdot 10^{0}$
0.5	1.0	$7.0 \cdot 10^{-14}$	$1.7 \cdot 10^{-8}$	100	$1.0 \cdot 10^{-8}$	$1.4 \cdot 10^{1}$	$1.7 \cdot 10^{0}$
0.1	1.0	$3.5 \cdot 10^{-13}$	$6.7 \cdot 10^{-10}$	100	$1.0 \cdot 10^{-8}$	$2.8 \cdot 10^{0}$	$6.7 \cdot 10^{2}$
2.2	0.1	$1.9 \cdot 10^{-14}$	$3.6 \cdot 10^{-8}$	100	$1.0 \cdot 10^{-8}$	$5.2 \cdot 10^{1}$	$3.6 \cdot 10^{0}$
1.1	0.1	$3.8 \cdot 10^{-14}$	$9.1 \cdot 10^{-9}$	100	$1.0 \cdot 10^{-8}$	$2.6 \cdot 10^{1}$	$9.1 \cdot 10^{-1}$
0.2	0.1	$1.9 \cdot 10^{-13}$	$3.6 \cdot 10^{-10}$	100	$1.0 \cdot 10^{-8}$	$5.2 \cdot 10^{0}$	$3.6 \cdot 10^{-2}$
1.0	1.0	$3.5 \cdot 10^{-14}$	$6.7 \cdot 10^{-8}$	100	$1.0 \cdot 10^{-7}$	$2.8 \cdot 10^{2}$	$6.7 \cdot 10^{-1}$
1.0	1.0	$3.5 \cdot 10^{-14}$	$6.7 \cdot 10^{-8}$	100	$1.0 \cdot 10^{-6}$	$2.8 \cdot 10^{3}$	$6.7 \cdot 10^{-2}$
2.2	0.1	$1.9 \cdot 10^{-14}$	$3.6 \cdot 10^{-8}$	100	$1.0 \cdot 10^{-7}$	$5.2 \cdot 10^{2}$	$3.6 \cdot 10^{-1}$
2.2	0.1	$1.9 \cdot 10^{-14}$	$3.6 \cdot 10^{-8}$	100	$1.0 \cdot 10^{-6}$	$5.2 \cdot 10^{3}$	$3.6 \cdot 10^{-2}$
0.1	1.0	$3.5 \cdot 10^{-13}$	$6.7 \cdot 10^{-10}$	1000	$1.0 \cdot 10^{-8}$	$2.8 \cdot 10^{1}$	$6.7 \cdot 10^{-2}$
0.1	1.0	$3.5 \cdot 10^{-13}$	$6.7 \cdot 10^{-10}$	500	$1.0 \cdot 10^{-8}$	$1.4 \cdot 10^{1}$	$6.7 \cdot 10^{-2}$
0.2	0.1	$1.9 \cdot 10^{-13}$	$3.6 \cdot 10^{-10}$	1000	$1.0 \cdot 10^{-8}$	$5.2 \cdot 10^{1}$	$3.6 \cdot 10^{-2}$
0.2	0.1	$1.9 \cdot 10^{-13}$	$3.6 \cdot 10^{-10}$	500	$1.0 \cdot 10^{-8}$	$2.6 \cdot 10^{1}$	$3.6 \cdot 10^{-2}$

4 Results and Discussion

In this section, drying experiments are compared with simulation results from the previous chapter. Utilizing aqueous PVA with silica flake particles, coatings were cast and subsequently dried. The distribution in the dry film was determined using 3-D Raman spectroscopy. During data treatment, a new tool for the morphology investigation was developed. By combining the single 2-D cross sections, a 3-D construct of the dry film can be built up. This new approach gives the opportunity to localize single particles or agglomerates in the film in a non-invasive process. All the simulated regimes using the proposed approach can be obtained experimentally, thus confirming that plate-like particles also produce similar particle distributions.

Each drying experiment is localized in the calculated drying regime maps to confirm if the concentration in the dry film corresponds to the predicted particle distribution on the chart. Unfortunately, the commercially available material systems that can be used for the validation of the charts are limited, mostly due to the transparency required for Raman spectroscopy, or the aspect ratio distribution is not monomodal[131].

The limitations of the simulation model are also addressed in this chapter and experimentally studied using a fluorinated polymer and graphene oxide composites. As stated in Chapter 3, the decrease in aspect ratio increases the particle viscous drag and with it the Evaporation regime area. Moreover, the decrease of the initial particle concentration increases the particle mobility and expands the Diffusion regime. Graphene-based coating inks used for the functionalization of fuel cell membranes are dilute and the particle aspect ratio tends to zero. This material system exceeds the capabilities of the simulation model and it is therefore experimentally investigated to identify which mechanism is dominant.

4.1 Particle distribution in the dry film

The particle distribution in the dry film was determined using 3-D micro Raman spectroscopy imaging. To this end the material system is required to be transparent to minimize light scattering. The polymer-particle pair used in this work fulfills this requirement and has been extensively studied

with physical data available. Glass particles can be easily identified in the Raman spectra due to their transparency and characteristic peaks. Moreover, aqueous PVA solutions are coatable liquids capable of producing homogeneous wet films and PVA has good mechanical properties reducing the formation of coating defects like cracks. The samples were dried using force convection with the devices described in section 2.5. The coatings were measured in the center to minimize the influence of edge effects. Due to the time required to make a measurement, the investigated area was limited to $100 \, x \, 100 \, \mu m^2$.

One of the main challenges of the experimental validation is the ability to move along the drying regime map without changing the aspect ratio. Unlike spheres, changing the particle size of plates also changes their mobility and therefore the borders of the map must be recalculated again. In other words, while experimentally investigating the drying regimes predicted in section 3.5, it is only possible to change the drying rate E_0 and the initial wet film height h_0 to modify the dimensionless numbers, without compromising the aspect ratio. This is due to the limitations of finding commercially available plates with constant aspect ratio but different particle size. Moreover, the synthesis of plate-like particles with low aspect ratio distribution requires high precision machinery and the recuperation process requires several steps[131]. Therefore, at a given particle size ratio by changing the evaporation rate one is moving along a line. If E_0 ↑ increases, then Pe_C ↑ increases and N_S ↓ decreases and vice versa, as depicted in Figure 4.1. By modifying the film height one can move up and down in the map, but as previously mentioned, the spectrometer has a resolution of $2 - 3 \, \mu m$. This also limits the possibilities to move the experiments into the Diffusion regime.
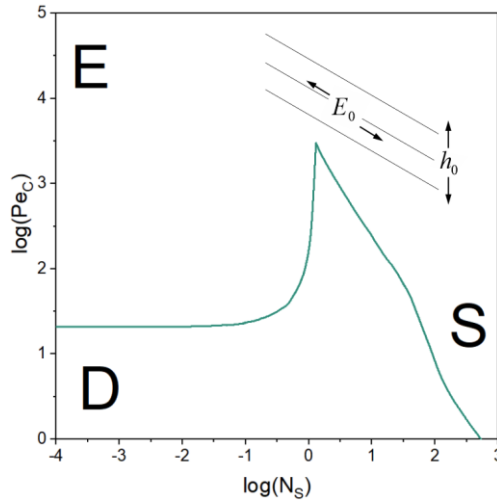
Figure 4.1. Drying regime map showing the limitations of the experimental valida-tions at a fixed particle aspect ratio $r_p = 0.1$. By increasing the evaporation rate E_0, the experimental points move diagonally upwards and vice versa. Changing the initial wet film height h_0 moves the experiments up and down in the chart.

Changing the polymer content could also modify the sedimentation num-ber by increasing or reducing the viscosity of the liquid via the polymer content. As mentioned in the previous sections, there is not much of an influence on the position of the regime borders by changing the ratio be-tween the solids. Nevertheless, the amount of solvent must remain the same and by increasing the polymer content the overlap concentration will be reached faster, resulting in a small change in the dimensionless numbers.

The spectral information is obtained by systematically moving the focal point, meaning that the measurements occur in a discrete manner. This implies that there is the possibility to encounter regions with only particles and the resulting concentration being higher than the maximal packing concentration ($\phi_{C,max} = 52\%$). In Figure 4.2 and Figure 4.3, the resulting 3-D images are displayed, showing how the particles are distributed in the dry film. The diagrams were plotted utilizing the isosurface function in Matlab and are created by interpolating the values in three dimensions at a given value of the particle concentration. The structures that appear in

the figures correspond to a particle concentration of $\phi_C > 80\ \%$. Due to the difficulty of observing a 3-D model in a two-dimensional space, a color gradient is added to identify were the plates are located along the film's height, thus allowing us to qualitatively determine the drying regime of the sample. However, the simulation program did not consider the diffusion in the horizontal directions x and y, and the concentration of the particles does not remain completely unchanged along these axes. In the images, holes can be seen between the particles, due to particle geometry defects and the formation of agglomerates. The inhomogeneity of the lateral concentration profiles poses a problem to accurately determine the resulting regime. Therefore, to obtain a representative concentration profile, an average integral concentration $\bar{\phi}_{C,dry}(z)$ is calculated from the Raman measurements using equation (4.1). Integration was done numerically using a $5\ \mu m$ grid. The resulting integration is plotted along the normalized dry film height h/h_{dry}.

$$\bar{\phi}_{C,dry}(z) = \frac{\int_0^{100\ \mu m} \int_0^{100\ \mu m} \phi_{C,dry}(x,y,z)\ dxdy}{\int_0^{100\ \mu m} \int_0^{100\ \mu m} dxdy} \qquad (\ 4.1\ )$$

In Figure 4.2 it can be seen that most of the particles are in the upper part of the sample, showing some "blank" spaces in the upper right corner. It is important to mention that particles could be in other parts of the film, but not at a concentration as high as previously mentioned, as can be seen from the average particle volume fraction. The bottom of the film is at a volume fraction of $32\ \%$ and this increases towards the upper part of the film, barely exceeding the maximal packing concentration, meaning that the sample morphology belongs to the description of the Evaporation regime, showing that using both, 3-D Raman imaging (qualitative) and average particle concentration (quantitative), the corresponding particle concentration in the dry film can be identified. In Figure 4.3 another particle distribution can be seen. In this case the particles appear to be more packed along the film height but still show the "blank" spaces. The average concentration corresponds to the 3-D model with the volume fraction tending to a constant value by serpentizing around the dry film concentration value ($\phi_{C,dry} \approx 41\%$), confirming that the Diffusion regime distribution with plate-like particles can be experimentally obtained.
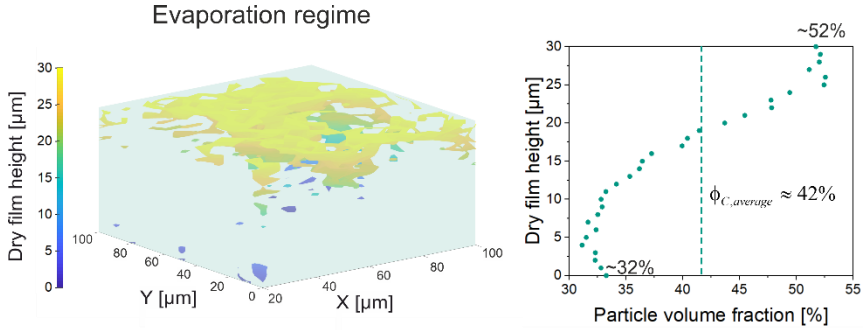
Figure 4.2. Left: three-dimensional micro 3D Raman image showing the glass flakes' distribution in a dry film qualitatively. The flakes with $r_p = 0.1$ are marked with a colour gradient to indicate their position in the film; PVA and regions with a low particle concentration ($\phi_C < 80\%$) are marked in green. An Evaporation regime example from sample 1 at $log(Pe_C) = 5.20$ and $log(N_S) = 0.06$ (see Table 2) can be observed.[69]. Right: average particle volume fraction extracted from the left image and calculated using equation (4.1), showing a concentration gradient from the bottom at 32%, to the top at 52%.
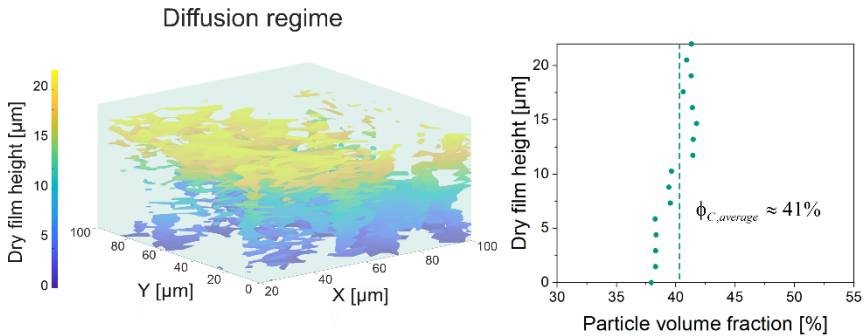
Figure 4.3. Left: three-dimensional micro 3D Raman image showing the glass flakes' distribution in a dry film qualitatively. The flakes with $r_p = 0.1$ are marked with a colour gradient to indicate their position in the film; PVA and regions with a low particle concentration ($\phi_C < 80\%$) are marked in green. A Diffusion regime example from sample 10 at $log(Pe_C) = 3.97$ and $log(N_S) = 0.74$ (see Table 2) can be observed.[69]. Right: average particle volume fraction extracted from the left image and calculated using equation (4.1), showing an almost homogeneous distribution of the particles around 41%.

In Figure 4.4, selected particle concentration profiles in a dry film are plotted as an example of how the different samples were quantitatively

classified as Evaporation, Sedimentation, or Diffusion regime. The concentration gradient along the film height remains visible in the dry film for the Evaporation and Sedimentation regime experiments. Even though, the final particle concentration in the dry film does not remain at the simulation termination condition of $\phi_C = 90\% \cdot \phi_{C,max}$ at the top or the bottom of the film.
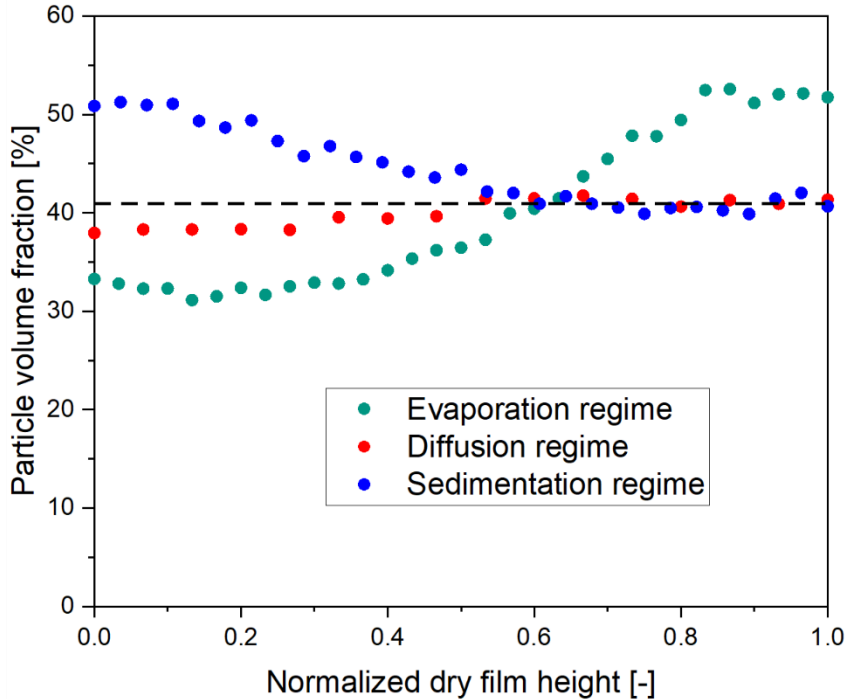
*Figure 4.4. Integral average concentration profiles along the normalized film height h/h_{dry}, showing the three different regimes: **E**vaporation, **D**iffusion and **S**edimentation. The sample numbers used in this diagram can be found in Table 2, the numbers are 2 for evaporation, 10 for diffusion, and 8 for sedimentation.[69]*

The drying conditions were systematically changed with their corresponding Péclet and sedimentation numbers in order to identify other regimes of particle profiles and to compare them with the prediction from the simulations. It is only possible to change the film's height h_0 by setting the gap between the coating knife and the drying rate by changing the air flow

and with it the HTC in the drying device. A complete collection of these parameters, as well as the experimentally observed regimes are listed in Table 2.

*Table 2. Coating and drying experiment parameters of glass flakes at $r_p = 0.1$ with their respective regime classification, E for **E**vaporation, S for **S**edimentation and D for **D**iffusion. [a] Concentration profiles are plotted in Figure 4.2 and Figure 4.3 [b] Sample's morphology can be seen in Figure 4.4.*

Sample	h_0 [μm]	α [$W\,m^{-2}K^{-1}$]	E_0 [$\mu m\,min^{-1}$]	$\log Pe_C$ [$-$]	$\log N_S$ [$-$]	Observed Regime
1	500	21.05	66	4.82	0.33	**E**
$2^{a.b}$	500	19.42	157	5.20	0.60	**E**
3	500	19.44	94	4.97	0.44	**E**
4	500	14.80	79	4.90	0.24	**E**
5	500	4.69	4	3.65	2.63	**S**
6	500	6.64	6	3.80	2.48	**S**
7	800	6.64	6	4.01	2.48	**S**
8^a	800	13.26	23	4.57	0.73	**S**
9	500	15.58	26	4.42	0.73	**D/S**
$10^{a.b}$	200	14.96	47	3.97	0.74	**D**

The criterion to classify the sample as Evaporation or Sedimentation regime is to have a concentration gradient greater than 10 %. In a similar way, all the samples in Table 2 were classified and plotted in the drying regime map to confirm the predicted concentration profile. Each point is labeled according to the observed regime, as seen in Figure 4.5. All experiments were conducted in triplicate to ensure reproducibility. As already mentioned, no Diffusion regime experiments could be conducted due to the difficulty of lowering the values of Pe_C. It is not enough to lower the evaporation rate to land in the Diffusion regime. The particle size must also be adjusted to avoid a higher N_S. The proper acquisition of a Raman

spectrum of the particles requires that the particle thickness must be at least $1\,\mu m$. This made it difficult to find particles having the same aspect ratio but a lower size from the same manufacturer. Most of the sedimentation experimental points lay in the predicted regime, showing good agreement with the simulation.
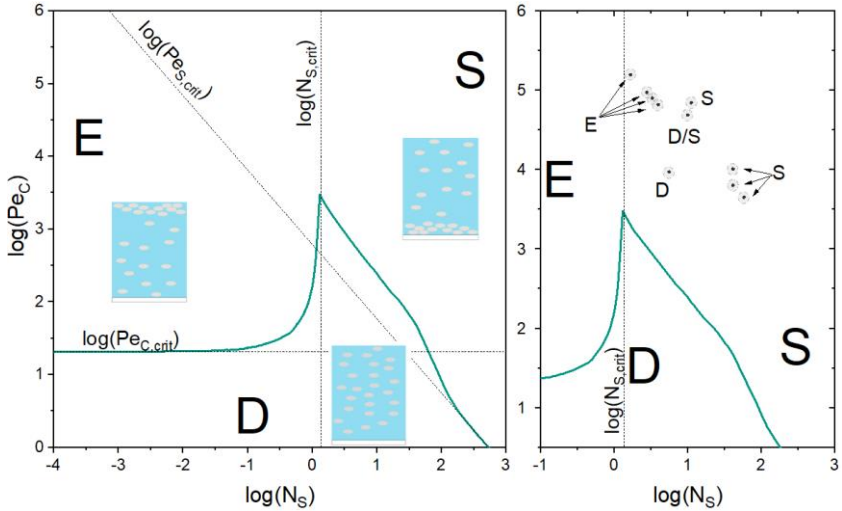
Figure 4.5. Zoomed-in drying regime map of glass flakes at $r_p = 0.1$ with all the evaluated experimental points. The area around the points shows the error in the calculation of Pe_C. The letter near the points denotes the observed regime in the dry: **E**vaporation regime E, **D**iffusion regime D, and **S**edimentation regime S.[69]

The particle distribution obtained in Sample 9 was not reproducible. The Sedimentation regime was obtained twice and the Diffusion regime once, despite conducting the experiment at the same conditions. Therefore, Sample 9 is marked with both letters. Sample 10 was found to be in a completely different regime. This deviation from the simulation can be attributed to the location of the experiments near the Evaporation−Sedimentation regime border. At this location, the particles can do both, sediment and accumulate at the top of the film. Because of film shrinkage during drying, the particles come close together and it could appear that the observed regime is Diffusion. The proposed mechanism for these results is depicted in Figure 4.6.
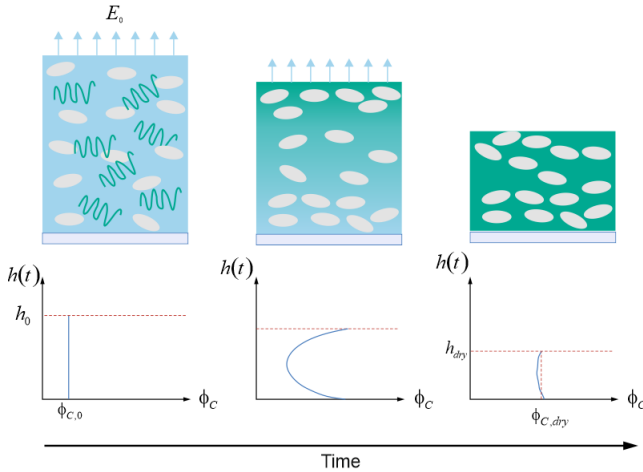
Figure 4.6. Proposed drying mechanism for the drying experiments near the border between the Evaporation and Sedimentation regime, where the particles tend to accumulate at the bottom and the top of the film but due to the shrinkage of the film the particle distribution appears to be in a Diffusion regime.

4.2   Applications and limitations of the model

The accumulation of polymer on the top of the film, or skin formation, is a configuration that unfortunately cannot be simulated due to the high values of the corresponding Pe_C, which makes the simulation diverge. Therefore, such cases are not contemplated in this work. But it is experimentally accessible by choosing the drying conditions. Additionally, all the experimental and theoretical conditions were conducted at constant temperature[51]. If the drying process is not isothermal, the physical properties must be given as a function of the temperature, to allow the simulation to solve for the temperature as another variable.

During the systematic change of simulation input parameters, it was noted that for initial particle concentrations higher than $\phi_{C,0} \geq 10\%$ the simulation does not converge, due to the mobility of the particle tending to zero. This is because most of the models utilized in the simulation do not consider interactions between more than three particles nor the effects of plates colliding at different angles[132][133]. Thermodynamic

behavior between the particles and the polymer solution, like dissolution or crystallization of the particles, or liquid-liquid phase separation are not considered in the model. It was stated that the particles were not soluble in the liquid. Nevertheless, there are some particle-solvent systems which can separate into two phases during drying. The phase separation in polymeric solutions is dependent on the concentration, temperature, and interaction between components of the material system. More information about phase separation in polymeric solutions can be found elsewhere[54].

One of the major applications found for plate-like-particle-composites can be found in graphene components and antibacterial silver nanoplates. The mayor difference with other composites, e.g. batteries, is the amount of particles present in the system. Battery slurries for example have more than $50\% \, w/w$ solid particles, whereas a printable graphene ink, used to increase the selectivity of the membranes in Direct Methanol Fuel Cells (DMFC) by reducing the passing of methanol, has a particle concentration of $0.05 \, g/L$ ($10^{-5}\% \, w/w$) in the coating. This major difference resides in the low amount of particles to achieve the functionality of the device. As displayed in Figure 3.13, the reduction of the initial particle and polymer concentrations expands the Sedimentation regime due to the inability of the particles to accumulate on the top of the film before the polymer chains overlap. This is in competition with the mobility reduction at low particle aspect ratio. Graphene is defined as long monoatomic sheets, which will make the aspect ratio tend to zero, $r_p \to 0$, and with it the particle mobility too $K_2 \to -\infty \, U_C(\phi_C) = D_C(\phi_C) \to 0$. If the particles are not able to move, the Evaporation regime spreads out. Hence, a competition between the infinite dilution and infinite flattening of the particles exists. Understanding which of these forces is dominant is crucial for the production of composite films, like functionalized membranes[14].

Graphene particles coated onto a membrane form a structure which increases the length of the path for molecules to defuse across the membrane. [134,135]. For the application as a barrier layer, it is important that the particles remain homogenously distributed with an orderly stacking of the plates, in other words the concentration must correspond to the Diffusion regime.[14,22]

In the present work[*], graphene composites were studied to evaluate the limitations of the simulation approach. The material system consisted of an ionomer solution, which would reduce the chemical difference with the membrane using an entangled version of the ionomer and graphene oxide particles. The ethanol-based ionomer Fumion™ solution $10 \% \, m/v$ FSLA1010 was purchased from FumaTech GmbH. Its chemical nature is similar to Nafion™, having a ramified fluorinated structure. The graphene particles correspond to graphene oxide flakes obtained by plasma reactors at a concentration of $0.055 \, g/L$ produced at the Leibniz Institute for Plasma Science and Technology in Greifswald. Similar to the experiments in the previous sections, the sedimentation velocity at low concentration was evaluated and coatings were dried.

Sedimentation rates of graphene oxide flakes can be found in Figure 4.7, at the concentration in the order of magnitude similar to a coating ink. As expected, almost no difference can be observed at different concentrations. Instead, a trend around a constant value of $U_C = 0.031 \, \mu m/s$ is found, which is lower the compared to the glass flakes values (about four orders of magnitude for the plates at $r_p = 0.10$). This result makes the sedimentation coefficient tend to unity $K(\phi_C) = 1$. This simplifies the particle's net volume flux Γ_C to:

$$\Gamma_C = D_{C,0} \frac{\partial \phi_C}{\partial z} + U_{C,0} \phi_C \qquad (4.2)$$

The absence of a particle shape influence on the mass transfer of the graphene oxide shifts the change of the particle mobility to the viscosity of the ionomer solution and the particle size. Unfortunately, due to the low concentration, it is impossible to simulate a drying regime chart for the graphene flakes, because unless the Péclet number is extremely high $Pe_C \rightarrow \infty$ it is unrealistic to reach 90 % of the total packing concentration. Hence, diffusional forces will be dominant and the particle distribution will remain constant along the film's height.

Figure 4.7. Graphene oxide flakes sedimentation velocity as a function of volume fraction showing almost no change due to the extreme dilution of the particles. The measurements were done at the Institute of Mechanical Process Engineering and Mechanics (MVM).

Determining which phenomenon controls the mass transfer during the production of composites requires drying experiments at industry relevant conditions. To this end, graphene oxide flakes dispersed in ethanol, with a concentration of $0.055\ g/L$, were combined with a $10\ \%\ m/v$ solution of Fumion™ in a volume ratio of $1:2$. Similar to the PVA dispersion, this coating ink was sonicated to avoid the formation of agglomerates and was cast onto a thin glass substrate using a coating knife. Subsequently the coating samples were dried using the Comb Nozzle dryer at $T = 20\ °C$ with a HTC of $\alpha = 20$ and $40\ W\ m^{-2}\ K^{-1}$. In Figure 4.8, a light optical microscope image of a coating sample is shown. The image is for an area of $500 \times 500\ \mu m^2$. The image analyzing software can use the contrast to identify where the graphene flakes are located. From a qualitative point of view, it would appear that all the flakes are evenly distributed along the composite. To confirm this claim, the samples were analyzed using 3-D Raman spectroscopy
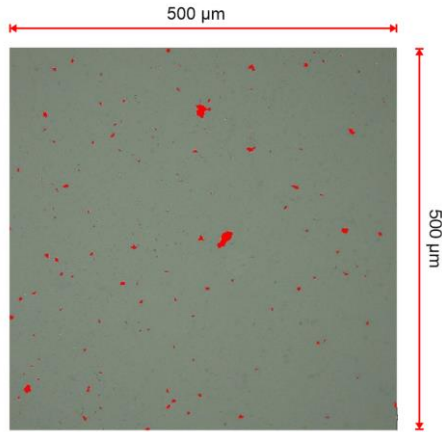
Figure 4.8. Optical microscope pictures of a $500 \times 500 \ \mu m^2$ coated fuel cell membrane with an ink made of graphene oxide flakes and Fumion at $\alpha = 40 \ W \ m^{-2} K^{-1}$ and $T = 20 \ °C$, where the image analyzing software identified the particles marking them in red.

Figure 4.9 shows the pure component spectra of graphene oxide flakes and the Fumion ionomer. The characteristic fluorine peak can be found at $720 \ cm^{-1}$. In the literature, the most intense peak for graphite at $\sim 1580 \ cm^{-1}$ has been labelled G and the second most intense D at $\sim 1350 \ cm^{-1}$. The intensity of these peaks can be related to the crystal geometry caused by the carbon atom hybridization (sp^2)[136]. On the right side of the spectrum, a minor peak labelled 2D at $\sim 2700 \ cm^{-1}$ can be seen, which is correlated with the number of the sp^2 layers. The higher the 2D peak intensity, the less graphite layers are present[137]. Hence, when the Raman intensity of 2D is dominant, the presence of graphene in the sample can be confirmed. A band next to the 2D peak can also be observed. This is caused by the oxygen functional groups attached to the edges of the low-layer carbon sheets, which causes a change in the hybridization to sp^3[138]. The purity of the graphene sample is calculated through the intensity ratio between the G and 2D peaks I_G/I_{2D} [139], which translates in the number of single carbon layers stacked on top of each other .
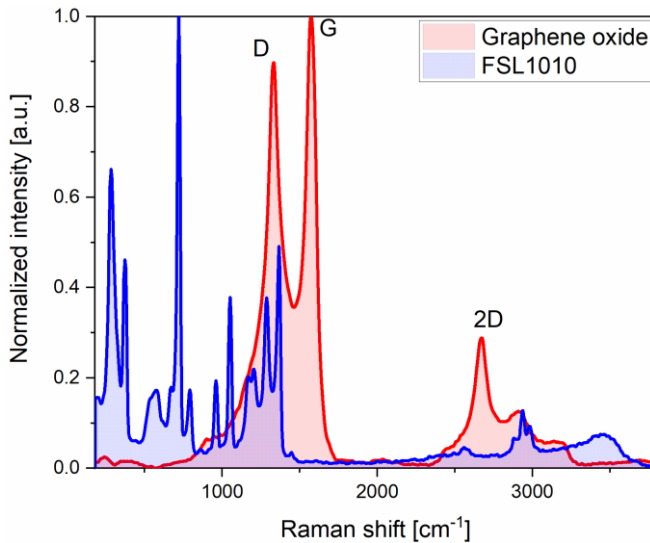
Figure 4.9. Graphene oxide and Fumion FSL1010 Raman spectral information, showing the characteristic peaks from graphene oxide (D at $1350\ cm^{-1}$, G at $1580\ cm^{-1}$, and 2D at $2700\ cm^{-1}$) and the fluorine peak of the ionomer $720\ cm^{-1}$.

The coatings were analyzed using the Raman spectrometer as described in section 2.2.1. As previously mentioned, the extremely low concentration of the graphene flakes makes it harder to quantify a physical property as a function of the concentration. That is also the case for the Raman intensity ratio, which would allow us to convert the Raman measurements into concentration profiles, as in the PVA and glass flake experiments described in section 2.2.2. Here, the content of graphene was studied by the pure intensity ratio to determine if there are any concentration gradients along the dry film's height[34]. Due to the thickness of the graphene flakes it is not possible to use the same imaging tool to plot the particles, which requires the particles to be at least $1\ \mu m$ thick. In Figure 4.10, intensity ratios averaged along the y-axis are plotted and compared at different X-positions in the dry film with an investigated sample area of $100\ \times 100\ \mu m^2$. As in Figure 4.3, the intensity ratio profiles tend to an average value of $\bar{\alpha}_{Gr} = 0.12$, showing that the graphene flakes tend to distribute homogeneously along the dry film's height.
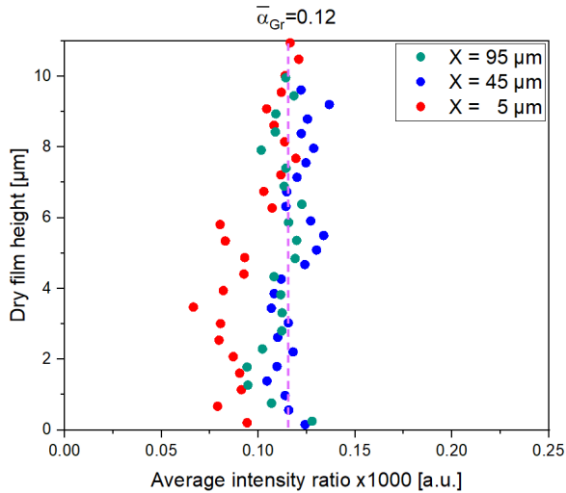
Figure 4.10. Averaged intensity ratio of graphene oxide along the ionomer coating, showing an almost constant value of $\bar{\alpha}_{Gr} = 0.12$ at different longitudes of the X axis. The coating was dried at $\alpha = 20\ W\ m^{-2}K^{-1}$ and $T = 20\ °C$.

Figure 4.11 shows the averaged intensity ratio across the sample area of two coatings dried at $\alpha = 20\ \mathrm{W\ m^{-2}K^{-1}}$ and $\alpha = 40\ \mathrm{W\ m^{-2}K^{-1}}$. The intensity ratio barely changes across the area. In both coatings some high concentrated graphene points can be observed. The sample which was dried at a higher HTC shows more inhomogeneities than the sample dried at a lower drying rate. Nevertheless, most of the sample has a homogenous particle distribution, tending to the same average value of $\bar{\alpha}_{Gr} = 0.12$. These findings confirm that the diffusive driving forces are dominant and the drag forces caused by the particle shape do not control the particle distribution in dry film. Showing one of the main limitations by using this simulation approach while designing drying processes. One question yet to be answered is the critical concentration value, at which the influence of the concentration and the flatness of the particles is in the same order of magnitude
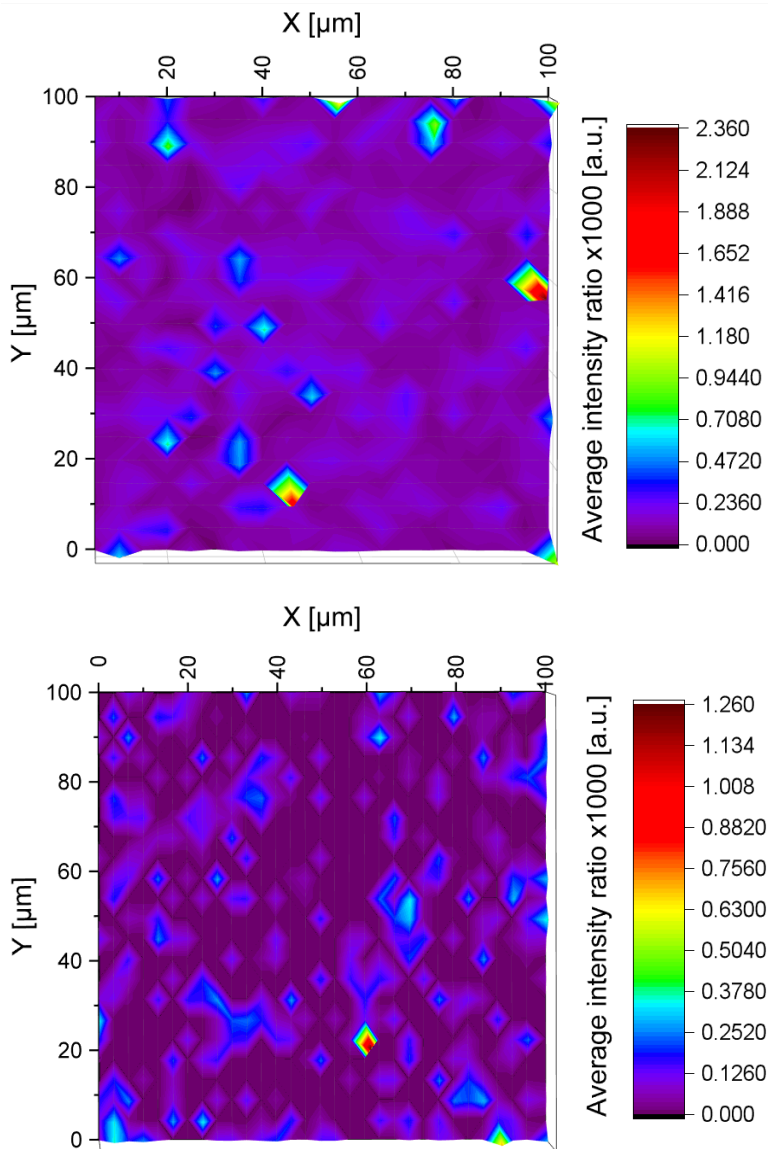
Figure 4.11. 3-D Raman imaging of a Fumion - graphene oxide coating dried at $\alpha = 20\ W\ m^{-2} K^{-1}$ (upper image) and $40\ W\ m^{-2} K^{-1}$ (lower image) with $T = 20\ °C$, showing a homogenous distribution in the lateral direction.

5 Conclusions

5.1 Summary

The objective of this work was to determine the influence of particle shape on the component distribution in composite coatings. To this end, a simulation developed from previous works was adapted to describe the mass transfer of particles while drying and drying regime maps for prediction of particle distributions in a dry film could also be plotted as a function of the sphericity of the particles. The study was limited to plate-like particles, which resemble the geometry of technically relevant materials like graphene. Experimental checking was done stepwise, firstly by choosing a polymer-particle system that could produce a stable dispersion and a wet film. Afterwards, the material system was characterized and the viscosity of the dispersion was investigated to confirm it could be modeled using rheological expressions similar used to the case for spherical particles. Once the coating dispersion was characterized, the orientation of the particles was studied and the causes of rotation identified. Finally, with the obtained physical information, the simulation routine was changed accordingly, and new regime maps were drawn. Experimental validation was conducted by systematically changing the drying conditions to induce different particle distributions in the dry film and comparing with the predictions from the drying regime maps.

PVA was chosen as the polymer due to its mechanical properties, which produce a stable dry film. Also, while it is dissolved in water it creates a homogeneous wet film. Moreover, there is extensive thermodynamic data of aqueous PVA solutions, which makes it ideal to limit the necessary experiments needed to implement the simulation. Glass flakes made mostly of silicon oxide plates were utilized as plate-like particles due to their commercial availability at two different sizes and aspect ratios. Additionally, its transparency makes them ideal to be identified using Raman spectroscopy. With the ternary system water-polyvinyl alcohol-glass flakes it was possible to produce homogeneous wet films to up to a particle volume fraction of $\phi_C = 6\,\%$ and a binary polymer concentration of $\phi_P^b = 13\,\%$, which corresponds to the overlap concentration. Additionally, with the chosen composite, Raman active dry films could be generated,

which made it possible to quantitatively investigate the distribution of the single components.

The zero shear viscosity of the dispersion was investigated at different particle concentrations ranging from $\phi_C = 0.5$ % to $\phi_C = 6$ % and at a fixed polymer content of $\phi_P = 3$ %. The results were fitted utilizing the Batchelor and Krieger-Dougherty expressions to verify if the existing models for spherical particles could be adapted. The fit for both systems showed a fair concordance with the experimental data, with the Krieger-Dougherty model having more accuracy at low particle concentration. However, due to its dependence on the maximum particle concentration, which changes depending on the orientation of the particles, it was decided to use Batchelor-like fits, that are only dependent on the volume fraction.

Sedimentation experiments were conducted to adapt the concentration dependency expressions used in the simulation model. To this end the settling velocity was measured using analytical centrifuge. The sedimentation rates were subsequently fitted utilizing the modified Batchelor expression for the sedimentation of hard spheres showing an excellent agreement (see Figure 2.13). This allowed us to correlate the exponent K_2 from equation (3.18) with the aspect ratio r_p, by proposing an expression based on the potential between two particles. This expression was later used to predict the normalized sedimentation rates from particles in different mediums and at different aspect ratios. The proposed model has a remarkable agreement with the experimental data, as shown in Figure 3.6. These findings are crucial for the automation of the simulation routine, because it is only necessary to determine the aspect ratio to describe the sedimentation and diffusion of plate-like particles.

Orientation of plate-like particles during coating and drying was investigated. Experimentally the orientation was investigated by preparing dispersions, coating them and determining the angle of the particles, in the wet film using Cryo-SEM experiments, and in the dry film with 3-D micro Raman spectroscopy. Theoretically the orientation was investigated by identifying the forces applied to the particles while processing composite films. It was experimentally found that directly after coating the particles are oriented mostly horizontally or lightly crooked. In the dry film this orientation remains, showing that the sedimentation and drying processes

do not significantly alter the angle of the particles. By theoretical studies from literature, the observed phenomena were explained as follows: during the formulation and before the coating step, the particles are randomly oriented, the coating step produces a simple shear stress that changes the angle and tends to a parallel alignment with the substrate, once drying commences the particles that are on the surface tend to align to the moving boundary, and the particles in the bulk keep an orientation that produces the largest resistance, in this case horizontal. These observations justify the modelling of the sedimentation velocity and diffusion coefficient of the particles as a scalar quantity rather than a tensor, which greatly simplifies the adaptation of the simulation.

Concentration profiles were obtained from the simulation as a function of the dimensionless Péclet and sedimentation numbers. The model predicts that when the Pe_C is high and N_S is low the particles tend to accumulate at the top of the surface. If the Péclet and sedimentation numbers are low, the particles will mostly remain homogenously distributed, with low accumulation on the surface of the film due to an increase in the viscosity via solvent evaporation. Finally, if both Pe_C and N_S are high, the particles tend to sink to the bottom of the film, having a polymer rich layer on top of the film at the later stages of drying. The model is capable of predicting concentration distributions similar to the drying regimes of the particles. New drying regime maps were obtained by systematically changing N_S to obtain a value of Pe_C at which the concentration of the particles reaches 90% of the maximum packing concentration at the top or the bottom of the film. The shift of the regime borders as a function of the aspect ratio was investigated, showing a considerable movement from the spherical prediction. The shift was compared with the dependency of the initial concentration on the Evaporation-Diffusion regime borders, showing that changing the aspect ratio from $r_p = 0.1$ to $r_p = 0.03$ causes as much change as modifying the initial solvent concentration 5%, thus confirming that particle shape is an important parameter to be considered while predicting component distributions in dry films.

Drying experiments were conducted to verify the simulation results using the selected material system. Plates with an aspect ratio of $r_p = 0.10$ were chosen due to the confidence in the simulated. The 3-D Raman imaging tool showed a reconstructed depiction of the composite film morphology,

which allowed us to qualitatively identify a particle distribution in the dry film, which concorded with the average concentration of the particles along the film height. Most of the experiments with an experimentally identified Sedimentation regime were found to be accurately predicted by the drying regime maps. The Evaporation regime particle distribution experiments were located near the border between the Sedimentation and Evaporation zones, given by the critical value of the Sedimentation number N_S, implying that to achieve the desired particle concentration in a dry film the drying conditions must be set at least one order of magnitude away from the borders. Moreover, a Diffusion regime particle distribution was also identified in the Sedimentation part of the map, the mechanism for this inaccuracy was graphically summarized in Figure 4.6. It proposed that at this point the particles could move to the extremes of the film having a polymer rich layer in the middle, but due to the film shrinkage it appeared that the particles were evenly distributed in the film.

Limitations of the simulation model were also addressed, namely the effects of an infinite dilution $\phi_C \to 0$ and of infinitely flat particles with $r_p \to 0$. As previously stated, an increase in the solvent concentration will increase the diffusion driving forces expanding the Diffusion regime. On the other hand, a decrease in the aspect ratio will increase the viscous resistance and with it the particle mobility drops, thus the particles will accumulate faster at lower values of the evaporation rate, expanding the drying regime. For certain industrially relevant material systems both phenomena are present, that is the case for coating inks which require little amount of thin particles for their functionality. It is important for these systems to analyze which case is dominant. To that end composites made of graphene oxide flakes were investigated. It was found that the effect of an infinite dilution on the particle distribution in the dry film is stronger than the influence of the particle shape, making the particle distribution in the dry film homogeneous.

Adaptation of the model worked in a good manner to predict the particle distributions that are found for the spherical particle composites. Moreover, the generalization of the particle mobility as a function of the particle shape allowed automating the simulation for plate-like particles. One of the main challenges with the validation is the availability of plates with different particle sizes, without compromising the aspect ratio.

Nevertheless, the present work shows the importance of the particle shape while simulating component distributions and how the drying regime borders can be changed by using different particle geometries. Therefore, the particle shape plays an important role while designing drying processes.

5.2 Outlook

One question that has yet to be answered is the effect of time-dependent rotation on the particle distribution while settling or diffusing, as will be the case for rod-like particles. Rods do not align after a coating process[109] and tend to form vortices while falling in a viscous fluid[118,140,141]. This could affect the final structure of a composite film. As stated in this work, the position and orientation of the particles is crucial for the quality and functionality of composites, as in the production of composites made of carbon nanotubes[142], glass fibers[143] or gold particles[144,145].

It has been assumed that there is no particle size distribution, and the effects of the interactions between particles with different sizes are negligible. In the literature there are already some theoretical and experimental studies by Routh et al. to address this issue[146,147]. In these works, one more equation is added to describe the mass transfer in a system with a bimodal particle size distribution. Additionally, one other term needs to be added which can describe the stratification of the particles. Stratification is a spontaneous effect due to entropic contributions which causes particles to separate according to particle size[148]. This strategy could also be implemented for rod-like particles by adding a set of equations for each possible angle of orientation and terms to describe the turbulence generated by rotation. Unfortunately, the implementation of a time-dependent orientation and turbulence into the simulation model could increase the computation time considerably.

Other approaches made by Howard and Fortini simulate the bimodal case discretely [149–151], meaning that the dynamics of the particles are calculated individually. This approach has the advantage of requiring less physical information about the particles and the medium but requires longer computational times, depending on the number of particles. Equation (5.1) shows the simplified discrete simulation model. Here, instead

of modeling the concentration by means of conservation equations, the model opts for calculating the position of the particles using a force balance. The velocity vector of the ith particle $d\underline{r_i}/dt$ is a function of the substrate's surface energy and the distance of the particle to the substrate $\underline{f_i^W}$, the random movement given by the Brownian forces $\underline{f_i^B}$, the potential energy between the ith particle and the rest $\underline{f_i^P}$, and the buoyancy caused by the moving phase boundary due to drying and surface tension $\underline{f_i^E}$. Additionally, the drag caused by the fluid is included as a resistance.

$$\frac{d}{dt}\underline{r_i} = \frac{1}{\xi}\left(\underline{f_i^W} + \underline{f_i^B} + \underline{f_i^P} + \underline{f_i^E}\right) \qquad (5.1)$$

Figure 5.1 shows graphically how this method could be applied for a bimodal particle size distribution. Figure 5.2 shows a graphical representation of the driving forces according to their position along the film's height $h(t)$. Using a quasi-binary approach, the concentration of the polymer and moving phase boundary caused by solvent evaporation will be calculated using a polymer-related coordinate system, whereas the particle concentration will be obtained by computing the position of the particles. There are also extensive investigations using the discrete approach, but not many with either a polymer dissolved or a non-spherical geometry[149–154]. Nevertheless, adapting this approach for rod-like particles or polymer-bimodal particle composites could result in the best course of action to advance this work.[*]

---

[*] The proposed approached was included in a project proposal for the German Research Foundation (Deutsche Forschungsgemeinschaft, DFG)
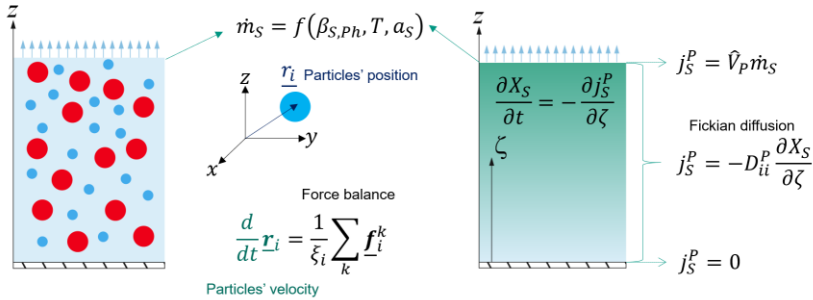
Figure 5.1. Graphical summary of a quasi-binary approach using discrete simulations for the particles and the polymer coordinate method for the polymer.
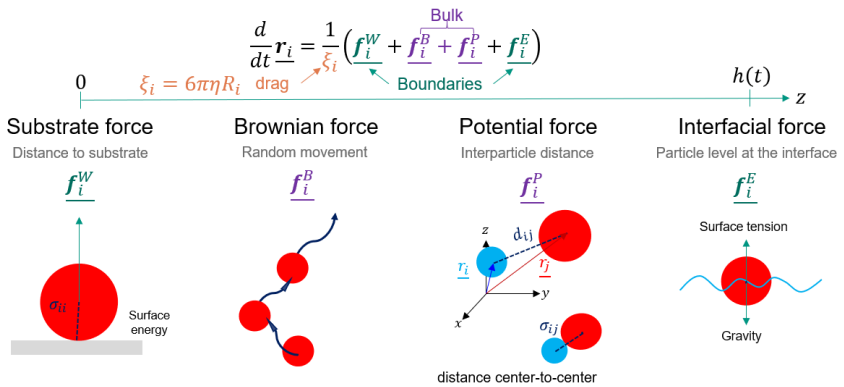
Figure 5.2. Graphical representation of the driving forces acting on the particle depending on its position along the film's height. Substrate energy and the interfacial force act on the systems borders, whereas the Brownian and potential forces have an effect in the bulk.

The numerical solution of differential equation (5.1) can be easily executed with the Euler method, because the equation is explicit. The only challenges are determination of the distance between all the particles for the potential force contribution. This can massively increase the computing times, and the appropriate time step. It is important to keep in mind that stratification as a function of the drying conditions summarized by the Péclet number can be nullified if the concentration of colloidal particles is high enough to undermine diffusion. In other words, the Péclet number

does not take into consideration the effects produced by the collective particles hindering their movement.

The experimental validation of rod particle simulations approach has fewer challenges than for the plate-like particles. PS particles are commercially available at different sizes and in combination with polyvinyl alcohol they produce a Raman active composite, thus being able to be investigated via spectroscopy. Additionally, PS spherical particles could be processed to synthesize prolate particles[155], extending the validation capabilities of the material system. Figure 5.3 shows a 3-D Raman image from a polymer-bimodal composite film made of PVA with a volume fraction in the dry film of $\phi_{P,dry} = 80$ % and PS particles at equal volume fractions of $\phi_{C,S,dry} = \phi_{C,L,dry} = 10$ %. The two different particles, with diameters of $3\ \mu m$ and $1 \mu m$, can be identified. This diagram corresponds to the top of a coating sample with a height of $14\ \mu m$. The sharpness of the image allows us to determine which particle size tends to go to the surface during drying, allowing us to experimentally determine stratification of the particles in the dry film.
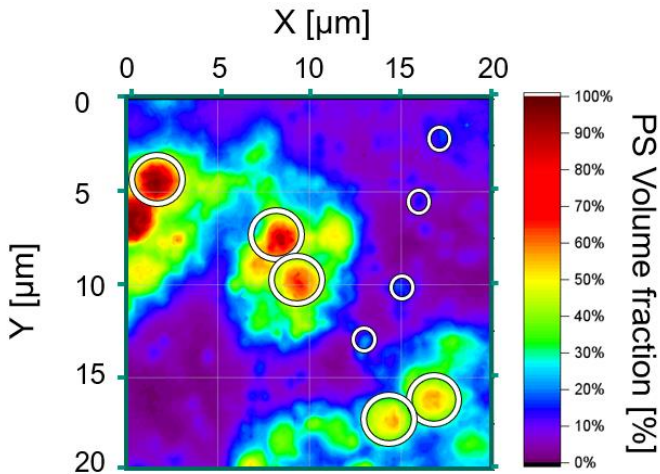
Figure 5.3. 3-D Raman imaging of a composite film made of PVA and PS dried at $30\ °C$ and $30\ Wm^{-2}K^{-1}$. Two different PS particles with different particle diameters of $3\ \mu m$ and $1\ \mu m$ were used. The image shows that Raman spectroscopy is a good tool to qualitatively determine the component distribution of different particle sizes and investigate the stratification of bimodal systems.

In the experimental work done by Routh et al.[147] the level of the stratification of colloidal particles in pure solvent was correlated with the drying conditions by means of the Péclet-Number, defined for bimodal particles as followed

$$Pe_{Bi} = \sqrt{Pe_L Pe_S} \qquad (5.2)$$

The finding showed that the concentration of the large particles at the top of the film was at its maximum when the Pe_{Bi} remained at the unity. However, industry relevant conditions are found to be at an order of magnitude of $O(Pe_{Bi}) = 10^3$ and in the presence of a polymer binder.

For colloidal particles with an average diameter lower than $< 1 \ \mu m$, it is not possible to qualitatively determine the position of the particles as shown in Figure 5.3, due to the spectrometer resolution ($2 - 3 \ \mu m$). Nevertheless, using particles with different chemical composition allows the ex situ identification of stratification in dry film. In a preliminary experiment PMMA and PS particles with an average diameter of $500 \ nm$ and $140 \ nm$ respectively we mixed with water and PVA, coated and dried at different heat transfer coefficients $\alpha = 30, 40, 50 \ W \ m^{-2} \ K^{-1}$. The concentration profiles of each particle system are plotted in Figure 5.4. At 30 and 40 $W \ m^2 \ K^{-1}$ it can be observed that the small and large particles are evenly distributed along the film height showing almost no change in the concentration. Nevertheless, at $50 \ W \ m^2 \ K^{-1}$ an accumulation of the large particles can be seen, even though the Péclet number exceeds unity, $Pe_{Bi}(\alpha = 50 \ W \ m^2 \ K^{-1}) = 7353$.

These preliminary results show the importance of the influence of the polymer binder, which affects the mobility of the particles during drying, hindering their movement as the viscosity of the medium increases.
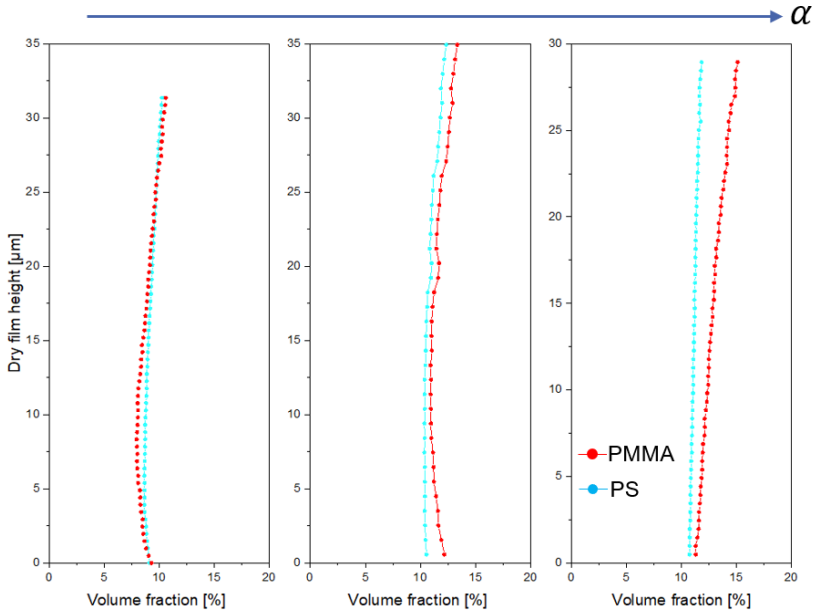
Figure 5.4. Concentration of the particles as a function of the film height, the films were dried by three different HTC ($\alpha = 30, 40, 50\ W\ m^{-2}K^{-1}$). The small PS particles are plotted in blue, and the large PMMA particles are plotted in red. On the far-right diagram a concentration gradient for the large particles can be observed.

6   References

[1] G. Keledi, J. Hári, B. Pukánszky, Polymer nanocomposites: structure, interaction, and functionality, *Nanoscale* **2012**, *4*, 1919.

[2] J. Kumberg, M. Müller, R. Diehm, S. Spiegel, C. Wachsmann, W. Bauer, P. Scharfer, W. Schabel, Drying of Lithium-Ion Battery Anodes for Use in High-Energy Cells: Influence of Electrode Thickness on Drying Time, Adhesion, and Crack Formation, *Energy Technol.* **2019**, *7*, 1900722.

[3] M. Müller, L. Pfaffmann, S. Jaiser, M. Baunach, V. Trouillet, F. Scheiba, P. Scharfer, W. Schabel, W. Bauer, Investigation of binder distribution in graphite anodes for lithium-ion batteries, *Journal of power sources* **2017**, *340*, 1.

[4] N. A. Luechinger, E. K. Athanassiou, W. J. Stark, Graphene-stabilized copper nanoparticles as an air-stable substitute for silver and gold in low-cost ink-jet printable electronics, *Nanotechnology* **2008**, *19*, 445201.

[5] L. Merklein, M. Mink, D. Kourkoulos, B. Ulber, S. M. Raupp, K. Meerholz, P. Scharfer, W. Schabel, Multilayer OLEDs with four slot die-coated layers, *J Coat Technol Res* **2019**, *16*, 1643.

[6] P. Staiti, F. Lufrano, Nafion® and Fumapem® polymer electrolytes for the development of advanced solid-state supercapacitors, *Electrochimica Acta* **2016**, *206*, 432.

[7] D. Rivin, C. E. Kendrick, P. W. Gibson, N. S. Schneider, Solubility and transport behavior of water and alcohols in Nafion™ **2001**.

[8] A.-L. Riegel, N. Borzenkova, V. Haas, P. Scharfer, W. Schabel, Activity determination of FAD-dependent glucose dehydrogenase immobilized in PEDOT: PSS-PVA composite films for biosensor applications, *Eng. Life Sci.* **2016**, *16*, 577.

[9] S. Srivastava, J. L. Schaefer, Z. Yang, Z. Tu, L. A. Archer, 25th anniversary article: polymer-particle composites: phase stability and applications in electrochemical energy storage, *Advanced Materials* **2014**, *26*, 201.

[10] A. B. Norton, R. D. Hancocks, L. M. Grover, Poly (vinyl alcohol) modification of low acyl gellan hydrogels for applications in tissue regeneration, *Food Hydrocolloids* **2014**, *42*, 373.

[11] B. Sadeghi, F. S. Garmaroudi, M. Hashemi, H. R. Nezhad, A. Nasrollahi, S. Ardalan, S. Ardalan, Comparison of the anti-bacterial activity on the nanosilver shapes: Nanoparticles, nanorods and nanoplates, *Advanced Powder Technology* **2012**, *23*, 22.

[12] Y. Ren, L. Zhang, G. Xie, Z. Li, H. Chen, H. Gong, W. Xu, D. Guo, J. Luo, A review on tribology of polymer composite coatings, *Friction* **2021**, *9*, 429.

[13] S. Sinha Ray, M. Okamoto, Polymer/layered silicate nanocomposites: a review from preparation to processing, *Progress in Polymer Science* **2003**, *28*, 1539.

[14] G. Liu, W. Jin, N. Xu, Graphene-based membranes, *Chemical Society reviews* **2015**, *44*, 5016.

[15] A. C. Ferrari, F. Bonaccorso, V. Fal'ko, K. S. Novoselov, S. Roche, P. Bøggild, S. Borini, F. H. L. Koppens, V. Palermo, N. Pugno, J. A. Garrido, R. Sordan, A. Bianco, L. Ballerini, M. Prato, E. Lidorikis, J. Kivioja, C. Marinelli, T. Ryhänen, A. Morpurgo, J. N. Coleman, V. Nicolosi, L. Colombo, A. Fert, M. Garcia-Hernandez, A. Bachtold, G. F. Schneider, F. Guinea, C. Dekker, M. Barbone, Z. Sun, C. Galiotis, A. N. Grigorenko, G. Konstantatos, A. Kis, M. Katsnelson, L. Vandersypen, A. Loiseau, V. Morandi, D. Neumaier, E. Treossi, V. Pellegrini, M. Polini, A. Tredicucci, G. M. Williams, B. H. Hong, J.-H. Ahn, J. M. Kim, H. Zirath, B. J. van Wees, H. van der Zant, L. Occhipinti, A. Di Matteo, I. A. Kinloch, T. Seyller, E. Quesnel, X. Feng, K. Teo, N. Rupesinghe, P. Hakonen, S. R. T. Neil, Q. Tannock, T. Löfwander, J. Kinaret, Science and technology roadmap for graphene, related two-dimensional crystals, and hybrid systems, *Nanoscale* **2015**, *7*, 4598.

[16] K. S. Novoselov, A. K. Geim, S. V. Morozov, D. Jiang, Y. Zhang, S. V. Dubonos, I. V. Grigorieva, A. A. Firsov, Electric field effect in atomically thin carbon films, *Science (New York, N.Y.)* **2004**, *306*, 666.

[17] M. M. Gudarzi, F. Sharif, Molecular level dispersion of graphene in polymer matrices using colloidal polymer and graphene, *Journal of colloid and interface science* **2012**, *366*, 44.

[18] Y. Dan, Y. Lu, N. J. Kybert, Z. Luo, A. T. C. Johnson, Intrinsic response of graphene vapor sensors, *Nano letters* **2009**, *9*, 1472.

[19] K. S. Kim, Y. Zhao, H. Jang, S. Y. Lee, J. M. Kim, K. S. Kim, J.-H. Ahn, P. Kim, J.-Y. Choi, B. H. Hong, Large-scale pattern growth of graphene films for stretchable transparent electrodes, *Nature* **2009**, *457*, 706.

[20] R. P. Pandey, G. Shukla, M. Manohar, V. K. Shahi, Graphene oxide based nanohybrid proton exchange membranes for fuel cell applications: An overview, *Advances in Colloid and Interface Science* **2017**, *240*, 15.

[21] D. Wang, D. Choi, J. Li, Z. Yang, Z. Nie, R. Kou, D. Hu, C. Wang, L. V. Saraf, J. Zhang, I. A. Aksay, J. Liu, Self-assembled TiO2-graphene hybrid nanostructures for enhanced Li-ion insertion, *ACS nano* **2009**, *3*, 907.

[22] C.-H. Tsou, Q.-F. An, S.-C. Lo, M. de Guzman, W.-S. Hung, C.-C. Hu, K.-R. Lee, J.-Y. Lai, Effect of microstructure of graphene oxide fabricated through different self-assembly techniques on 1-butanol dehydration, *Journal of Membrane Science* **2015**, *477*, 93.

[23] M. Wei, M. Jiang, X. Liu, M. Wang, S. Mu, Graphene-doped electrospun nanofiber membrane electrodes and proton exchange membrane fuel cell performance, *Journal of power sources* **2016**, *327*, 384.

[24] Z. Liu, K. Parvez, R. Li, R. Dong, X. Feng, K. Müllen, Transparent conductive electrodes from graphene/PEDOT:PSS hybrid inks for ultrathin organic photodetectors, *Advanced Materials* **2015**, *27*, 669.

[25] M. Alexandre, P. Dubois, Polymer-layered silicate nanocomposites: preparation, properties and uses of a new class of materials, *Materials Science and Engineering: R: Reports* **2000**, *28*, 1.

[26] V. Mittal, Polymer Layered Silicate Nanocomposites: A Review, *Materials* **2009**, *2*, 992.

[27] P. Cassagnau, Melt rheology of organoclay and fumed silica nanocomposites, *Polymer* **2008**, *49*, 2183.

[28] W. R. Caseri, Nanocomposites of polymers and inorganic particles: preparation, structure and properties, *Materials Science and Technology* **2006**, *22*, 807.

[29] L. Wang, F. Gao, J. Xu, K. Zhang, J. Kong, M. Reece, H. Yan, Enhanced dielectric tunability and energy storage properties of plate-like Ba0.6Sr0.4TiO3/poly(vinylidene fluoride) composites through

texture arrangement, *Composites Science and Technology* **2018**, *158*, 112.

[30] N. S. Stoloff, An overview of powder processing of silicides and their composites, *Materials Science and Engineering: A* **1999**, *261*, 169.

[31] R. K. Nishihora, P. L. Rachadel, M. G. N. Quadri, D. Hotza, Manufacturing porous ceramic materials by tape casting—A review, *Journal of the European Ceramic Society* **2018**, *38*, 988.

[32] J. Pan, F. Ai, P. Shao, H. Chen, H. Gao, Development of polyvinyl alcohol/β-cyclodextrin antimicrobial nanofibers for fresh mushroom packaging, *Food Chemistry* **2019**, *300*, 125249.

[33] M. Léang, F. Giorgiutti-Dauphiné, L.-T. Lee, L. Pauchard, Crack opening: from colloidal systems to paintings, *Soft matter* **2017**, *13*, 5802.

[34] S. Baesch, D. Siebel, B. Schmidt-Hansberg, C. Eichholz, M. Gerst, P. Scharfer, W. Schabel, Comparison of Surfactant Distributions in Pressure-Sensitive Adhesive Films Dried from Dispersion under Lab-Scale and Industrial Drying Conditions, *ACS applied materials & interfaces* **2016**, *8*, 8118.

[35] R. B. Bird, C. F. Curtiss, R. C. Armstrong, O. Hassager, Dynamics of Polymeric Liquids, Volume 2: Kinetic Theory, Wiley **1987**.

[36] H. C. Öttinger, Generalized Zimm model for dilute polymer solutions under theta conditions, *The Journal of Chemical Physics* **1987**, *86*, 3731.

[37] R. B. Bird, W. E. Stewart, E. N. Lightfoot, Transport phenomena, Wiley, New York **1960**.

[38] J. S. Vrentas, J. L. Duda, Diffusion in polymer–solvent systems. II. A predictive theory for the dependence of diffusion coefficients on temperature, concentration, and molecular weight, *J. Polym. Sci. Polym. Phys. Ed.* **1977**, *15*, 417.

[39] S. Kachel, P. Scharfer, W. Schabel, Measurements and predictive modeling of water diffusion coefficients in bovine serum albumin/polymer blends for biosensors, *J. Appl. Polym. Sci.* **2017**, *134*, 45368.

[40] M. Räderer, A. Besson, K. Sommer, A thin film dryer approach for the determination of water diffusion coefficients in viscous products, *Chemical Engineering Journal* **2002**, *86*, 185.

[41] D. Siebel, P. Scharfer, W. Schabel, Determination of Concentration-Dependent Diffusion Coefficients in Polymer–Solvent Systems:

Analysis of Concentration Profiles Measured by Raman Spectroscopy during Single Drying Experiments Excluding Boundary Conditions and Phase Equilibrium, *Macromolecules* **2015**, *48*, 8608.

[42] W. Schabel, Inverse Mikro-Raman-Spektroskopie - Eine neue Messmethode zur Untersuchung lokaler Stofftransportvorgänge in dünnen Filmen, Folien und Membranen, *Chemie Ingenieur Technik* **2005**, *77*, 1915.

[43] W. Schabel, P. Scharfer, M. Müller, I. Ludwig, M. Kind, Messung und Simulation von Konzentrationsprofilen bei der Trocknung binärer Polymerlösungen, *Chemie Ingenieur Technik* **2003**, *75*, 1336.

[44] P. Scharfer, W. Schabel, M. Kind, Modelling of alcohol and water diffusion in fuel cell membranes--Experimental validation by means of in situ Raman spectroscopy, *Chemical engineering science* **2008**, *63*, 4676.

[45] L. Onsager, Reciprocal Relations in Irreversible Processes. I, *Phys. Rev.* **1931**, *37*, 405.

[46] S. M. Raupp, P. G. Kitz, D. K. Siebel, A. Wunsch, L. Merklein, P. Scharfer, W. Schabel, Modeling of interdiffusion in poly(vinyl acetate)–poly(methyl methacrylate)–toluene multicomponent systems, *Journal of Applied Polymer Science* **2019**, *136*, 47092.

[47] D. Siebel, P. Scharfer, W. Schabel, Prediction of diffusion in a ternary solvent-solvent-polymer blend by means of binary diffusion data: Comparison of experimental data and simulative results, *J. Appl. Polym. Sci.* **2016**, *133*.

[48] E.-U. Schlünder, Einführung in die Stoffübertragung, Thieme, Stuttgart **1984**.

[49] Verein Deutscher Ingenieure, VDI-Gesellschaft Verfahrenstechnik und Chemieingenieurwesen, VDI-Wärmeatlas, Springer Vieweg, Berlin **2013**.

[50] R. Saure, G. R. Wagner, E.-U. Schlünder, Drying of solvent-borne polymeric coatings: I. Modeling the drying process, *Surface and Coatings Technology* **1998**, *99*, 253.

[51] L. Merklein, J. C. Eser, T. Börnhorst, N. Könnecke, P. Scharfer, W. Schabel, Different dominating mass transport mechanisms for drying and sorption of toluene-PMMA films – Visualized with Raman spectroscopy, *Polymer* **2021**, *222*, 123640.

[52] P. Scharfer, W. Schabel, M. Kind, Mass transport measurements in membranes by means of in situ Raman spectroscopy—First results of methanol and water profiles in fuel cell membranes, *Journal of Membrane Science* **2007**, *303*, 37.

[53] S. Jeck, P. Scharfer, M. Kind, Absence of Schroeder's paradox: Experimental evidence for water-swollen Nafion® membranes, *Journal of Membrane Science* **2011**, *373*, 74.

[54] V.-A. Gracia-Medrano-Bravo, L. Merklein, N. Oberle, M. Batora, P. Scharfer, W. Schabel, Determination of Binary Interaction Parameters for Ternary Polymer–Polymer–Solvent Systems Using Raman Spectroscopy, *Adv. Mater. Technol.* **2021**, *6*, 2000149.

[55] A. F. Routh, W. B. Zimmerman, Distribution of particles during solvent evaporation from films, *Chemical engineering science* **2004**, *59*, 2961.

[56] A. F. Routh, W. B. Russel, Horizontal drying fronts during solvent evaporation from latex films, *AIChE J.* **1998**, *44*, 2088.

[57] I. Ludwig, W. Schabel, M. Kind, J.-C. Castaing, P. Ferlin, Drying and film formation of industrial waterborne latices, *AIChE J.* **2007**, *53*, 549.

[58] K. E. Davis, W. B. Russel, An asymptotic description of transient settling and ultrafiltration of colloidal dispersions, *Physics of Fluids A: Fluid Dynamics* **1989**, *1*, 82.

[59] G. K. Batchelor, Brownian diffusion of particles with hydrodynamic interaction, *Journal of Fluid Mechanics* **1976**, *74*, 1.

[60] W. P. Lee, V. R. Gundabala, B. S. Akpa, M. L. Johns, C. Jeynes, A. F. Routh, Distribution of surfactants in latex films: a Rutherford Backscattering study, *Langmuir* **2006**, *22*, 5314.

[61] A. F. Routh, W. B. Russel, A Process Model for Latex Film Formation: Limiting Regimes for Individual Driving Forces, *Langmuir* **1999**, *15*, 7762.

[62] J. W. Vanderhoff, E. B. Bradford, W. K. Carrington, The transport of water through latex films, *J. polym. sci., C Polym. symp.* **1973**, *41*, 155.

[63] A. F. Routh, W. B. Russel, Deformation Mechanisms during Latex Film Formation: Experimental Evidence, *Industrial & Engineering Chemistry Research* **2001**, *40*, 4302.

[64] E. R. Dufresne, E. I. Corwin, N. A. Greenblatt, J. Ashmore, D. Y. Wang, A. D. Dinsmore, J. X. Cheng, X. S. Xie, J. W. Hutchinson, D. A. Weitz, Flow and fracture in drying nanoparticle suspensions, *Physical review letters* **2003**, *91*, 224501.

[65] A. F. Routh, Fundamentals of Latex Film Formation: *Processes and Properties*, Springer Netherlands, Dordrecht **2010**.

[66] C. M. Cardinal, Y. D. Jung, K. H. Ahn, L. F. Francis, Drying regime maps for particulate coatings, *AIChE Journal* **2010**, *56*, 2769.

[67] S. Baesch, P. Scharfer, W. Schabel, L. Francis, Influence of the drying conditions on the particle distribution in particle-filled polymer films: Predictive simulation of the particle distribution during drying, *Journal of composite materials* **2017**, *51*, 3391.

[68] S. Baesch, K. Price, P. Scharfer, L. Francis, W. Schabel, Influence of the drying conditions on the particle distribution in particle filled polymer films: Experimental validation of predictive drying regime maps, *Chemical Engineering and Processing - Process Intensification* **2018**, *123*, 138.

[69] V.-A. Gracia-Medrano-Bravo, J. Gröne, S. Baesch, P. Scharfer, W. Schabel, Influence of Particle Shape on the Drying Regime Maps for Platelike Particle-Polymer Composites, *Langmuir* **2020**, *36*, 6245.

[70] S. Jaiser, J. Kumberg, J. Klaver, J. L. Urai, W. Schabel, J. Schmatz, P. Scharfer, Microstructure formation of lithium-ion battery electrodes during drying – An ex-situ study using cryogenic broad ion beam slope-cutting and scanning electron microscopy (Cryo-BIB-SEM), *Journal of power sources* **2017**, *345*, 97.

[71] F. Buss, C. C. Roberts, K. S. Crawford, K. Peters, L. F. Francis, Effect of soluble polymer binder on particle distribution in a drying particulate coating, *Journal of colloid and interface science* **2011**, *359*, 112.

[72] M. Bercea, S. Morariu, D. Rusu, In situgelation of aqueous solutions of entangled poly(vinyl alcohol), *Soft matter* **2013**, *9*, 1244.

[73] S. Baesch, Influence of the drying conditions on the particle distribution in polymer matrix composites drying regime maps - approach for facilitated industrial applicability **2017**.

[74] P. M. Chaikin, A. Donev, W. Man, F. H. Stillinger, S. Torquato, Some Observations on the Random Packing of Hard Ellipsoids, *Industrial & Engineering Chemistry Research* **2006**, *45*, 6960.

[75] N. I. Lebovka, M. O. Tatochenko, N. V. Vygornitskii, Y. Y. Tarasevich, Paris car parking problem for partially oriented discorectangles on a line, *Physical review. E* **2020**, *102*, 12128.

[76] R. Aris, Vectors, tensors, and the basic equations of fluid mechanics, Dover Publications, New York **1989**.

[77] X. Tian, M. E. Itkis, E. B. Bekyarova, R. C. Haddon, Anisotropic Thermal and Electrical Properties of Thin Thermal Interface Layers of Graphite Nanoplatelet-Based Composites, *Sci Rep* **2013**, *3*, 1.

[78] J. G. Pharoah, K. Karan, W. Sun, On effective transport coefficients in PEM fuel cell electrodes: Anisotropy of the porous transport layers, *Journal of power sources* **2006**, *161*, 214.

[79] D. Le Bihan, J. F. Mangin, C. Poupon, C. A. Clark, S. Pappata, N. Molko, H. Chabriat, Diffusion tensor imaging: concepts and applications, *Journal of magnetic resonance imaging JMRI* **2001**, *13*, 534.

[80] J. C. Eser, B. Deichmann, T. Wirsching, P. G. Weidler, P. Scharfer, W. Schabel, Hysteresis Behavior in the Sorption Equilibrium of Water in Anodes for Li-Ion Batteries, *Langmuir the ACS journal of surfaces and colloids* **2020**, *36*, 6193.

[81] J. C. Eser, T. Wirsching, P. G. Weidler, A. Altvater, T. Börnhorst, J. Kumberg, G. Schöne, M. Müller, P. Scharfer, W. Schabel, Moisture Adsorption Behavior in Anodes for Li-Ion Batteries, *Energy Technology* **2020**, *8*, 1801162.

[82] P. Zehner, E. U. Schlünder, Wärmeleitfähigkeit von Schüttungen bei mäßigen Temperaturen, *Chemie Ingenieur Technik* **1970**, *42*, 933.

[83] R. Vasanthi, S. Bhattacharyya, B. Bagchi, Anisotropic diffusion of spheroids in liquids: Slow orientational relaxation of the oblates, *The Journal of Chemical Physics* **2002**, *116*, 1092.

[84] S. Jeck, P. Scharfer, W. Schabel, M. Kind, Water sorption in poly(vinyl alcohol) membranes: An experimental and numerical study of solvent diffusion in a crosslinked polymer, *Chemical Engineering and Processing - Process Intensification* **2011**, *50*, 543.

[85] S. Kachel, P. Scharfer, W. Schabel, Sorption isotherms of mixtures of polymers, proteins and electrolytes—Measurement data and model predictions, *Chem Eng Process* **2013**, *68*, 45.

[86] F. M. van der Kooij, E. S. Boek, A. P. Philipse, Rheology of Dilute Suspensions of Hard Platelike Colloids, *Journal of colloid and interface science* **2001**, *235*, 344.

[87] S. Mueller, E. W. Llewellin, H. M. Mader, The effect of particle shape on suspension viscosity and implications for magmatic flows, *Geophys. Res. Lett.* **2011**, *38*, n/a-n/a.

[88] W. B. Russel, D. A. Saville, W. R. Schowalter, Colloidal dispersions, Cambridge Univ. Press, Cambridge **1991**.

[89] S. Spiegel, T. Heckmann, A. Altvater, R. Diehm, P. Scharfer, W. Schabel, Investigation of edge formation during the coating process of Li-ion battery electrodes, *J Coat Technol Res* **2022**, *19*, 121.

[90] A. Einstein, A new determination of molecular dimensions, *Ann. Phys.* **1906**, *19*, 289.

[91] G. K. Batchelor, The effect of Brownian motion on the bulk stress in a suspension of spherical particles, *J. Fluid Mech.* **1977**, *83*, 97.

[92] H. Eilers, Die Viskosität von Emulsionen hochviskoser Stoffe als Funktion der Konzentration, *Colloid Polym Sci* **1941**, *97*, 313.

[93] M. Mooney, The viscosity of a concentrated suspension of spherical particles, *Journal of Colloid Science* **1951**, *6*, 162.

[94] I. M. Krieger, T. J. Dougherty, A Mechanism for Non-Newtonian Flow in Suspensions of Rigid Spheres, *Transactions of the Society of Rheology* **1959**, *3*, 137.

[95] W. Schabel, Trocknung von Polymerfilmen: *Messung von Konzentrationsprofilen mit der Inversen-Mikro-Raman-Spektroskopie*, Shaker, Aachen **2004**.

[96] B. Schmidt-Hansberg, M. Baunach, J. Krenn, S. Walheim, U. Lemmer, P. Scharfer, W. Schabel, Spatially resolved drying kinetics of multi-component solution cast films for organic electronics, *Chemical Engineering and Processing: Process Intensification* **2011**, 50, 509.

[97] T. A. Ameel, Average effects of forced convection over a flat plate with an unheated starting length, *International Communications in Heat and Mass Transfer* **1997**, *24*, 1113.

[98] Cavadini, P., W. Schabel, P. Scharfer und L. Wengeler, Device for transferring heat or mass, comprising hexagonal jet nozzles, and method for treating surface layers.

[99] F. Perrin, Mouvement brownien d'un ellipsoide - I. Dispersion diélectrique pour des molécules ellipsoidales, *Journal de Physique et le Radium* **1934**, *5*, 497.

[100] H. Brenner, Rheology of a dilute suspension of axisymmetric Brownian particles, *Int. J. Multiph.* **1974**, *1*, 195.

[101] F. M. van der Kooij, A. P. Philipse, J. K. G. Dhont, Sedimentation and Diffusion in Suspensions of Sterically Stabilized Colloidal Platelets, *Langmuir* **2000**, *16*, 5317.

[102] Y. Han, A. M. Alsayed, M. Nobili, J. Zhang, T. C. Lubensky, A. G. Yodh, Brownian motion of an ellipsoid, *Science (New York, N.Y.)* **2006**, *314*, 626.

[103] P. S. Hubbard, Rotational Brownian Motion, *Phys. Rev. A* **1972**, *6*, 2421.

[104] G. L. Hunter, K. V. Edmond, M. T. Elsesser, E. R. Weeks, Tracking rotational diffusion of colloidal clusters, *Opt. Express, OE* **2011**, *19*, 17189.

[105] C.-M. Hu, R. Zwanzig, Rotational friction coefficients for spheroids with the slipping boundary condition, *The Journal of Chemical Physics* **1974**, *60*, 4354.

[106] J. K. G. Dhont, An introduction to dynamics of colloids, Elsevier, Amsterdam **2003**.

[107] F. P. Bretherton, The motion of rigid particles in a shear flow at low Reynolds number, *J. Fluid Mech.* **1962**, *14*, 284.

[108] S. Kim, S. J. Karrila, H. Brenner, Microhydrodynamics: Principles and Selected Applications, Elsevier Science, Burlington **2013**.

[109] G. B. Jeffery, The Motion of Ellipsoidal Particles Immersed in a Viscous Fluid, *Proceedings of the Royal Society A: Mathematical, Physical and Engineering Sciences* **1922**, *102*, 161.

[110] C. Yang, W. H. Smyrl, E. L. Cussler, Flake alignment in composite coatings, *Journal of Membrane Science* **2004**, *231*, 1.

[111] L.-P. Sung, M. E. Nadal, M. E. McKnight, E. Marx, B. Laurenti, Optical reflectance of metallic coatings: Effect of aluminum flake orientation, *Journal of Coatings Technology* **2002**, *74*, 55.

[112] E. Bertevas, X. Fan, R. I. Tanner, Simulation of the rheological properties of suspensions of oblate spheroidal particles in a Newtonian fluid, *Rheologica Acta* **2010**, *49*, 53.

[113] D. Z. Gunes, R. Scirocco, J. Mewis, J. Vermant, Flow-induced orientation of non-spherical particles: Effect of aspect ratio and medium rheology, *Journal of Non-Newtonian Fluid Mechanics* **2008**, *155*, 39.

[114] E. Kirchner, Film shrinkage and flake orientation, *Progress in Organic Coatings* **2009**, *65*, 333.

[115] J. D. Posey-Dowty, K. S. Seo, K. R. Walker, A. K. Wilson, Carboxymethylcellulose acetate butyrate in water-based automotive paints, *Surface Coatings International Part B: Coatings Transactions* **2002**, *85*, 203.

[116] W. R. WHALLEY, C. E. MULLINS, Oriented and random sedimentation of plate-like clay particles in high centrifugal fields, *Journal of Soil Science* **1992**, *43*, 531.

[117] M. N. Ardekani, P. Costa, W. P. Breugem, L. Brandt, Numerical study of the sedimentation of spheroidal particles, *International Journal of Multiphase Flow* **2016**, *87*, 16.

[118] M. Hnatow, R. Pfeffer, J. Happel, Sedimentation of two prolate spheroids in close proximity, *Can. J. Chem. Eng.* **1969**, *47*, 12.

[119] H. Huang, X. Yang, X. Lu, Sedimentation of an ellipsoidal particle in narrow tubes, *Phys. Fluids* **2014**, *26*, 53302.

[120] A. S. Dogonchi, M. Hatami, K. Hosseinzadeh, G. Domairry, Non-spherical particles sedimentation in an incompressible Newtonian medium by Padé approximation, *Powder Technology* **2015**, *278*, 248.

[121] G. K. Batchelor, Sedimentation in a dilute dispersion of spheres, *J. Fluid Mech.* **1972**, *52*, 245.

[122] G. K. Batchelor, Sedimentation in a dilute polydisperse system of interacting spheres. Part 1. General theory, *J. Fluid Mech.* **1982**, *119*, 379.

[123] R. Buscall, J. W. Goodwin, R. H. Ottewill, T. Tadros, The settling of particles through Newtonian and non-Newtonian media, *Journal of colloid and interface science* **1982**, *85*, 78.

[124] de Kruif C.G., Jansen J.W., Vrij A., A sterically stabilized silica colloid as a model supramolecular fluid **1987**.

[125] J. Jansen, C. de Kruif, A. Vrij, Attractions in sterically stabilized silica dispersions, *Journal of colloid and interface science* **1986**, *114*, 501.

[126] P. He, A. F. Mejia, Z. Cheng, D. Sun, H.-J. Sue, D. S. Dinair, M. Marquez, Hindrance function for sedimentation and creaming of colloidal disks, *Physical review. E, Statistical, nonlinear, and soft matter physics* **2010**, *81*, 26310.

[127] J. D. Weeks, D. Chandler, H. C. Andersen, Role of Repulsive Forces in Determining the Equilibrium Structure of Simple Liquids, *The Journal of Chemical Physics* **1971**, *54*, 5237.

[128] V.-A. Gracia-Medrano-Bravo, P. Scharfer, W. Schabel, On the drying kinetics of non-spherical particle-filled polymer films: A numerical study, *AIChE Journal* **2022**, *68*.

[129] J. Crank, The mathematics of diffusion, Oxford Univ. Press, Oxford **1975**.

[130] J. Crank, The Influence of Concentration-Dependent Diffusion on Rate of Evaporation, *Proc. Phys. Soc. B* **1950**, *63*, 484.

[131] S. J. Ahn, K. H. Ahn, S. J. Lee, Film squeezing process for generating oblate spheroidal particles with high yield and uniform sizes, *Colloid Polym Sci* **2016**, *294*, 859.

[132] L. Onsager, THE EFFECTS OF SHAPE ON THE INTERACTION OF COLLOIDAL PARTICLES, *Annals of the New York Academy of Sciences* **1949**, *51*, 627.

[133] S. Prager, Diffusion and viscous flow in concentrated suspensions, *Physica* **1963**, *29*, 129.

[134] R. R. Nair, H. A. Wu, P. N. Jayaram, I. V. Grigorieva, A. K. Geim, Unimpeded permeation of water through helium-leak-tight graphene-based membranes, *Science (New York, N.Y.)* **2012**, *335*, 442.

[135] S. C. O'Hern, M. S. H. Boutilier, J.-C. Idrobo, Y. Song, J. Kong, T. Laoui, M. Atieh, R. Karnik, Selective ionic transport through tunable subnanometer pores in single-layer graphene membranes, *Nano letters* **2014**, *14*, 1234.

[136] F. Tuinstra, J. L. Koenig, Raman Spectrum of Graphite, *The Journal of Chemical Physics* **1970**, *53*, 1126.

[137] A. C. Ferrari, J. C. Meyer, V. Scardaci, C. Casiraghi, M. Lazzeri, F. Mauri, S. Piscanec, D. Jiang, K. S. Novoselov, S. Roth, A. K. Geim, Raman spectrum of graphene and graphene layers, *Physical review letters* **2006**, *97*, 187401.

[138] A. A. Muhsan, K. Lafdi, Numerical study of the electrochemical exfoliation of graphite, *SN Appl. Sci.* **2019**, *1*, 1.

[139] M. S. Dresselhaus, A. Jorio, A. G. Souza Filho, R. Saito, Defect characterization in graphene and carbon nanotubes using Raman

spectroscopy, *Philosophical transactions. Series A, Mathematical, physical, and engineering sciences* **2010**, *368*, 5355.

[140] M. N. Niazi Ardekani, P. Costa, W. P. Breugem, L. Brandt, Numerical study of the sedimentation of spheroidal particles, *Int. J. Multiph.* **2016**, *87*, 16.

[141] R. H. Davis, Sedimentation of axisymmetric particles in shear flows, *Phys Fluid Fluid Dynam* **1991**, *3*, 2051.

[142] X. Zeng, X. Xu, P. M. Shenai, E. Kovalev, C. Baudot, N. Mathews, Y. Zhao, Characteristics of the Electrical Percolation in Carbon Nanotubes/Polymer Nanocomposites, *J. Phys. Chem. C* **2011**, *115*, 21685.

[143] B. A. Housen, C. Richter, B. A. van der Pluijm, Composite magnetic anisotropy fabrics: experiments, numerical models and implications for the quantification of rock fabrics, *Tectonophysics* **1993**, *220*, 1.

[144] S. I. Park, H.-M. Song, Synthesis of Prolate-Shaped Au Nanoparticles and Au Nanoprisms and Study of Catalytic Reduction Reactions of 4-Nitrophenol, *ACS Omega* **2019**, *4*, 7874.

[145] J. Pérez-Juste, B. Rodríguez-González, P. Mulvaney, L. M. Liz-Marzán, Optical Control and Patterning of Gold-Nanorod-Poly(vinyl alcohol) Nanocomposite Films, *Adv. Funct. Mater.* **2005**, *15*, 1065.

[146] A. K. Atmuri, S. R. Bhatia, A. F. Routh, Autostratification in drying colloidal dispersions: effect of particle interactions, *Langmuir the ACS journal of surfaces and colloids* **2012**, *28*, 2652.

[147] R. E. Trueman, E. Lago Domingues, S. N. Emmett, M. W. Murray, J. L. Keddie, A. F. Routh, Autostratification in drying colloidal dispersions: experimental investigations, *Langmuir the ACS journal of surfaces and colloids* **2012**, *28*, 3420.

[148] A. Beaugendre, S. Degoutin, S. Bellayer, C. Pierlot, S. Duquesne, M. Casetta, M. Jimenez, Self-stratifying coatings: A review, *Progress in Organic Coatings* **2017**, *110*, 210.

[149] A. Fortini, I. Martín-Fabiani, J. L. de La Haye, P.-Y. Dugas, M. Lansalot, F. D'Agosto, E. Bourgeat-Lami, J. L. Keddie, R. P. Sear, Publisher's Note: Dynamic Stratification in Drying Films of Colloidal Mixtures Phys. Rev. Lett. 116, 118301 (2016), *Physical review letters* **2016**, *116*, 229902.

[150] M. P. Howard, A. Nikoubashman, A. Z. Panagiotopoulos, Stratification Dynamics in Drying Colloidal Mixtures, *Langmuir the ACS journal of surfaces and colloids* **2017**, *33*, 3685.

[151] M. P. Howard, A. Nikoubashman, A. Z. Panagiotopoulos, Stratification in Drying Polymer-Polymer and Colloid-Polymer Mixtures, *Langmuir the ACS journal of surfaces and colloids* **2017**, *33*, 11390.

[152] J. H. Jeong, Y. K. Lee, K. H. Ahn, Stratification Mechanism in the Bidisperse Colloidal Film Drying Process: Evolution and Decomposition of Normal Stress Correlated with Microstructure, *Langmuir the ACS journal of surfaces and colloids* **2021**, *37*, 13712.

[153] C. Chang, R. L. Powell, Self-diffusion of bimodal suspensions of hydrodynamically interacting spherical particles in shearing flow, *J. Fluid Mech.* **1994**, *281*, 51.

[154] J. F. Favier, M. H. Abbaspour-Fard, M. Kremmer, A. O. Raji, Shape representation of axi-symmetrical, non-spherical particles in discrete element simulation using multi-element model particles, *Engineering Computations* **1999**, *16*, 467.

[155] C. C. Ho, A. Keller, J. A. Odell, R. H. Ottewill, Preparation of monodisperse ellipsoidal polystyrene particles, *Colloid Polym Sci* **1993**, *271*, 469.

[156] D. R. Stull, Vapor Pressure of Pure Substances. Organic and Inorganic Compounds, *Ind. Eng. Chem.* **1947**, *39*, 517.

[157] I. Mamaliga, W. Schabel, M. Kind, Measurements of sorption isotherms and diffusion coefficients by means of a magnetic suspension balance, *Chemical Engineering and Processing - Process Intensification* **2004**, *43*, 753.

[158] I. Sakurada, A. Nakajima, H. Fujiwara, Vapor pressures of polymer solutions. II. Vapor pressure of the poly(vinyl alcohol)-water system, *J. Polym. Sci.* **1959**, *35*, 497.

6.1   List of Figures

6.2 Student thesis supervised during the realization of this work

1. Jakob Gröne, *Beschichten einer Polymer-Nanopartikel Lösung und Untersuchung der Morphologie mittels Mikro-Raman Spektroskopie*, Bachelorarbeit, Karlsruher Institut für Technologie (KIT) 2019

2. Nikolas Oberle, *Experimentelle und theoretische Untersuchung von ternären Polymer-Polymer-Lösemittel Phasendiagrammen*, Bachelorarbeit, Karlsruher Institut für Technologie (KIT) 2019

3. Louis Kontschak, *Untersuchung der rheologischen Eigenschaften von Suspensionen zur Herstellung von Polymer-Partikel Kompositen*, Bachelorarbeit, Karlsruher Institut für Technologie (KIT) 2019

4. Manuel Batora, *Untersuchung der Temperatur- und Konzentrationsabhängigkeit ternärer Phasendiagramme* Bachelorarbeit, Karlsruher Institut für Technologie (KIT) 2019

5. Nadine Zimmerer, *Untersuchung des Trocknungsverhaltens und der Ausbildung der Mikrostruktur von Anoden für Natrium-Ionen-Batterien,* Masterarbeit, Karlsruher Institut für Technologie (KIT) 2020

6. Tanatta Vanessa van Bonn, *Untersuchungen zu antibakteriellen Beschichtungen aus Polyvinylpyrrolidon mit Silber-Nanopartikel*, Bachelorarbeit, Karlsruher Institut für Technologie (KIT) 2020

6.3 Publications, conference talks and posters emanated from this work

Publications

1. **V.-A. Gracia-Medrano-Bravo**, J. Gröne, S. Baesch, P. Scharfer, W. Schabel, *Influence of Particle Shape on the Drying Regime Maps for Plate-like Particle-Polymer Composites*, Langmuir 2020, 36, 6245.

2. **V.-A. Gracia-Medrano-Bravo**, P. Scharfer, W. Schabel, *On the drying kinetics of non-spherical particle-filled polymer films: A numerical study*, AIChE Journal 2022, 68.

3. **V.-A. Gracia-Medrano-Bravo**, L. Merklein, N. Oberle, M. Batora, P. Scharfer, W. Schabel, Determination of Binary Interaction Parameters for Ternary Polymer–Polymer–Solvent Systems Using Raman Spectroscopy, Adv. Mater. Technol. 2021, 6, 2000149.

Conference talks

1. **Víctor Gracia**; Philip Scharfer; Wilhelm Schabel, *Drying of bimodal spherical particle-polymer-composites*, Jahrestreffen der ProcessNet-Fachgruppen Lebensmittelverfahrenstechnik und Trocknungstechnik, March 10-11, 2022, Frankfurt am Main, Germany

2. **Víctor Gracia**; Philip Scharfer; Wilhelm Schabel, *Simulation of bimodal particle systems*, 14th European Coating Symposium, September 7-9, 2021, Brussels, Belgium

3. **Víctor Gracia**; Philip Scharfer; Wilhelm Schabel, *Simulation of drying for particle-polymer systems*, Jahrestreffen der ProcessNet-Fachgruppen Hochdruckverfahrenstechnik und Trocknungstechnik zusammen mit dem Jahrestreffen der ProcessNet-Fachgruppe Phytoextrakte, March 15-16, 2021, Virtual Event, Germany

4. **Víctor Gracia**; Jakob Gröne; Susana Baesch; Philip Scharfer; Wilhelm Schabel, *Drying of anisotropic systems* , Jahrestreffen der ProcessNet-Fachgruppen Hochdruckverfahrenstechnik und Trocknungstechnik zusammen mit dem Jahrestreffen der ProcessNet-Fachgruppe Phytoextrakte, February 24-26, 2021, Virtual Event, Germany

5. **Víctor Gracia**; Jakob Gröne; Susana Baesch; Philip Scharfer; Wilhelm Schabel, *Drying of non-spherical polymer-particle-composites*, 20th International Coating Science and Technology Symposium, September 20-23, 2020, Virtual Event, USA

6. **Víctor Gracia**; Jakob Gröne; Susana Baesch; Philip Scharfer; Wilhelm Schabel, *Drying of polymer-particle composites*, 13th European Coating Symposium, September 08-11, 2019, Heidelberg, Germany

7. **Víctor Gracia**; Lisa Merklein; Philip Scharfer; Wilhelm Schabel, *Drying of thin polymeric films*, 7th European Drying Conference, July 10-12, 2019, Turin, Italy

8. **Víctor Gracia**; Susana Baesch; Philip Scharfer; Wilhelm Schabel; *Trocknung von Polymer-Partikel-Komposit-Lösungen mit plättchenförmigen Graphen-Partikeln*; ProcessNet-Jahrestagung und 33. DECHEMA-Jahrestagung der Biotechnologen, September 12-13 2018, Aachen, Germany

Conference posters

1. **Víctor Gracia**; Lisa Merklein; Philip Scharfer; Wilhelm Schabel, *Theoretische und experimentale Untersuchung der Prozessierung ternärer Systeme zur Herstellung von Polymerbeschichtungen*, Jahrestreffen der ProcessNet-Fachgruppe Wärme- und Stoffübertragung, March 12-13 2020, Erfurt , Germany

2. **Víctor Gracia**; Lisa Merklein; Philip Scharfer; Wilhelm Schabel, *Experimental and theoretical processing of ternary systems to produce functionalized polymer coatings*, 13th European Coating Symposium, September 08-11, 2019, Heidelberg, Germany

3. **Víctor Gracia**; Jakob Gröne; Susana Baesch; Philip Scharfer; Wilhelm Schabel, *Drying of polymer-glass flakes composites*, 7th European Drying Conference, July 10-12, 2019, Turin, Italy

4. **Víctor Gracia**; Jakob Gröne; Susana Baesch; Philip Scharfer; Wilhelm Schabel, *Drying of polymer-particle composites*, 35th INTERNATIONAL CONFERENCE of THE POLYMER PROCESSING SOCIETY, May 5-12, Çesme, Turkey

5. **Víctor Gracia**; Jakob Gröne; Susana Baesch; Philip Scharfer; Wilhelm Schabel, *Influence of particle geometry and orientation on the drying regime maps using polymer-plate-like glass-flake Composites*, Jahrestreffen der ProcessNet Fachgruppe Wärme- und Stoffübertragung, March 18-19, Essen, Germany

7 Appendix

7.1 Adaptation of the state of the art simulation

The simulation of the mass transfer process begins shortly after the coating process, where all the plate-like particles are already aligned with the substrate. Using the same approach used and developed by Baesch et al.[73], the system is considered quasi binary. That means the interactions between particles and the polymer solution are separated from the interactions between polymer and solvent.

The average volume velocity of the ternary system $u^{V,t}$ is obtained as the sum of all velocities of each individual component $\hat{V}_i \cdot \dot{n}_i$, as shown in equation (7.1). The sum can be grouped in the binary term marked in red and the contributions of the particles.

$$u^{V,t} = \hat{V}_S \cdot \dot{n}_S + \hat{V}_P \cdot \dot{n}_P + \hat{V}_C \cdot \dot{n}_C = u^{b,t} + \hat{V}_C \cdot \dot{n}_C \qquad (7.1)$$

The conservation equation of the drying corresponds to the dynamic diffusion equation.

$$\frac{\partial \tilde{c}_i}{\partial t} = -\frac{\partial}{\partial z} \dot{n}_i \qquad (7.2)$$

The sedimentation and diffusion coefficients are included as it follows with the diffusions coefficient also considering the mass dependence and the maximal packing concentration.

$$\dot{n}_C = -\frac{\partial}{\partial z}\left[D_C(\phi_C) \cdot \frac{\partial \tilde{c}_C}{\partial z} + U_C(\phi_C) \cdot \tilde{c}_C \right] \qquad (7.3)$$

The molar flux for the binary polymer-solvent system derives from the Fick's law.

$$\dot{n}_i^b = D_{P,S}(X_S) \cdot \frac{\partial \tilde{c}_i^b}{\partial z} \qquad (7.4)$$

where $i = S, P$

The binary concentration can be converted to ternary with the following relation.

$$\tilde{c}_i^b = \frac{\tilde{c}_i}{1 - \phi_C} \qquad (7.5)$$

where $i = S, P$

Analog to the equation (7.1) the total ternary flux can also be divided in binary and the contribution of the particles

$$\dot{n}_i = \dot{n}_i^b + \tilde{c}_i \cdot \hat{V}_C \cdot \dot{n}_C \qquad (7.6)$$

Substituting the relation (7.5) in (7.4) results in the ternary conservation equations for the polymer and the solvent

$$\dot{n}_i = -D_{P,S}(X_S) \cdot \left(\frac{1}{1 - \phi_C} \frac{\partial \tilde{c}_i}{\partial z} + \frac{\tilde{c}_i}{(1 - \phi_C)^2} \frac{\partial \phi_C}{\partial z} \right) + \tilde{c}_i \cdot \hat{V}_C \cdot \dot{n}_C \qquad (7.7)$$

where $i = S, P$

Considering no significant changes in the volume the conservation equation can be written in terms of the volume fraction by multiplying by the specific volume $\hat{V}_i$, as it follows

$$\frac{\partial \phi_C}{\partial t} = -\frac{\partial}{\partial z} \Gamma_C = \frac{\partial}{\partial z} \left[D_{C,0}^{\perp}(r_p) \cdot \frac{d[Z(\phi_C) \cdot \phi_C]}{d\phi_C} \cdot \frac{\partial \phi_C}{\partial z} + U_{C,0}(r_p) \right.$$
$$\left. \cdot K(\phi_C) \cdot \phi_C \right] \qquad (7.8)$$

$$\frac{\partial \phi_i}{\partial t} = \frac{\partial}{\partial z} \left[D_{P,S}(X_S) \cdot \left(\frac{1}{1 - \phi_C} \frac{\partial \phi_i}{\partial z} + \frac{\phi_i}{(1 - \phi_C)^2} \frac{\partial \phi_C}{\partial z} \right) + \phi_i \cdot \Gamma_C \right]$$

where $i = S, P$

The initial concentration is assumed to be homogeneous along the film. The boundary conditions are the evaporation at the top of the film, and the impermeable substrate at the bottom. The shrinkage due to solvent leaving the film produces an advection term at the phase boundary $h(t)$ on the total mass flux of each component as shown in (7.9)

$$\dot{n}_i|_{z=h(t)} = j_i + \tilde{c}_i \cdot u_{Evap} = j_i + \tilde{c}_i \cdot \hat{V}_S \cdot \dot{n}_{Evap} \qquad (7.9)$$

Solving for the diffusion term and writing it as volume flux

$$j_i = \dot{n}_i|_{z=h(t)} - \tilde{c}_i \cdot \hat{V}_S \cdot \dot{n}_{Evap} \qquad (7.10)$$

$$\Gamma_i = \hat{V}_i \cdot \dot{n}_i|_{z=h(t)} - \phi_i \cdot \hat{V}_S \cdot \dot{n}_{Evap} \qquad (7.11)$$

The boundary conditions in terms of the volume flux are

$$\forall\, t > 0 : \Gamma_i|_{z=0} = 0 \qquad (7.12)$$

$$\forall\, t > 0 : \Gamma_i|_{z=h(t)} = -\phi_i \cdot \hat{V}_S \cdot \dot{n}_{Evap} \qquad (7.13)$$

where $i = P, C$

$$\forall\, t > 0 : \Gamma_S|_{z=h(t)} = (1 - \phi_S) \cdot \hat{V}_S \cdot \dot{n}_{Evap} \qquad (7.14)$$

The evaporation of the solvent is modeled with a viscous limit layer at the phase boundary using the integrated expression (7.15) for $\dot{n}_S^{evap}$ [20]

$$\dot{n}_S^{evap} = \tilde{\rho}_{gas} \cdot \beta_{S,air} \cdot \ln\left(\frac{1 - \tilde{y}_S^*(T)}{1 - \tilde{y}_S^\infty}\right) \qquad (7.15)$$

where, $\beta_{S,air}$ is the mass transfer coefficient from the phase boundary to the top of the limit layer. The gas molar density is $\tilde{\rho}_S$ and $\tilde{y}_S^*(T)$ is the temperature-dependent solvent concentration at the phase boundary, it is considered the same concentration as in thermodynamic equilibrium, and $\tilde{y}_S^\infty$ is the solvent concentration in the incoming air. In this work it is assumed that the air is completely dry.

The concentration at the phase boundary is modeled according to the Raoult's law $\tilde{y}_S^*(T) = a_S \cdot p_S^*(T)/p_{Tot}$ with the solvent activity from the Flory-Huggins solution theory[156]. The concentration dependence of the binary interaction parameter $\chi_{P,S}$ can be obtained from sorption and desorption measurements at defined thermodynamic conditions[157,158]. For PVA-Water the interaction parameter was studied by Jeck et al.[84]

$$\ln a_S = (1 - \phi_P^b) + \phi_P^b + \chi_{P,S} \cdot (\phi_P^b)^2$$

$$\chi_{P,S} = 5.9340 - 5.4556 \cdot (\phi_P^b)^{0.0725} \qquad (7.16)$$

The film thickness is obtained from the mass balance at the phase boundary. It is supposed that the drying occurs only at the top of the film and the film shrinkage is one dimensional.

$$\frac{dh}{dt} = -\dot{E} = -\hat{V}_S \cdot \dot{n}_S^{evap} \qquad (7.17)$$

The nondimensionalization of the system, is done with the characteristic length h_0 and time $t_{Char} = h_0/\dot{E}_0$. The initial drying rate is calculated using the expression (7.18).

$$\dot{E}_0 = \tilde{\rho}_{gas} \cdot \hat{V}_S \cdot \beta_{S,air} \cdot \ln\left(\frac{1 - \tilde{y}_{S,0}^*(T)}{1 - \tilde{y}_S^\infty}\right) \qquad (7.18)$$

This leads to the inclusion of the Péclet and Sedimentation numbers into the equation system, and thus the dimensionless equation system (7.19) and (7.20). The change on the drag coefficient is acknowledged through the binary relative viscosity $\eta_{rel}(\phi_P^b)$ based on the initial polymer concentration.

$$\frac{\partial \phi_C}{\partial \tau} = \frac{\partial \bar{\Gamma}_C}{\partial \bar{z}} = \frac{\partial}{\partial \bar{z}}\left[\frac{K(\phi_C)}{Pe_C \cdot \eta_{rel}(\phi_P)} \cdot \frac{d[Z(\phi_C) \cdot \phi_C]}{d\phi_C} \cdot \frac{\partial \phi_C}{\partial \bar{z}} + \frac{N_S \cdot K(\phi_C)}{\eta_{rel}(\phi_P)}\phi_C\right] \qquad (7.19)$$

for $i = S, P$

$$\frac{\partial \phi_i}{\partial \tau} = \frac{\partial}{\partial \bar{z}}\left[\frac{d_P(\phi_S)}{Pe_P} \cdot \left(\frac{1}{1 - \phi_C} \cdot \frac{\partial \phi_i}{\partial \bar{z}} + \frac{\phi_i}{(1 - \phi_C)^2} \cdot \frac{\partial \phi_C}{\partial \bar{z}}\right) + \phi_i \cdot \bar{\Gamma}_C\right] \qquad (7.20)$$

The zero-shear viscosity's concentration dependency of the aqueous PVA can be found on the experimental section of this work. It is important to notice that dimensionless evaporation rate $\bar{E}$ in equation (7.21) does not require the mass transfer coefficient to be calculated, making it independent of the air velocity.

$$\frac{d\bar{h}}{d\tau} = -\frac{\dot{E}}{\dot{E}_0} = -\bar{E} = -\frac{\ln\left(\frac{1 - \tilde{y}_S^*(T)}{1 - \tilde{y}_S^\infty}\right)}{\ln\left(\frac{1 - \tilde{y}_{S,0}^*(T)}{1 - \tilde{y}_S^\infty}\right)} \qquad (7.21)$$

The dimensionless boundary conditions are as it follows,

$$\bar{z} = 0 \; \forall \; \tau > 0 \qquad\qquad \bar{\Gamma}_i = 0 \qquad (7.22)$$

$$\bar{z} = \bar{h}(\tau) \; \forall \; \tau > 0 \qquad \bar{\Gamma}_S = -\frac{(1 - \phi_S) \cdot \hat{V}_S \cdot \dot{n}_S^{evap}}{E_0} \qquad (7.23)$$

$$\bar{z} = \bar{h}(\tau) \; \forall \; \tau > 0; for \; i \\ = C, P \qquad \bar{\Gamma}_i = \frac{\phi_i \cdot \hat{V}_S \cdot n_S^{evap}}{E_0} \qquad (7.24)$$

The simulation is carried out with the initial concentration, temperature, aspect ratio, Pe_C and N_S as input parameters. The Péclet number for the polymer Pe_P is obtained from the Pe_C and the diffusion ratio polymer-solvent / particle-polymer solution.

$$Pe_P = Pe_C \cdot \left(\frac{D_{C,0}}{D_{S,P,0}} \right) \qquad (7.25)$$

7.2　　Viscosity curves
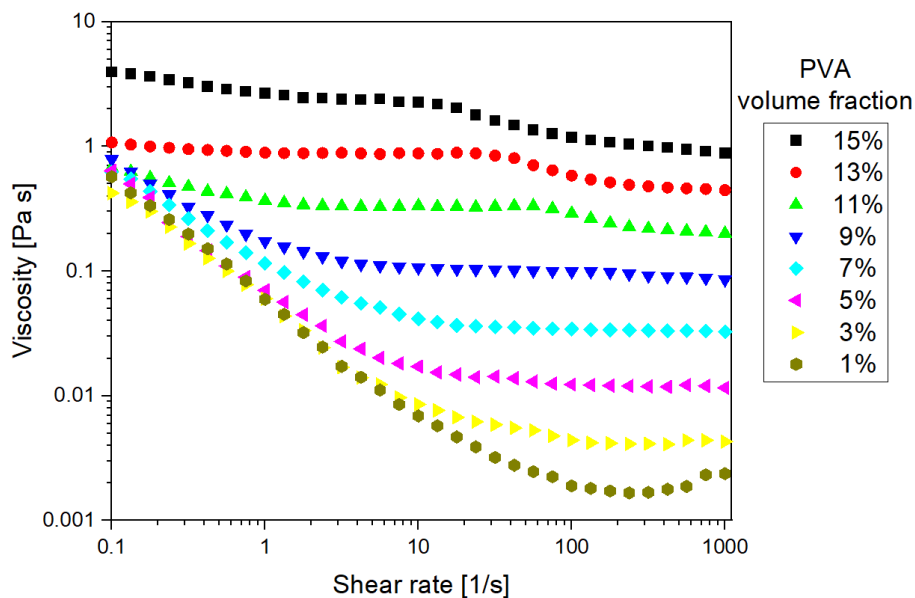
Figure 7.1. Viscosity of aqueous PVA solutions at $T = 40\,°C$ and different volume fractions as a function the shear rate.
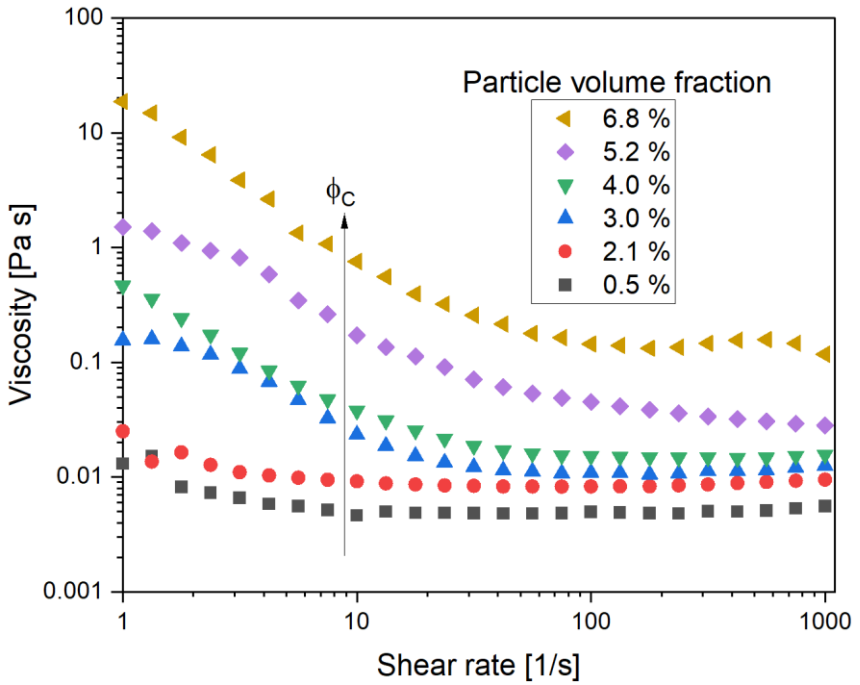
Figure 7.2. Viscosity of 3% v/v aqueous PVA plate-like particle dispersions at $T = 40\,°C$ and different volume fractions as a function the shear rate.

7.2.1 Determination of the overlap concentration

The overlap concentration at $40\,°C$ for the binary PVA aqueous solution is determined by measuring the viscosity at different polymer volume fractions ϕ_P^b. The transition for $[\eta]\phi_{C,overlap}$ is obtained by fitting the points and adding measurements to one side or the other until the coefficient of determination r^2 reaches a maximum on the diluted and concentrated regimes.
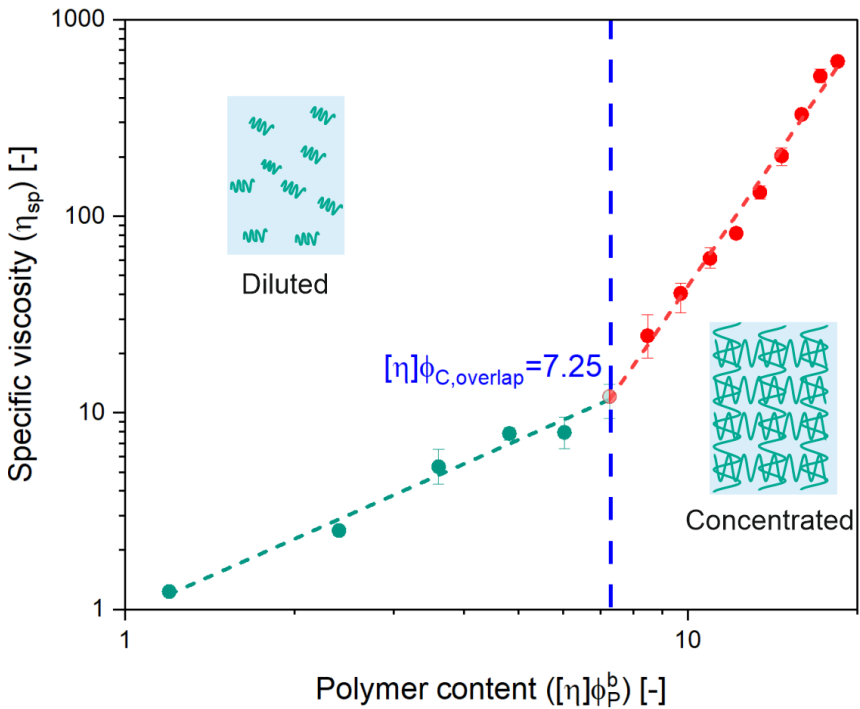
Figure 7.3. Determination of the overlap concentration for aqueous PVA at $T = 40°C$.

7.3 Diffusion coefficient for PVA-water

The PVA diffusion coefficient in water were determined using drying experiments and measuring the concentration in wet film via IMRS as described by Siebel et al.[41] The automatize program to obtain the spectral information can be found in Section 7.7

$$D_{P,S} = \exp\left(-\frac{A + BX_S}{1 + CX_S}\right)$$

A 28,73

B 60,44

C 2,632
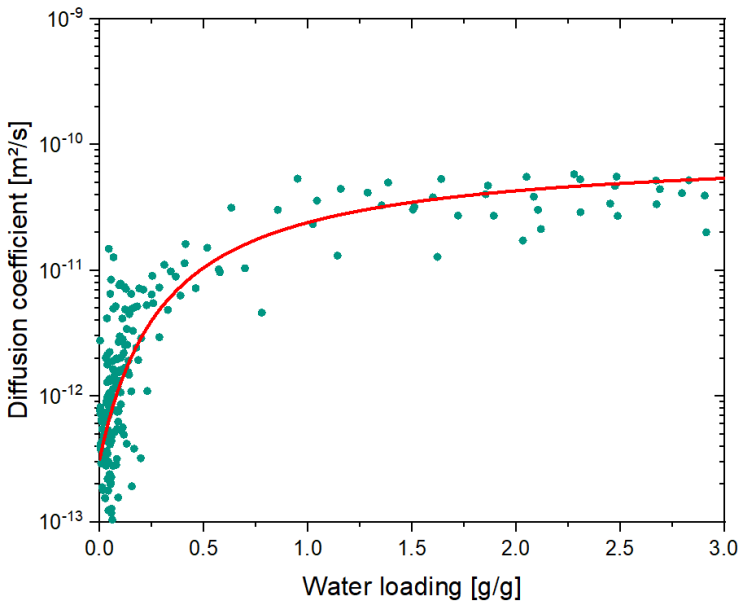
Figure 7.4. Diffusion coefficient of PVA in water as a function of the water loading at 40°C. The experimental data is fitted using equation (1.1).

7.4 Sedimentation rate measurements at $12\,g$
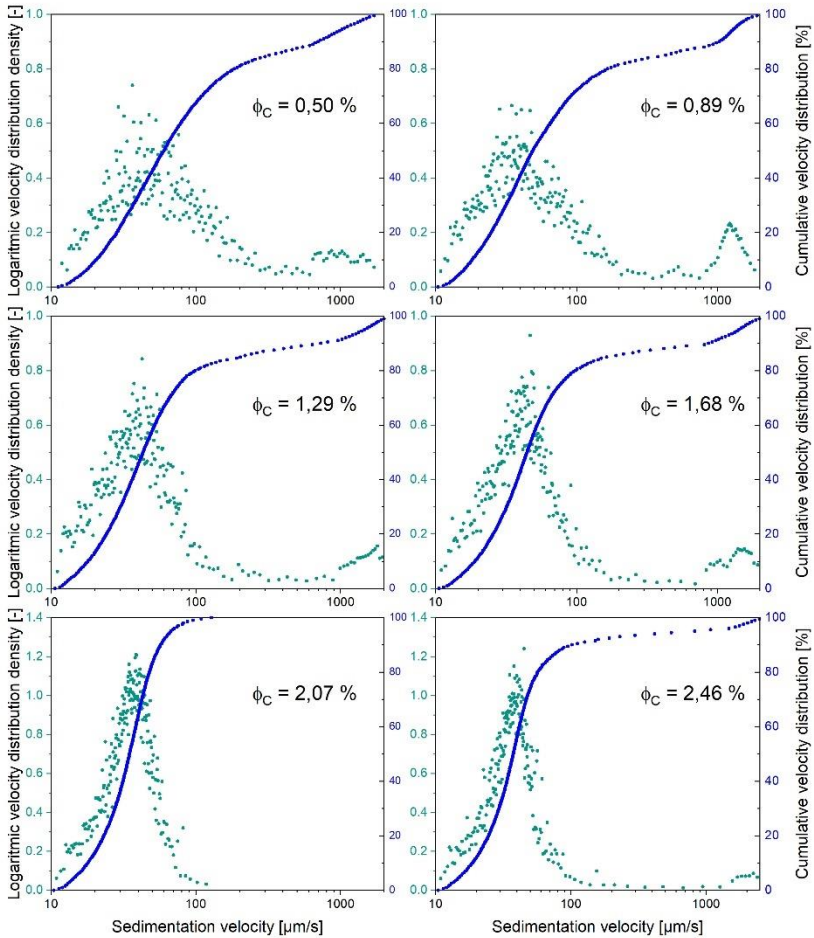
Figure 7.5.Cumulative velocity distribution and logarithmic velocity distribution density as a function of the sedimentation velocity of a $3\%\ v/v$ PVA glass flakes aqueous dispersion at 40 °C. The measurements were obtained at Institute of Mechanical Process Engineering and Mechanics (MVM).
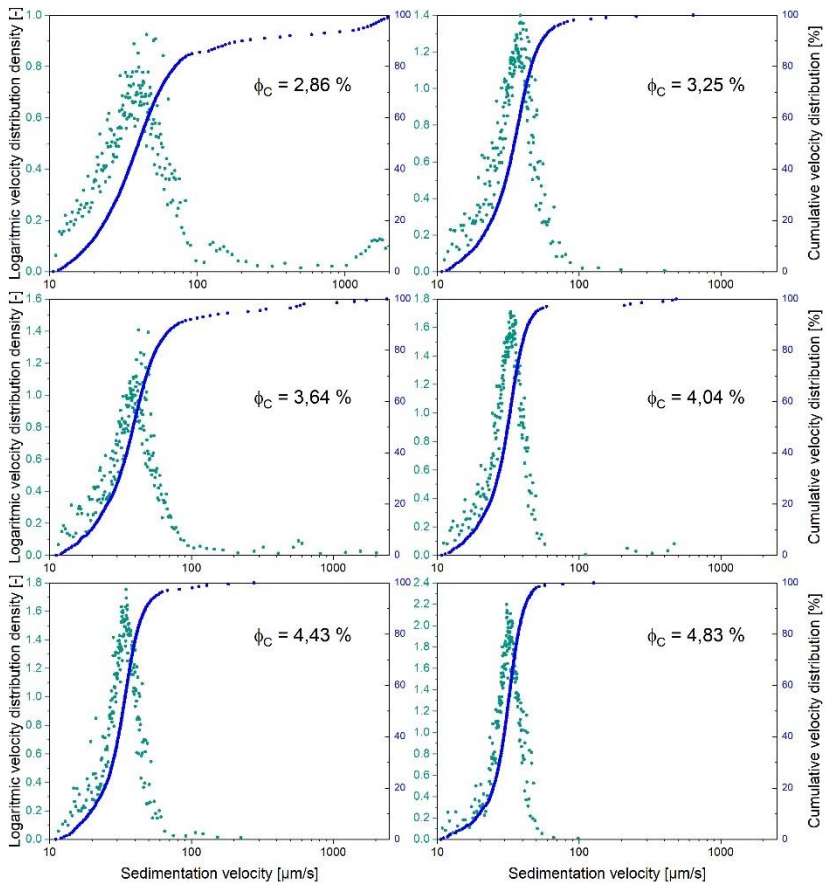
Figure 7.6.Cumulative velocity distribution and logarithmic velocity distribution density as a function of the sedimentation velocity of a $3\% \ v/v$ PVA glass flakes aqueous dispersion at 40 °C. The measurements were obtained at Institute of Mechanical Process Engineering and Mechanics (MVM).

133
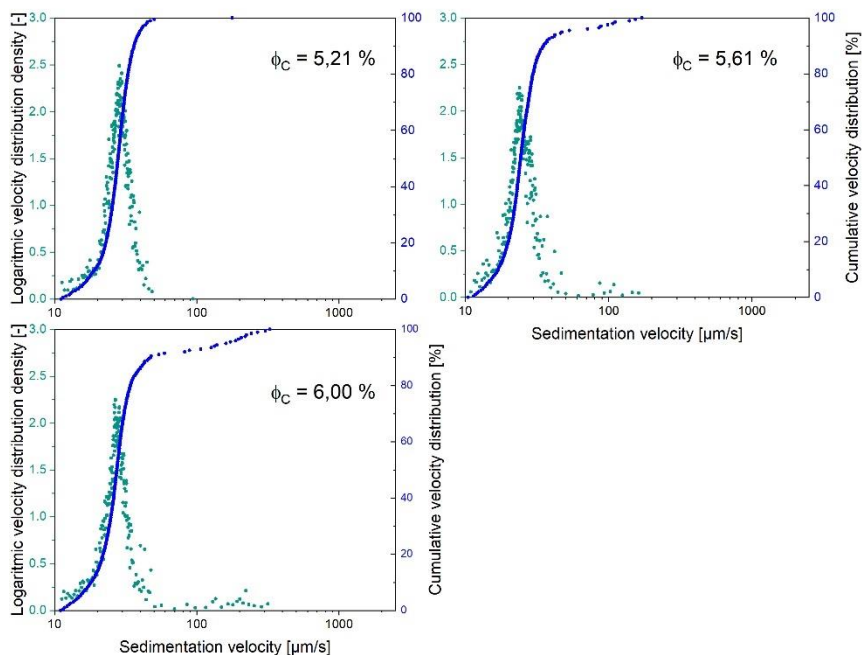
Figure 7.7.Cumulative velocity distribution and logarithmic velocity distribution density as a function of the sedimentation velocity of a $3\% \, v/v$ PVA glass flakes aqueous dispersion at 40 °C. The measurements were obtained at Institute of Mechanical Process Engineering and Mechanics (MVM).

7.5   COMSOL automatized script

```
//Initialization with number of points

int n = 500;
int it = 0;

//Variable declaration

double Pe_S[] = new double[n];
double N_S[] = new double[n];

//Sedimentation number interval

N_S[0] = 1e-4;
N_S[n-1] = 1e4;

double M[][] = new double[n][2];

for (int i = 0; i <= n-1; ++i) {
  N_S[i]                   =                   Math.pow(10,
Math.log10(N_S[0])+i*((Math.log10(N_S[n-1])-
Math.log10(N_S[0]))/(n-1)));
}
double error;

double[][] phi_x;

int it_max = 100;

double tol = 1e-4;

double x_n[] = new double[it_max+3];
x_n[0] = model.param().evaluate("Pec");
x_n[1] = 1.0003*x_n[0];
double f_n[] = new double[it_max+3];
```

```java
phi_x = evaluateToDoubleArray2D(model.result().numerical("max1"));

//Initialization

model.param().set("Ns", N_S[0]);
model.param().set("Pec", x_n[0]);
model.study("std1").run();
phi_x = evaluateToDoubleArray2D(model.result().numerical("max1"));
f_n[0]        =        phi_x[0][0]-model.param().evaluate("phi_C_m")*0.9;

model.param().set("Pec", x_n[1]);
model.study("std1").run();
phi_x = evaluateToDoubleArray2D(model.result().numerical("max1"));
f_n[1]        =        phi_x[0][0]-model.param().evaluate("phi_C_m")*0.9;
x_n[2]        =        Math.abs(x_n[1]-f_n[1]*((x_n[1]-x_n[0])/(f_n[1]-f_n[0])));

error = Math.abs((x_n[2]-x_n[1])/x_n[1]);

//Main iteration loop

for (int a = 0; a <= n-1; ++a) {

  if (a > 0) {
    model.param().set("Ns", N_S[a]);

    x_n[0] = x_n[it-2];

    model.param().set("Pec", x_n[0]);
    model.study("std1").run();
    phi_x        =        evaluateToDoubleArray2D(model.result().numerical("max1"));

    f_n[0]        =        phi_x[0][0]-model.param().evaluate("phi_C_m")*0.9;

    x_n[1] = x_n[it-1];
```

```
    model.param().set("Pec", x_n[1]);
    model.study("std1").run();
    phi_x      =      evaluateToDoubleArray2D(model.re-
sult().numerical("max1"));

    f_n[1]    =     phi_x[0][0]-model.param().evalu-
ate("phi_C_m")*0.9;

    x_n[2]    =     Math.abs(x_n[1]-f_n[1]*((x_n[1]-
x_n[0])/(f_n[1]-f_n[0])));

  }

  it = 3;

  //Main iteration loop

  do {

    model.param().set("Pec", x_n[it-1]);
    model.study("std1").run();
    phi_x      =      evaluateToDoubleArray2D(model.re-
sult().numerical("max1"));

    f_n[it-1]    =    phi_x[0][0]-model.param().evalu-
ate("phi_C_m")*0.9;

    x_n[it] = Math.abs(x_n[it-1]-f_n[it-1]*((x_n[it-
1]-x_n[it-2])/(f_n[it-1]-f_n[it-2])));

    error = Math.abs((x_n[it]-x_n[it-1])/x_n[it-1]);

    it = it+1;

  } while (it < it_max && error > tol);

  Pe_S[a] = x_n[it-1];

  for (int i = 0; i <= n-1; ++i) {
    M[i][1] = Math.log10(Pe_S[i]);
    M[i][0] = Math.log10(N_S[i]);
```

```
    }

    String[][] stringMatrix = toString(M);

    //the path of the output-excel-file with the results
    writeExcelFile("path", stringMatrix);

}
```

7.6   MATLAB imaging script

```
tic
clear all
clf
clc

PS=importdata(''); % Component_1
PVA=importdata(''); % Component_2

W_PS=interp(PS(:,1),4);
I_PS=interp(PS(:,2),4);
I_PVA=interp(PVA(:,2),4);
I_PS=sgolayfilt(I_PS,3,21);
I_PVA=sgolayfilt(I_PVA,3,21);

x_2=find(abs(W_PS-2500)==min(abs(W_PS-2500)));
x_1=find(abs(W_PS-3650)==min(abs(W_PS-3650)));

n_I(:,1)=I_PS-min(I_PS);
n_I(:,1)=n_I(:,1)/max(n_I(:,1));

n_I(:,2)=I_PVA-min(I_PVA);
n_I(:,2)=n_I(:,2)/max(n_I(:,2));

[fileID,pathname]=uigetfile('.txt','Wählen Sie ein 3D
Mapping');
A=importdata([pathname,fileID]);

Y=A(2:end,2);
X=A(2:end,1);
Z=A(2:end,3);
y=unique(Y);
x=unique(X);
z=unique(Z);

W=A(1,4:end);
```

```matlab
for i=1:length(y)
    mean_index=find(A(2:end,1)==y(i));
    I_mean(:,i)=mean(A(mean_index,4:end));
end

parfor i=2:length(A(1:end,3))
    I(:,i-1)=sgolayfilt(interp(A(i,4:end),4),3,21);
    I(:,i-1)=medfilt1(I(:,i-1),7);
end

plot(mean(I'));
ylabel('Intensität [a.u.]')
xlabel('Raman Shift [1/cm]')
 [xi,yi] = getpts;

xi=round(xi);
textprogressbar('Fortschritt: ');
for j=1:length(I(1,:))
clear m b
m(1)=(I(xi(1),j)-I(1,j))/(xi(1)-1);
b(1)=I(1,j)-m(1);

for i=1:length(xi)-1
    m(i)=(I(xi(i+1),j)-I(xi(i),j))/(xi(i+1)-xi(i));
    b(i)=I(xi(i+1),j)-m(i)*xi(i+1);
end

m(end+1)=(I(end,j)-I(xi(end),j))/(length(I(:,1))-
xi(end));
b(end+1)=I(end,j)-m(end)*length(I(:,1));

y_basis(1:xi(1),j)=(1:xi(1))*m(1)+b(1);

for i=1:length(xi)-1
    y_ba-
sis(xi(i):xi(i+1),j)=(xi(i):xi(i+1))*m(i)+b(i);
end
```

```
y_ba-
sis(xi(end):length(I(:,1)),j)=(xi(end):length(I(:,1))
)*m(end)+b(end);

I_basis(:,j)=I(:,j)-y_basis(:,j);
textprogressbar(floor(j/(length(I(1,:))-1)*100));
end
textprogressbar('fertig!');
parfor i=1:length(I(1,:))
    n_I_m(:,i)=I(x_1:x_2,i)-min(I(x_1:x_2,i));
    n_I_m(:,i)= n_I_m(:,i)/max(n_I_m(:,i));
end


parfor i=1:length(I(1,:))
    a=fmincon(@(alpha)error2f(alpha(1),x_1,x_2,[al-
pha(2),al-
pha(3)],n_I_m(:,i),n_I),[0.5,18*4,12*4],[],[],[],[],[
0,-20*4,-20*4],[1,20*4,20*4]);
    a_r(:,i)=a;
    [eqf(i),I_fit(:,i)]=er-
ror2f(a(1),x_1,x_2,[a(2),a(3)],n_I_m(:,i),n_I);
end


omega=a_r(1,:)./(1-a_r(1,:));


X_PS=omega/1.89; % Calibration constant here


X_PS=X_PS';
n_X=zeros(length(X_PS),1);
n_X=X_PS-min(X_PS);
n_X=n_X/max(n_X);


Kor=A(2:end,1:3);


for i=1:length(x)
    for j=1:length(y)
        for k=1:length(z)
            index=find(Kor(:,1)==x(i) &
Kor(:,2)==y(j) & Kor(:,3)==z(k));
            K_m(k,j,i)=X_PS(index);
```

```
            n_K(k,j,i)=n_X(index);
        end
    end
end

clf
surface(y,z,K_m(:,:,13))
colorbar
shading interp
colormap(jet)
axis equal
xlabel('X [µm]')
ylabel('Z [µm]')

toc

function [eqf,I_fit]=er-
ror2f(a,x_1,x_2,shift,I_n_m,I_n_r)
    shift=round(shift);
    I_fit=a*I_n_r(x_1+shift(1):x_2+shift(1),1)+(1-
a)*I_n_r(x_1+shift(2):x_2+shift(2),2);
    I_fit=I_fit-min(I_fit);
    I_fit=I_fit/max(I_fit);

    epsilon=abs(I_fit-I_n_m);

    eqf=sum(epsilon)^2;
end
```

7.7 Visual Basic Script (VBS) for the in situ Raman measurements

```vbs
'=== Skript für Trocknungsversuche von Max ===
'    adaptiert von 3D.vbs von Victor 2020/01
'    Last modified: 10.01.2020
'=============
'=== START ===
'=============
Option Explicit
'============================
'=== VARIABLE DECLARATIONS ===
'============================
'--- filesystem related variables
Dim dataPath, dataFolderName        ' data basefolder
/ data folder name
Dim folderList, fileList            ' sortable lists
Dim fso, f, file                    ' file system ob-
jects
Dim folder
Dim isCreateFolder
Const MB_OK = 0
Const MB_ICONERROR = 60
'--- config related values
Dim configPath
Dim abortFile
Dim zMin, zMax, zIncrement          ' z positions
from config file
Dim tExposure
Dim isAutoAbort                     ' abort according
to intensity drop?
Dim strRun
Dim tWait                           ' delay between
depth scans
Dim zPrecision
Dim dteWait
'--- settings related variables
Dim workingDistance
```

143

```
Dim nIMax                            ' amount of tol-
erable pixel errors in single spectrum
Dim tDiffMin                         ' min. time dif-
ference for new folder
Dim numberIntensityMax               ' number of past
intensities to consider for auto abort
Dim IFactor                          ' factor for in-
tensity abort
'--- spectrum related variables
Dim ScanCnt                          ' depth scan
counter
Dim ScanCntOffset                    ' depth scan off-
set if existing experiment is continued
'--- other
Dim Param                            ' uninitialized
variable for empty paramter list in LabSpec.Exec
'--- return values --> NECESSARY?
Dim SafeSucc         'Return_Safe
Dim SuccVal
'===============
'=== SETTINGS ===
'===============
dataPath = "D:\56 Gracia\00_Victor\00_Trocknungsver-
suche"     ' basefolder For data
configPath = "D:\56 Gracia\00_Victor\LabSpec-Parame-
ter.cfg"
abortFile = "D:\56 Gracia\00_Victor\LabSpec-Ab-
bruch.cfg"
tDiffMin = 3                         ' min. time dif-
ference from last depth scan for new folder in
minutes
workingDistance = 180                ' in um, specific
for microscope objective
nIMax = 3                            ' amount of tol-
erable pixel errors in spectrum
numberIntensityMax = 5               ' amount of past
max. intensities to consider for auto abort
IFactor = 0.3                        ' factor for in-
tensity abort
zPrecision = 1                       ' precision of
z_position
'===================
```

```vbnet
'=== SUBROUTINES ===
'==================
'=== create formatted date time (YYYY-MM-DD_HH-MM-SS)
from current system value
'===
Function getFormattedDateTimeNow
    Dim dateNow, year, month, day, hour, minute, sec-
ond
    dateNow = Now()
    year = DatePart("yyyy", dateNow)
    month = Right("00" & DatePart("m", dateNow), 2)
    day = Right("00" & DatePart("d", dateNow), 2)
    hour = Right("00" & DatePart("h", dateNow), 2)
    minute = Right("00" & DatePart("n", dateNow), 2)
    second = Right("00" & DatePart("s", dateNow), 2)
    getFormattedDateTimeNow = year & "-" & month & "-
" & day & "_" & hour & "-" & minute & "-" & second
End Function

Function getFormattedDateTime(dateTime)
    Dim dateNow, year, month, day, hour, minute, sec-
ond
    dateNow = dateTime
    year = DatePart("yyyy", dateNow)
    month = Right("00" & DatePart("m", dateNow), 2)
    day = Right("00" & DatePart("d", dateNow), 2)
    hour = Right("00" & DatePart("h", dateNow), 2)
    minute = Right("00" & DatePart("n", dateNow), 2)
    second = Right("00" & DatePart("s", dateNow), 2)
    getFormattedDateTime = year & "-" & month & "-" &
day & "_" & hour & "-" & minute & "-" & second
End Function
'=== wait for motor (piezo) movement to finish
'===
Private Sub MotorMove(Motor, Schritt)
    Dim ret
    ret = 1
    ret = LabSpec.MoveMotor(Motor, Schritt, 1, 0)
    Do While ret <> 0
        ret = LabSpec.GetMotorStatus(Motor,0)
    Loop
End Sub
```

```
'=== display complete arraylist (for debug)
'===
Private Sub printList(list)
    Dim message, element
    message = ""
    For Each element in list
        message = message & vbCrlf & element
    Next
    LabSpec.Message message, MB_OK
End Sub
Private Sub printArray(array)
    Dim message
    message = ""
    Dim i,j
    For i = 0 To UBound(array, 1)
        message = message & i & ":"
        For j = 0 To UBound(array, 2)
            message = message & vbTab &  array(i,j)
        Next
        message = message &  vbCrlf
    Next
    LabSpec.Message message, MB_OK
End Sub
'=== transpose txt file
'===
Function FileToArray(filePath)
    Dim file
    Dim strRawData
    Dim rowsRaw
    Dim iRow, iColumn
    Dim nRows, nColumns
    Dim strRowArray
    Dim strDataArray()

    Const FoReading = 1
    Const FoWriting = 2

    '--- read file to string
    Set file = fso.OpenTextFile(filePath, FoReading,
False)
    Do While file.AtEndOfStream <> True
        strRawData = file.ReadAll
```

146

```
    Loop
    file.Close

    '--- ensure that file is not empty
    If Trim(strRawData) <> "" Then
        rowsRaw = Split(strRawData, vbNewLine)
        nColumns = UBound(Split(rowsRaw(0), vbTab)) +
1
    End If  '--- exception handling for empty files
not given

    '--- set array dimensions
    If rowsRaw(UBound(rowsRaw)) = "" Then
        ReDim strDataArray(UBound(rowsRaw) - 1, nCol-
umns - 1)
    Else
        ReDim strDataArray(UBound(rowsRaw), nColumns
- 1)
    End If

    '--- convert string to array
    For iRow = 0 To UBound(rowsRaw)
        If rowsRaw(iRow) = "" Then
            '--- stop at blank line at EOF
            Exit For
        End If
        strRowArray = Split(rowsRaw(iRow), vbTab)
        For iColumn = 0 To nColumns - 1
            strDataArray(iRow, iColumn) =
strRowArray(iColumn)
        Next
    Next

    FileToArray = strDataArray
End Function
'=== transpose string array and write it to file
'===
Sub ArrayTransposedToFile(filePath, strDataArray)
    Dim file
    Dim strRawRow
    Dim i,j
```

```
    Const FoWriting = 2

    Set file = fso.OpenTextFile(filePath, FoWriting,
True)

    '--- dimension 2 was columns will be rows
    For i = 0 To UBound(strDataArray, 2)
        strRawRow = ""
        '--- dimension 1 was rows will be columns
        For j = 0 To UBound(strDataArray, 1)
            If j = UBound(strDataArray, 1) Then
                strRawRow = strRawRow &
strDataArray(j,i)
            Else
                strRawRow = strRawRow &
strDataArray(j,i) & vbTab
            End If
        Next
        file.WriteLine(strRawRow)
    Next
    file.Close
End Sub
'=== subroutine for single depth scan
'===
Sub DepthScan (tExposure, zMin, zMax, zIncrement,
ScanCnt)
    '--- acquisition related variables
    Dim isFirstSpectrum
    Dim currentDateTime
    Dim SpectrumID                    ' Spectrum Nummer
    Dim zPosTarget, zPosCurrent
    Dim i
    Dim ProfileID
    Dim fileName, fileNameNew

    '--- intensity cutoff related variables
    Dim DataArray()                   ' Intensitae-
ten Messspektrum
    Dim IMaxCurrent
    Dim maxIntensityList, maxIntensityListSorted
    Set maxIntensityList = CreateObject("System.Col-
lections.ArrayList")
```

148

```
    Dim DataList

    '--- data management
    Dim strDataArray
    Dim dateModified

    '--- timer (use integral timer2 instead)
    Dim lastTime, currentTime
    Dim times()
    Dim timeAverage
    '---timer2
    Dim lastTime2, currentTime2
    Dim time2
    Dim timeAverage2
    Dim nSpectra

    isFirstSpectrum = True
    zPosTarget = zMin
    nSpectra = 0

    currentDateTime = getFormattedDateTimeNow

    '---timer2 start
    lastTime2 = Timer

    Do While zPosTarget =< zMax
        '---timer1 start (use integral timer2 in-
stead)
        ' lastTime = Timer

        '--- move to desired z position
        MotorMove "Z", zPosTarget
        '--- get actual z-position (due to piezo
clipping at +-171 um / rounded to precision given in
settings)
        zPosCurrent = Round(LabSpec.GetMotorPosi-
tion("Z", 1), zPrecision)

        '--- Acquire Spectrum
        LabSpec.Acq 0, tExposure, 1, 0, 0
        nSpectra = nSpectra + 1
        Do
```

149

```
            SpectrumID = LabSpec.GetAcqID() ' Wait
until Spectrum is ready (acquisition is done)
        Loop Until SpectrumID > 0

        If isFirstSpectrum = True Then
            '--- Create a profile With the first
spectrum
            ProfileID = LabSpec.Profile(0, 0, Spec-
trumID, zPosCurrent, "mm", "Tiefe")    ' Mode (0: cre-
ate, 1: add), ProfileID (only when mode:create),
SpectrumID, extra dimension value, Unit, Label

            isFirstSpectrum = False
        Else
            '--- add spectrum to existing profile
            ProfileID = LabSpec.Profile(1, ProfileID,
SpectrumID, zPosCurrent, "mm", "Tiefe")
        End If

        LabSpec.Exec ProfileID, 0, Param          '
Show Profile

        '--- save spectra (in z loop, in order to re-
tain data if depth scan was aborted in LabSpec)
        fileName = dataPath & "\" & dataFolderName &
"\" & currentDateTime & "_" & "Tiefenscan_" &
Right("00" & ScanCnt,3)
        SafeSucc = LabSpec.Save(ProfileID, fileName &
".tvf", "tvf")
        SafeSucc = LabSpec.Save(ProfileID, fileName &
".txt", "txt")

        '--- auto abort due to intensity cutoff
        If isAutoAbort = "JA" Then
            '--- current spectral intensity data to
array
            SuccVal = LabSpec.GetValue(SpectrumID,
"Data", DataArray)
            ' LabSpec.Message "SuccVal: " & SuccVal ,
MB_NON_BLOCKING+MB_OK
```

```
            '--- transform array to ArrayList object
for easy sorting
            Set DataList = CreateObject("System.Col-
lections.ArrayList")
            For i = 0 To UBound(DataArray)
                DataList.Add DataArray(i)
            Next
            DataList.Sort()
            DataList.Reverse()

            '--- extract n'th highest element
            IMaxCurrent = DataList(nIMax)

            If maxIntensityList.Count > 0 Then
                '--- create a copy of past intensity
list for sorting
                Set maxIntensityListSorted = Cre-
ateObject("System.Collections.ArrayList")
                maxIntensityListSorted.AddRange(max-
IntensityList)
                maxIntensityListSorted.Sort()
                maxIntensityListSorted.Reverse()
                ' printList maxIntensityListSorted

                If IMaxCurrent < IFactor * maxInten-
sityListSorted(0) Then
                    MotorMove "Z", zMin
                    ' LabSpec.Message "STOP due to
intensity cutoff", MB_OK
                    Exit Do
                End If
            End If

            '-- add nIMax'th highest Value to list
            maxIntensityList.Add DataList(nIMax)

            If maxIntensityList.Count > numberInten-
sityMax Then
                ' LabSpec.Message "deleted one ele-
ment", MB_OK
                maxIntensityList.Remove(maxInten-
sityList.Item(0))
```

```
            End If
        End If

        '--- Abort individual depth scan manually
        If fso.FileExists(abortFile) Then
            fso.DeleteFile abortFile
            Exit Do
        End If

        '--- timer1 end (use integral timer2 instead)
        ' currentTime = Timer
        ' If zPosTarget = zMin Then
        '     ReDim times(0)
        ' Else
        '     ReDim Preserve times(UBound(times)+1)
        ' End If
        ' times(UBound(times)) = currentTime -
lastTime

        zPosTarget = zPosTarget + zIncrement
    Loop

    currentTime2 = Timer
    time2 = currentTime2 - lastTime2
    'timeAverage2 = time2 / (CLng((zMax - zMin) /
zIncrement) + 1)
    timeAverage2 = time2 / (CLng((zPosTarget - zMin)
/ zIncrement) + 1)
    timeAverage2 = time2 / CLng(nSpectra)

    '--- rename to DateLastModified (MoveFile does
NOT change the actual DateLastModified)
    dateModified = fso.GetFile(fileName &
".tvf").DateLastModified
    fileNameNew = dataPath & "\" & dataFolderName &
"\" & getFormattedDateTime(dateModified) & "_" &
"Tiefenscan_" & Right("00" & ScanCnt,3)
    fso.MoveFile fileName & ".txt", fileNameNew &
".txt"
    fso.MoveFile fileName & ".tvf", fileNameNew &
".tvf"
```

```
    '--- calculate average measurement time per spec-
trum (use integral timer2 instead)
    ' For i = 0 To UBound(times)
        ' timeAverage = timeAverage + times(i)
    ' Next
    ' timeAverage = timeAverage / (UBound(times) + 1)

    '--- transpose data in file
    strDataArray = FileToArray(fileNameNew & ".txt")
    strDataArray(0, 0) = Replace(FormatNumber(timeAv-
erage2,2,-1,0,0),",",".")
    ArrayTransposedToFile fileNameNew & ".txt",
strDataArray
End Sub
'===================
'=== MAIN PROGRAM ===
'===================
'--- check if data folder empty or last depth scan
older than tDiffMin minutes, if yes create new
folder, otherwise continue using last folder
Set fso = CreateObject("Scripting.FileSystemObject")
If fso.GetFolder(dataPath).SubFolders.Count = 0 Then
    isCreateFolder = True
Else
    Set folderList = CreateObject("System.Collec-
tions.ArrayList")

    For Each folder In fso.GetFolder(dataPath).Sub-
Folders
        folderList.Add folder.Name
    Next
    folderList.Sort()
    folderList.Reverse()

    If fso.GetFolder(dataPath & "\" & folder-
List(0)).Files.Count = 0 Then
        isCreateFolder = True
    Else
        '--- get all files in existing subfolder and
set depth scan offset accordingly
        Set fileList = CreateObject("System.Collec-
tions.ArrayList")
```

153

```
        For Each file In fso.GetFolder(dataPath & "\"
& folderList(0)).Files
            If Right(file.Name, 4) = ".txt" Then
                fileList.Add file.Name
            End If
        Next
        fileList.Sort()
        fileList.Reverse()

        '--- extract date from folder name
        Dim year, month, day, hour, minute, second
        year = Mid(fileList(0), 1, 4)
        month = Mid(fileList(0), 6, 2)
        day = Mid(fileList(0), 9, 2)
        hour = Mid(fileList(0), 12, 2)
        minute = Mid(fileList(0), 15, 2)
        second = Mid(fileList(0), 18, 2)

        Dim fileDate
        fileDate = CDate(day & "." & month  & "." &
year  & " " & hour & ":" & minute & ":" & second)

        If DateDiff("n", fileDate, Now()) >= tDiffMin
Then
            isCreateFolder = True
        Else
            dataFolderName = folderList(0)
            ScanCntOffset =
CLng(Left(Right(fileList(0), 7), 3))
            isCreateFolder = False
        End If
    End If
End If

If isCreateFolder = True Then
    '--- Create folder for measurement data
    dataFolderName = getFormattedDateTimeNow
    Set f = fso.CreateFolder(dataPath & "\" & data-
FolderName)
End If
```

```
'--- read config for first time (in order to get zMax
BEFORE first scan execution)
Set file = fso.OpenTextFile(configPath, 1)  ' 1: read
only
strRun = file.ReadLine
tExposure = CDbl(Replace(file.ReadLine, ".", ","))
zMin = CDbl(Replace(file.ReadLine, ".", ","))
zMax = CDbl(Replace(file.ReadLine, ".", ","))
zIncrement = CDbl(Replace(file.ReadLine, ".", ","))
tWait = CDbl(Replace(file.ReadLine, ".", ","))
isAutoAbort = file.ReadLine
file.close

'--- safety feature works only if zStart = 0 (inter-
face between glass substrate and film)
If zMax > workingDistance Then
    LabSpec.Message "zMax too large",MB_OK + MB_ICON-
ERROR
Else
    '--- loop through individual depth scans (999
limit due to 3 digit filename numeration)
    For ScanCnt = 1 To (999 - ScanCntOffset)
        '--- read config (after depth scan because
this way STOP and DELAY changes during scan will be
considered before next scan)
        Set file = fso.OpenTextFile(configPath, 1)  '
1: read only
        strRun = file.ReadLine
        '--- apparently decimal symbol must be ",",
so conversion is optional at current setup
        tExposure = CDbl(Replace(file.ReadLine, ".",
","))
        zMin = CDbl(Replace(file.ReadLine, ".", ","))
        zMax = CDbl(Replace(file.ReadLine, ".", ","))
        zIncrement = CDbl(Replace(file.ReadLine, ".",
","))
        tWait = CDbl(Replace(file.ReadLine, ".",
","))
        isAutoAbort = file.ReadLine
        file.Close

        '--- perform depth scan
```

```
        DepthScan tExposure, zMin, zMax, zIncrement,
(ScanCnt + ScanCntOffset)

        '--- read config (after depth scan because
this way STOP and DELAY changes during scan will be
considered before next scan)
        Set file = fso.OpenTextFile(configPath, 1)   '
1: read only
        strRun = file.ReadLine
        '--- apparently decimal symbol must be ",",
so conversion is optional at current setup
        tExposure = CDbl(Replace(file.ReadLine, ".",
","))
        zMin = CDbl(Replace(file.ReadLine, ".", ","))
        zMax = CDbl(Replace(file.ReadLine, ".", ","))
        zIncrement = CDbl(Replace(file.ReadLine, ".",
","))
        tWait = CDbl(Replace(file.ReadLine, ".",
","))
        isAutoAbort = file.ReadLine
        file.Close

        '--- check for stop command
        If strRun = "STOP" Then
            MotorMove "Z", 0
            Exit For
        End If

        '--- wait for next measurement
        dteWait = Timer + tWait
        Do Until (Timer > dteWait)
        Loop
    Next
End If
'===================
'=== END PROGRAM ===
'===================
```
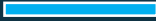
Víctor Gracia

Geburtsdatum: 19. August 1991

Geburtsort: Mexiko-Stadt

SPRACHEN

- Spanisch
- Deutsch
- Englisch
- Französisch

INTERESSEN

- Tennis
- Wandern
- Ski fahren

SOFTWARE-KENNTNISSE

- Microsoft Office und Visual Basic
- Aspen Plus und HYSYS
- Matlab und Python
- COMSOL Multiphysics
- CorelDraw

BERUFSERFAHRUNG

Seit 2022 Verfahrensingenieur
H-Tec Systems GmbH

- Entwicklung von Konzepten zur Herstellung von Elektrolyseuren.

2017-2022 Wissenschaftlicher Mitarbeiter
Karlsruher Institut für Technologie (KIT)

- Bearbeitung von Forschungsprojekten im Bereich Brennstoffzellen und Lithium-Ionen-Batterien.
- Entwicklung von numerischen Simulationen für Trocknungsprozesse.
- Analyse von Polymerfilmen mittels Raman Spektroskopie.
- Beschichtung- und Trocknungstechnologien von dünnen Polymerfilmen.

2014-2016 Tutor für Prozessleittechnik
Nationale Unabhängige Universität Mexiko (UNAM).

2013 Praktikum bei Organic Potash Corporation (Toronto, Kanada)

- Bachelorabschlussarbeit zur Dimensionierung einer Kaliumcarbonat-Anlage.

2011-2013 Praktikum
Institut für Chemie, Mexiko-Stadt

- Laborarbeit zur Synthese von 1-4 Diketonkomponenten mittels radikaler Reaktionen.
- Ergebnisse wurden bei Tetrahedron publiziert.

STUDIUM

2014-2016 Masterstudium Chemieingenieurwesen
UNAM, Mexiko-Stadt

- Vertiefungsfächer: Transportprozesse und Prozesssimulation.
- Masterarbeit: „Analyse von Stoff-Übertrager" nominiert für beste Abschlussarbeit des Jahrgangs.
- Abschlussnote: 10/10.
- Graduiert mit Honoris.

2013 Akademischer Austausch
University of Toronto, Toronto Kanada

- Durch ein 10.000 USD dotiertes Preisgeld finanziert.

2009-2013 Bachelorstudium Chemieingenieurwesen
UNAM, Mexiko-Stadt.

- Vertiefungsfächer: angewandte Mathematik und organische Synthese.
- Abschlussnote: 9,54/10.
- Graduiert mit Honoris.

2006-2009 Allgemeine Hochschulreife
Centro Universitario Mexico, Mexiko-Stadt

- Vertiefung: Physik und Mathematik.
- Abitur: 8,2/10.

PUBLIKATIONEN

- **Gracia-Medrano-Bravo, Víctor-Alfonso**, et al. "On the drying kinetics of non-spherical particle-filled polymer films: A numerical study." AIChE J (2021): 68(1):e17398.
- **Gracia-Medrano-Bravo, Víctor-Alfonso**, et al. "Determination of Binary Interaction Parameters for Ternary Polymer–Polymer–Solvent Systems Using Raman Spectroscopy." Advanced Materials Technologies (2020): 2000149.
- **Gracia-Medrano-Bravo, Víctor-Alfonso**, et al. "Influence of Particle Shape on the Drying Regime Maps for Platelike Particle–Polymer Composites." Langmuir 36.22 (2020): 6245-6253.